



**Max-Planck-Institut für Metallforschung**  
Stuttgart

---

## **High-Temperature Oxidation of Bulk RuAl Alloy**

Paul J. Bellina

Dissertation  
an der  
**Universität Stuttgart**

---

Bericht Nr. 185  
Februar 2006



# High-Temperature Oxidation of Bulk RuAl Alloy

Von der Fakultät Chemie der Universität Stuttgart  
Zur Erlangung der Würde eines Doktors der Naturwissenschaften  
(Dr. rer. nat.) genehmigte Abhandlung

vorgelegt von

**Paul J. Bellina**

aus Trieste (Italy)

Hauptberichter: Prof. Dr. M. Rühle  
Mitberichter: Prof. Dr. F. Aldinger  
Tag der Einreichung: 08 Dezember 2005  
Tag der mündlichen Prüfung: 13 Februar 2006

Max-Planck-Institut für Metallforschung  
Stuttgart 2006

Part of the results can be found on:

P.J. Bellina, A. Catanoiu, F.M. Morales, and M. Rühle: Formation of discontinuous  $\text{Al}_2\text{O}_3$  layers during high-temperature oxidation of RuAl alloys. *Journal of Materials Research* **21**, 276 (2006).

# CONTENTS

## LIST OF ABBREVIATIONS

<b>ABSTRACT</b>	<b>8</b>
<b>ZUSAMMENFASSUNG</b>	<b>12</b>
<b>1. INTRODUCTION</b>	<b>16</b>
<b>2. FUNDAMENTALS ON THE OXIDATION OF METALS AND ALLOYS</b>	<b>19</b>
2.1 Thermodynamics of the oxidation of pure metals at high temperature	19
2.2 Kinetics of the oxide growth	24
2.3 Oxidation of alloys	28
2.4 Different oxidizing atmospheres	31
2.5 Stresses in the oxide	31
<b>3. LITERATURE OVERVIEW</b>	<b>35</b>
3.1 The Thermal Barrier Coating system	35
3.1.1 The Top Coat	35

3.1.2	The thermal Grown Oxide and the Bond Coat	37
<b>3.2</b>	<b>Description of the systems involved in the oxidation of RuAl:</b>	<b>39</b>
3.2.1	The Ru-Al system	39
3.2.2	The Ru-O system	42
3.2.3	The Al-O system	43
<b>3.3</b>	<b>Oxidation at High-temperature of IrAl, Ru, RuAl</b>	<b>45</b>
3.3.1	Oxidation of IrAl	45
3.3.2	Oxidation of Ru	47
3.3.3	Oxidation of the RuAl	49
<b>4.</b>	<b>EXPERIMENTAL METHODS AND SAMPLE PREPARATION</b>	<b>51</b>
<b>4.1</b>	<b>Processing of the RuAl alloy</b>	<b>51</b>
<b>4.2</b>	<b>Thermogravimetric analysis</b>	<b>52</b>
<b>4.3</b>	<b>X-ray diffraction</b>	<b>55</b>
<b>4.4</b>	<b>Electron microscopy techniques:</b>	<b>58</b>
4.4.1	Scanning electron microscopy	60
4.4.2	Transmission electron microscopy	62
<b>5.</b>	<b>RESULTS</b>	<b>71</b>
<b>5.1</b>	<b>Morphological investigation of RuAl oxidized in air</b>	<b>71</b>
<b>5.2</b>	<b>Characterization of the multiphase material</b>	<b>85</b>
<b>5.3</b>	<b>Oxidation's kinetics: air vs. O<sub>2</sub> plus Ar</b>	<b>93</b>
<b>5.4</b>	<b>Evaporation of RuO<sub>3</sub> and RuO<sub>4</sub> during oxidation in O<sub>2</sub> plus Ar</b>	<b>103</b>

<b>5.5</b>	<b>Evolution of stresses in <math>\alpha</math>-Al<sub>2</sub>O<sub>3</sub>, <math>\delta</math>-Ru and RuO<sub>2</sub> during oxidation in air at 1100 °C</b>	<b>106</b>
<b>6.</b>	<b>DISCUSSION</b>	<b>109</b>
<b>6.1</b>	<b>Morphology of the Thermal Grown Oxide and substrate</b>	<b>109</b>
<b>6.2</b>	<b>Evolution of stresses during oxidation</b>	<b>113</b>
<b>6.3</b>	<b>Oxidation progress</b>	<b>114</b>
<b>7.</b>	<b>CONCLUSIONS</b>	<b>121</b>
<b>8.</b>	<b>REFERENCES</b>	<b>123</b>

**ACKNOWLEDGEMENTS**

**CURRICULUM VITAE**

## LIST OF ABBREVIATIONS

<b>AES</b>	Auger Electron Spectroscopy
<b>APS</b>	Air Plasma Spray
<b>BF</b>	Bright Field
<b>BC</b>	Bond Coat
<b>CTE</b>	Coefficient of Thermal Expansion
<b>CVD</b>	Chemical Vapour Deposition
<b>DF</b>	Dark Field
<b>EB-PVD</b>	Electron Beam Physical Vapour Deposition
<b>EDS</b>	Electron Dispersive Spectroscopy
<b>EELS</b>	Electron Energy Loss Spectroscopy
<b>ELNES</b>	Energy Loss Near Edge Structure
<b>EXELFS</b>	EXtended Energy Loss Fine Structure
<b>HAADF</b>	High Angle Annular Dark Field
<b>HIP</b>	Hot Isostatically Pressed
<b>HREM</b>	High Resolution Electron Microscopy
<b>HRTEM</b>	High Resolution Transmission Electron Microscopy
<b>LPPS</b>	Low Pressure Plasma Spray
<b>PBR</b>	Pilling Bedworth Ratio
<b>PGM</b>	Platinum Group Metals



<b>SAD</b>	Selective Area Diffraction
<b>SEM</b>	Scanning Electron Microscopy
<b>STEM</b>	Scanning Transmission Electron Microscopy
<b>TBC</b>	Thermal Barrier Coating
<b>TEM</b>	Transmission Electron Microscopy
<b>TGA</b>	ThermoGravimetric Analysis
<b>TGO</b>	Thermally Grown Oxide
<b>XEDS</b>	X-ray Electron Dispersive Spectroscopy
<b>XRD</b>	X-ray Diffraction
<b>YSZ</b>	Yttria Stabilized Zirconia

$a_{\text{Ru}}$	Ru's activity
$a_{\text{RuO}_2}$	RuO <sub>2</sub> 's activity
$\Delta G$	Gibbs energy
$\Delta G^0$	Free energy of formation
$K_{\text{eq}}$	Equilibrium constant
$P_{\text{O}_2}$	Oxygen partial pressure

## ABSTRACT

It is known that the efficiency of advanced gas turbines depends on the working temperature and that for this reason the research of alloys with higher melting point and better mechanical properties has been carried out in the last decades. A substantial improvement has been offered by the application of multifunctional coatings, which enhance the thermo-chemical resistance of the components. Thermal barrier coatings (TBCs), which were firstly adopted in order to improve the durability of the metal components, nowadays are considered as a prime reliant element, since can offer an improvement in temperature capability of almost 200 °C.

In present systems, thermal insulation is provided by an outer  $Y_2O_3$  partially-stabilized zirconia (YSZ) layer. Beneath this layer a chemical barrier is needed to protect the underlying superalloy from the thermal oxidation, because the porous YSZ is permeable to oxygen. Chemical protection is provided by a thin  $\alpha-Al_2O_3$  layer between the metal and thermal barrier. This layer grows during oxidation and hence is known as the thermally grown oxide (TGO). Since the superalloys are not optimized for oxidation resistance, development of a chemical barrier requires modification of the surface chemistry. A buffer layer is formed by adding specific elements, such as: Al, Pt, Cr, Co, Y. This buffer layer is commonly addressed as the bond coat (BC).

Improving the BCs is regarded as the highest priority for emerging TBC systems; in fact there is evidence that most of the TBC failures are related to the TGO and its interfacial separation. The common mode of failure is based on a partial buckling and subsequent spallation of the coating from the superalloy, and intuitively it can be understood that even the most sophisticated TBCs are not performing efficiently if they do not remain adherent to the turbine.

The use of Ru-containing BCs has been indicated as a promising alternative to (Ni,Pt)Al, which represents so far the most suitable material for BCs. It has been suggested that the utilization of platinum group metals (PGM) in the bulk buffer layer minimizes the interdiffusion with the superalloy. In particular, stoichiometric RuAl has a very good room temperature hardness and toughness. It possesses a high melting point, a coefficient of thermal expansion (CTE) close to that of  $\alpha-Al_2O_3$  and a good creep resistance. All

these characteristics render this alloy a potential candidate for high temperature applications.

The main objective of this thesis is to perform fundamental studies on the oxidation behaviour of polycrystalline RuAl bulk material.

All the experiments in this study were conducted on near stoichiometric polycrystalline RuAl (B2 structure) obtained by arc-melting and induction-melting. Mainly all the oxidation experiments were conducted isothermally at 1100 °C, which represents the desired working temperature for BCs used in TBC systems.

The oxidation experiments lasted for different times ranging from 0.1 to 500 h. Particular attention was paid to short oxidation times in order to detect whether transient alumina was formed at the initial oxidation stages.

Different oxidizing atmospheres have been used (air, and oxygen plus argon mixture) in order to detect possible formations of nitrides, which have been observed during the oxidation on other alumina-former alloys.

The surfaces of the RuAl samples were prepared prior to oxidation in two different ways: (i) by polishing, and (ii) by grinding. The choice of using 600SiC paper for grinding the samples was motivated by the wish of getting closer to the real working conditions.

In addition, thermogravimetric analyses (TGA) and X-ray diffraction (XRD) were performed during oxidation in order to investigate in-situ the growth of the TGO.

The oxidized samples were characterized using XRD, scanning electron microscopy (SEM), and transmission electron microscopy (TEM).

The results showed the formation of an  $\alpha$ -Al<sub>2</sub>O<sub>3</sub> layer on top of a  $\delta$ -Ru layer. The  $\delta$ -Ru phase forms during oxidation because of the depletion of Al in the RuAl substrate. In fact RuAl has a small stoichiometric gap, which induces a fast phase transformation due to the Al depletion. After oxidation a compositional modulation was observed in the RuAl substrate, which may rise from a self-rearrangement of the Al vacancies prior to the transformation to  $\delta$ -Ru phase. This may suggest an orientation influence of the RuAl upon the  $\delta$ -Ru formation.

Cross section investigations of the oxide scale presented an equiaxed morphology next to the gas phase and a columnar morphology next to the  $\delta$ -Ru phase. There is evidence, which suggests a growth mechanism of the TGO based on a simultaneous inward diffusion of oxygen and an outward diffusion of Al.

The formation of  $\alpha$ -Al<sub>2</sub>O<sub>3</sub> needles has also been observed at the gas/oxide interface. No transient crystalline alumina has ever been detected after the performed oxidations. It is suggested that the early-formation of the  $\delta$ -Ru phase enhances the nucleation of  $\alpha$ -Al<sub>2</sub>O<sub>3</sub>. During the early stages of the oxidation the microstructure of the scale is already well defined, showing the  $\delta$ -Ru and the  $\alpha$ -Al<sub>2</sub>O<sub>3</sub> layers. Interface instability between these layers and evaporation of gaseous Ru-oxides lead to the formation of large elongated cavities and alternating  $\alpha$ -Al<sub>2</sub>O<sub>3</sub>/ $\delta$ -Ru layers.

The  $\delta$ -Ru layer acts as a diffusion barrier for Al to migrate from the RuAl substrate to the oxide scale, and consequently renders the interface between the oxide and the metallic Ru unstable. In fact any inward protuberance of the interface shortens the diffusion distance, resulting in a favorite growing site. The wavy oxide/ $\delta$ -Ru interface and the stresses, induced by the oxide growth and the  $\delta$ -Ru formation, enhance the formation of cracks in the brittle  $\delta$ -Ru layer.

Cracks in the  $\delta$ -Ru layer act as free paths for oxygen to diffuse. Due to the low solubility of O in the  $\delta$ -Ru phase, the oxide grows preferentially at the crack-sites and at the  $\delta$ -Ru/RuAl interface. Therefore, the cracking of the  $\delta$ -Ru layer represents the way through which oxygen can pass through, embedding the  $\delta$ -Ru and creating the multilayer morphology. The growth of the oxide across the  $\delta$ -Ru layer renders the TGO wavy and develops out-of-plane stresses, which may induce cracks in the oxide.

Once the  $\delta$ -Ru is embedded in the  $\alpha$ -Al<sub>2</sub>O<sub>3</sub>, it can form cavities because of the evaporation of its gaseous Ru-oxides (RuO<sub>3</sub> and RuO<sub>4</sub>), which have a high partial pressure at 1100 °C. The gaseous Ru-oxides are supposed to find their way out through grain boundaries and cracks in the  $\alpha$ -Al<sub>2</sub>O<sub>3</sub> scale.

An amorphous oxy-nitride (Ru-Al-O-N) can be detected in the cavities after oxidation in air. This material is the outcome of the oxidation of the  $\delta$ -Ru phase. Compared to the oxidation in O<sub>2</sub> plus Ar, the oxidation in air showed a much less severe evaporation of

gaseous Ru-oxides. It is proposed that N strongly reduces the evaporation rate of the gaseous Ru-oxides by enhancing the stability of this amorphous phase.

In-situ measurements of Debye-Scherrer diffraction patterns from  $\alpha$ -Al<sub>2</sub>O<sub>3</sub> and  $\delta$ -Ru phases have been recorded during oxidation. The elliptical distortion of the diffraction rings has been analyzed in order to determine the in-plane strain.

The results showed that the stress in the  $\alpha$ -Al<sub>2</sub>O<sub>3</sub> is compressive at all times, with the largest stress appearing in early oxidation. This is in agreement with the fact that no transition aluminas have been observed. In fact, for alumina-formers at 1100 °C, a large tensile stress is commonly seen, which results from the  $\theta$  to  $\alpha$  phase conversion of the initial oxide. The residual stress, which develops during cooling in the oxide scale, is relatively small compared to other alumina-former alloys. In fact, as mentioned, the thermal expansion coefficients (CTE) of  $\alpha$ -Al<sub>2</sub>O<sub>3</sub> and RuAl are relatively comparable. The in-plane stress, calculated for the  $\delta$ -Ru phase, is obtained for two different orientations and the measured stresses behave differently during the oxidation.

In conclusion, the high-temperature oxidation of polycrystalline RuAl presented properties, which are very advantageous for a potential BC, such as (i) the direct establishment of  $\alpha$ -Al<sub>2</sub>O<sub>3</sub> during oxidation, and (ii) the relatively small stresses developed by the TGO during oxidation and cooling. But the formation of the  $\delta$ -Ru layer beneath the oxide scale appears detrimental for the TGO formation, because the evaporation of RuO<sub>3</sub> and RuO<sub>4</sub> does not allow a compact oxide to form.

Possible alternative routes to take advantage of the “good” properties of the Ru-containing alloys are: (i) to investigate alloying elements, which prevent the formation of the  $\delta$ -Ru phase, and (ii) to investigate the oxidation of RuAl on specific grain orientation, since evidences have been observed, which suggested a possible orientation-influence of the RuAl substrate.

## ZUSAMMENFASSUNG

Es ist bekannt, dass die Effizienz von Gasturbinen von der Arbeitstemperatur abhängt. Daher hat man in den letzten Jahrzehnten Untersuchungen an Legierungen mit höherem Schmelzpunkt und besseren mechanischen Eigenschaften durchgeführt. Eine erhebliche Verbesserung lieferte die Anwendung von multifunktionellen Beschichtungen, welche den thermo-chemischen Widerstand der einzelnen Komponenten erhöhen. Wärmedämmschichtsysteme (TBC) wurden zunächst eingeführt um die Haltbarkeit der metallischen Komponenten zu verbessern. Heute nutzt man die Tatsache, dass man sie bei höheren Temperaturen einsetzen kann.

In den heutigen Systemen, wird die thermische Isolierung durch eine äußere  $Y_2O_3$ , teilweise mit Zirkonium stabilisierte Schicht (YSZ), gewährleistet. Neben dieser Schicht wird eine weitere benötigt, um die darunter liegende Legierung vor thermischer Oxidation zu schützen, da die poröse YSZ Schicht Sauerstoffdiffusion zulässt. Dieser chemische Schutz wird durch eine dünne  $\alpha-Al_2O_3$  zwischen dem Metall und der thermischen Barriere gewährleistet. Diese Schicht wächst während der Oxidation und deshalb nennt man sie thermisch wachsende Oxidschicht (TGO). Diese TGO- Schicht stellt eine Diffusionsbarriere für den Sauerstoff dar. Zu diesem Zweck wird auf das Bauteil zunächst eine metallische Haftvermittlerschicht (Bond Coat BC) aufgebracht, die während der TBC Beschichtung eine thermisch wachsende Oxidschicht ausbildet. Die Haftvermittlerschicht enthält Elemente wie Al, Pt, Cr, Co und Y .

Eine Verbesserung dieser BC's stellt einen Schwerpunkt bei der Herstellung der TBC Systeme dar, weil die meisten Ausfälle durch eine Trennung an den Grenzflächen Metall-BC oder BC-TGO zustande kommen. Die Hauptursache der Ausfälle ist eine teilweise Knickung und die nachzufolgende Abplatzung der Schicht von der Superlegierung.

Die Anwendung von BCs, die Ru enthalten, hat sich als eine vielversprechende Alternative zu (Ni, Pt )Al erwiesen. Es wurde angenommen, dass Anwenden von Platingruppe Metallen in der Buffer-Schicht die Interdiffusion mit der Superlegierung minimiert. Die stöchiometrische Zusammensetzung von RuAl besitzt eine sehr gute Härte und Zähigkeit bei Raumtemperatur. Desweiteren besitzt RuAl einen hohen Schmelzpunkt, eine gute Kriechbeständigkeit sowie einen themischen

Ausdehnungskoeffizienten, der in der Größenordnung des  $\alpha$ - $\text{Al}_2\text{O}_3$  liegt. Aufgrund dieser Eigenschaften ist es ein guter potentieller Kandidat für Hochtemperaturanwendungen. Die Hauptaufgabe dieser Arbeit war es, das Oxidationsverhalten von RuAl zu untersuchen.

Alle Experimente wurden an nahezu stöchiometrischem RuAl durchgeführt, welches durch Lichtbogenofenschmelzen und Induktionsschmelzen hergestellt wurde. Alle Oxidationsexperimente wurden isotherm bei 1100 °C durchgeführt. Dies ist die übliche Arbeitstemperatur von BCs, welche in TBCs verwendet werden.

Die Dauer der Oxidationsexperimente variierte von 0.5-500h. Besondere Beachtung wurde den Kurzzeituntersuchungen gewidmet, um zu beobachten, ob sich während der ersten Oxidationsstufen besondere Oxide des Aluminiums bilden.

Unterschiedliche Oxidationsatmosphären wurden verwendet (Luft, sowie eine Sauerstoff-Argonmischung) um die Entstehung möglicher Nitride zu beobachten. Diese wurden schon bei anderen Al-bildenden Legierungen beobachtet.

Die Oberflächen der RuAl Proben wurden vor dem Versuch in folgender Weise präpariert: (i) Polieren, (ii) Schleifen. Bei den geschliffenen Proben wurde 600SiC Papier für das Schleifen verwendet, um näher an den Realbedingungen zu sein. Bei den polierten Proben wurde mit Diamant bis Körnung 1  $\mu\text{m}$  poliert.

Zusätzlich wurden thermogravimetrische Untersuchungen und Röntgenuntersuchungen durchgeführt, um das insitu-Wachstum der TGO-Schicht zu beobachten. Die oxidierten Proben wurden mit XRD, REM und TEM untersucht.

Die Ergebnisse zeigten die Bildung einer  $\alpha$ - $\text{Al}_2\text{O}_3$  -Schicht über einer  $\delta$ -Ru -Schicht, Das  $\delta$ -Ru bildet sich während der Oxidation infolge einer Al-Verarmung des RuAl-Grundwerkstoffes. Wegen des geringen Löslichkeitsbereiches der Phase RuAl geschieht der Übergang zum Ru-Mischkristall sehr schnell. Nach der Oxidation wurde eine Modulation der Zusammensetzung im Grundwerkstoff gefunden. Diese kommt durch Selbstorganisation der Leerstellen, die durch Al-Ausdiffusion entstanden sind, zustande. Dies legt einen Zusammenhang zwischen der Orientierung einzelner Al-Körner und der Bildung von  $\delta$ -Ru nahe.

Querschliffuntersuchungen des Oxides zeigten aequiaxiales Wachstum an der Außenseite und Stengelkristallwachstum zum  $\delta$ -Ru hin. Der ableitbare Wachstumsmechanismus des TGO besteht darin, dass es eine Eindiffusion von Sauerstoff und eine Ausdiffusion von Aluminium gibt.

Das Wachstum von  $\alpha$ - $\text{Al}_2\text{O}_3$  -Nadeln an der Atmosphärenseite wurde ebenfalls beobachtet. Andere Aluminiumoxide als  $\alpha$ - $\text{Al}_2\text{O}_3$  wurden zu keiner Zeit der Oxidation gefunden. Es wird angenommen, dass die frühe Bildung von  $\delta$ -Ru die Keimbildung von  $\alpha$ - $\text{Al}_2\text{O}_3$  begünstigt.

Während der Frühphase der Oxidation wird das Gefüge der Schicht schnell mit  $\delta$ -Ru und  $\alpha$ - $\text{Al}_2\text{O}_3$  -Lagen ausgebildet. Grenzflächeninstabilität zwischen diesen Lagen und die Abdampfung von Ru-Oxiden führt zur Bildung großer, lang gestreckter Poren und den abwechselnden Lagen von  $\alpha$ - $\text{Al}_2\text{O}_3$  und  $\delta$ -Ru.

Die  $\delta$ -Ru -Lagen wirken als Diffusionssperre für Al und destabilisieren die Grenzfläche zum Oxid hin. Protuberanzen des Oxids in Richtung Grundwerkstoff verkürzen den Diffusionsweg und verstärken sich dadurch selbst. Die wellenförmige Grenzfläche zwischen Oxid und  $\delta$ -Ru und die Spannungen fördern die Rissbildung im spröden  $\delta$ -Ru.

Risse in der  $\delta$ -Ru -Schicht wirken als bevorzugte Diffusionspfade für Sauerstoff. Wegen der schlechten Diffusion von Sauerstoff im Ru-Mischkristall wächst das Oxid bevorzugt in Rissen und an der Grenzfläche Ru-RuAl. Das Risswachstum wird deshalb als wesentlicher Mechanismus für die Bildung der Mehrlagenoxide angesehen. Das Wachstum des Oxids entlang der  $\delta$ -Ru -Lagen wird deshalb wellenförmig und die Spannungen bilden sich nicht in einer Ebene aus. Dies wiederum kann zu Rissen im Oxid führen.

Sobald  $\delta$ -Ru von  $\alpha$ - $\text{Al}_2\text{O}_3$  eingeschlossen, können sich bei Oxidation an Luft Poren wegen des Abdampfens von Ru-Oxiden ( $\text{RuO}_3$  und  $\text{RRuO}_4$ ) bilden. Diese Oxide haben bei 1100C einen hohen partiellen Dampfdruck. Es wird angenommen, dass die Gase entlang von Korngrenzen und Rissen im Oxid entweichen können.

In den Poren wurde nach Oxidation ein amorphes Oxinitrid (Ru-Al-O-N) gefunden. Im Vergleich zu einer Oxidation in Sauerstoff mit Argon wurde bei Oxidation an Luft weniger Abdampfung von Ru-Oxid gefunden. Es wird angenommen, dass Stickstoff die Abdampftrate durch die Bildung des Oxinitrides nennenswert heruntersetzt.



Es wurden In-situ-Messungen mit Debye-Scherrer-Technik während der Oxidation durchgeführt. Die elliptische Verzeichnung der Beugungsringe wurde zur Ermittlung der Spannungen ausgewertet.

Die Ergebnisse zeigten, dass im  $\alpha$ - $\text{Al}_2\text{O}_3$  stets Druckspannungen vorliegen. Dabei liegen die höchsten Spannungen im Frühstadium der Oxidation vor. Diese Ergebnisse stimmen damit überein, dass beim Anfangsstadium keine anderen Oxide gefunden wurden. Bei anderen Legierungen, die bei Aluminiumoxidbildung bei 1100°C einen Übergang von  $\gamma$  zu  $\alpha$ - $\text{Al}_2\text{O}_3$  durchmachen, werden in der Regel Zugspannungen gefunden. Die nach der Abkühlung im Oxid verbleibenden Spannungen sind im Vergleich zu  $\alpha$ - $\text{Al}_2\text{O}_3$  auf anderen Hochtemperaturwerkstoffen niedrig. Dies liegt daran, dass die thermischen Ausdehnungskoeffizienten von Oxid und RuAl annähernd gleich sind. Die ebenen Spannungen wurden für  $\delta$ -Ru in zwei Orientierungen berechnet. Die wahren Spannungen, die während der Oxidation auftreten, weichen davon vermutlich wegen einer Orientierungsabhängigkeit ab.

Zusammenfassend zeigte die Hochtemperaturoxidation von polykristallinem RuAl Eigenschaften, die ein Potential für einen Einsatz von RuAl als BC-Material darstellen. Diese bestehen (i) darin, dass sich  $\alpha$ - $\text{Al}_2\text{O}_3$  direkt während der Oxidation bildet und (ii) darin, dass sich bei der TGO-Bildung und bei der anschließenden Abkühlung wenig Spannungen aufbauen. Die Bildung der  $\delta$ -Ru -Lagen hingegen ist kritisch für die Bildung einer funktionellen TGO-Schicht, weil die Abdampfung der Ru-Oxide kein massives, fehlerfreies Oxid zulässt.

Mögliche weitere Wege, mit denen die hier gefundenen positiven Eigenschaften genutzt werden könnten, wären: Erstens die Untersuchung der Wirkung weiterer Legierungselemente, die die Bildung von  $\delta$ -Ru unterbinden und zweitens die Untersuchung der Oxidation in Abhängigkeit der Orientierung der Körner des Grundwerkstoffes.

## 1. INTRODUCTION

Multifunctional high-temperature coatings used in advanced gas turbines are required to operate under the most aggressive conditions encountered by structural components, and must survive thousands of cycles or thousands of hours of continued exposure. Through their ability to simultaneously provide thermal insulation and oxidation protection, these coatings have become the crucial element in the pursuit of improved efficiency and reduced environmental impact.

Thermal Barrier Coatings (TBCs) have been used in industry and technology for over 20 years [Mil97]. However, their benefits have yet to be fully realized because of the inadequacy of current materials and designs. Finding viable solutions requires enhanced fundamental understanding and predictive models governing design, deposition and performance.

TBCs are formed by multilayers having dual thermal/chemical functionality, deposited on actively cooled hot section components [Cla03]. They are used conservatively in current gas turbines since they lose adhesion and spall from the substrate, especially in those areas subject to high heat flux. A consistent improvement in engine technology would be if (i) a predictable life could be assured and (ii) materials with improved refractoriness ( $>1200$  °C) and chemical stability were discovered. Both of these tasks require a high of basic understanding about degradation mechanisms and the connection between the material responses and the evolving microstructure.

In present systems, thermal insulation is provided by an outer  $7 \pm 1$  wt. %  $Y_2O_3$  partially-stabilized zirconia (7YSZ) layer, about 125-250  $\mu\text{m}$  thick [Lev04]. Beneath this layer a chemical barrier is needed to protect the underlying superalloy from the thermal oxidation, because the porous 7YSZ is permeable to oxygen. Chemical protection is provided by a thin  $\alpha\text{-Al}_2\text{O}_3$  layer between the metal and thermal barrier. It evolves in-situ and hence is known as the thermally grown oxide (TGO). Ideally the TGO should be stable, dense, adherent, planar (to minimize out-of-plane tension) and grow as slowly as possible.

Since the underlying superalloys are not generally optimized for oxidation resistance, development of a durable chemical barrier requires modification of the surface chemistry. A buffer layer is formed by adding specific elements, such as: Al, Pt, Cr, Co, Y. This

buffer layer is known as the bond coat (BC), and can be applied as an over-layer or by diffusional treatments.

The thermally grown alumina is the major source of strain incompatibility that motivates failure. The critical features are the imperfections in the TGO. They convert the misfit stress into a driving force for failure by large scale buckling [Hut00]. Therefore, improving the BC can be regarded as the highest priority for emerging TBC systems. A successful achievement would be to discover an enhanced bond coat system that suppresses failure and provides reliable life.

The main objective of this thesis is to investigate the possibility of using Ru-containing BCs as an alternative to (Ni,Pt)Al, which represents so far the most suitable material for BCs. In fact, the use of platinum group metals (PGM) and Al in the bulk buffer layer enhances the availability of Al for the formation of the TGO and minimizes interdiffusion with the superalloy.

Ruthenium is the least expensive of the PGM and forms a continuous  $\beta$ -phase field with NiAl in the ternary Ni-Al-Ru system [Cha86]. Additionally, compared to NiAl, stoichiometric RuAl presents the same cubic B2 structure and possesses a greater number of slip systems. It has a very good room temperature, hardness and toughness. It possesses a high melting point, a coefficient of thermal expansion (CTE) close to that of  $\alpha$ -Al<sub>2</sub>O<sub>3</sub> and a good creep resistance [Fle91, Try04, LuD99] (Tab. 1.1). All these characteristics make this alloy a potential candidate for high temperature applications. Therefore, fundamental studies on the oxidation behaviour of polycrystalline RuAl bulk material have been performed.

Material	E (GPa) at RT	T <sub>M</sub> (°C)	Yield S. (MPa) at RT	Crystal Str.	Thermal exp. Coeff. $\alpha$ (K <sup>-1</sup> ) at RT / 1100°C
$\alpha$ -Al <sub>2</sub> O <sub>3</sub>	380	2050	---	Hexagonal	6,8x10 <sup>-6</sup> / 8,2x10 <sup>-6</sup>
RuAl	267	2060	145	B2	5,5x10 <sup>-6</sup> / 8,8x10 <sup>-6</sup>
NiAl	193	1638	50	B2	1x10 <sup>-5</sup> / 1,3x10 <sup>-5</sup>

Table 1.1. Comparison between the properties of  $\alpha$ -Al<sub>2</sub>O<sub>3</sub>, RuAl and NiAl [Try04].

The oxidation experiments have been conducted under different conditions at 1100 °C, which represents the desired working temperature of actual BC in TBC systems.

The results showed the formation of an  $\alpha$ -Al<sub>2</sub>O<sub>3</sub> layer on top of a  $\delta$ -Ru layer. Interface instability between these layers and evaporation of gaseous Ru-oxides can lead to the formation of large elongated cavities and alternating  $\alpha$ -Al<sub>2</sub>O<sub>3</sub>/ $\delta$ -Ru layers.

A similar behaviour under isothermal conditions has already been observed on the IrAl alloy [Cho90], where alternating layers of Al<sub>2</sub>O<sub>3</sub> and Ir-rich phase were produced after oxidation at 1300 °C. The layered structure has been discussed based on the diffusion kinetics of O, Al and Ir; and a mechanism based on alternating diffusion fluxes of Al and O through the Ir-rich phase has been suggested as the cause of such morphology.

Understanding the oxidation behaviour in the case of RuAl proved to be a challenging task. In fact, different techniques have been used in order to obtain a complete picture of the ongoing process, such as: thermogravimetric analysis (TGA), X-ray diffraction (XRD), Auger spectroscopy, scanning electron microscopy (SEM) and transmission electron microscopy (TEM).

In particular, thermogravimetric and in-situ diffraction measurements have been exploited to describe the kinetic growth and the stresses of the TGO during oxidation. Afterwards, the use of TEM focused on the microstructure of the TGO on lengthscales reaching from  $\mu\text{m}$  to  $\text{\AA}$ . This was essential for understanding and describing the peculiar kinetic-behaviour observed.

At the end, a model was developed, which describes the different steps occurring during oxidation, such as: (i) the formation of the double layer  $\alpha$ -Al<sub>2</sub>O<sub>3</sub>/ $\delta$ -Ru, (ii) the formation of the multilayered morphology, and (iii) the formation of the cavities due to the evaporation of Ru-oxides.

## 2. FUNDAMENTALS ON THE OXIDATION OF METALS AND ALLOYS

The majority of metals have a big affinity with oxygen, water, sulfur and carbon dioxide; the consumption of the metal and the loss of its mechanical properties under the attack of these components is called corrosion.

The corrosion consists in an electro-chemical reaction through which the metal oxidizes donating electrons to the reduced specie. The corrosion process might proceed fast even at RT due to the presence of a liquid electrolyte, which provides a high mobility to the different species (Wet Corrosion). In the case of high temperature oxidation the diffusion in the solid phase of the different elements is big enough to render the oxidation destructive even without the presence of the liquid phase (Dry Corrosion).

### 2.1 THERMODYNAMICS OF THE OXIDATION OF PURE METALS AT HIGH TEMPERATURE

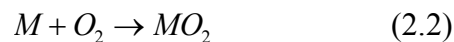
The study of oxidation phenomena requires the determination of the reactions energetically favored during the high temperature exposure. Equilibrium thermodynamics indicates the equilibrium state toward which the system moves and the driving forces of the reactions expressed in terms of free energy,  $\Delta G$ :

$$\Delta G = \Delta H - T\Delta S \quad (2.1)$$

where  $\Delta H$  indicates the variation of enthalpy,  $T$  the temperature and  $\Delta S$  the variation of entropy.

The free energy indicates the energy produced by the reaction, therefore a chemical process will proceed spontaneous when it releases energy ( $\Delta G < 0$ ). For  $\Delta G$  equal to zero the system is in equilibrium condition and for values higher than zero the reaction is thermodynamically impossible.

For the reaction,



where  $M$  stands for metal, the variation of free energy is

$$\Delta G = G_{MO_2} - G_M - G_{O_2} \quad (2.3).$$

The free energy of a component  $i$ ,  $G_i$ , is defined

$$G_i = G_i^0 + RT \ln a_i \quad (2.4)$$

where  $a$  stands for the activity,  $R$  is the universal gas constant and  $G^0$  is the standard free energy of formation calculated when all species are in their standard states.

Therefore the reaction (2.2) can be expressed in terms of free energy variation:

$$\Delta G = \Delta G^0 + RT \ln \frac{a_{MO_2}}{a_M a_{O_2}} \quad (2.5).$$

In the special case of equilibrium ( $\Delta G = 0$ ) the equation (2.5) reduces to

$$\Delta G^0 = -RT \ln \left( \frac{a_{MO_2}}{a_M a_{O_2}} \right)_{eq.} \quad (2.6).$$

The term in brackets is defined as **the equilibrium constant** ( $K_{eq}$ ) of the reaction.

When the alloy is formed by more elements which can oxidize, then the determination of the more stable corrosion products is required. Ellingham diagrams (Fig. 2.1) show the standard free energy of formation ( $\Delta G^0$ ) versus temperature of the most common oxidation reactions. These diagrams allow a comparison of the relative stabilities of the different compounds.

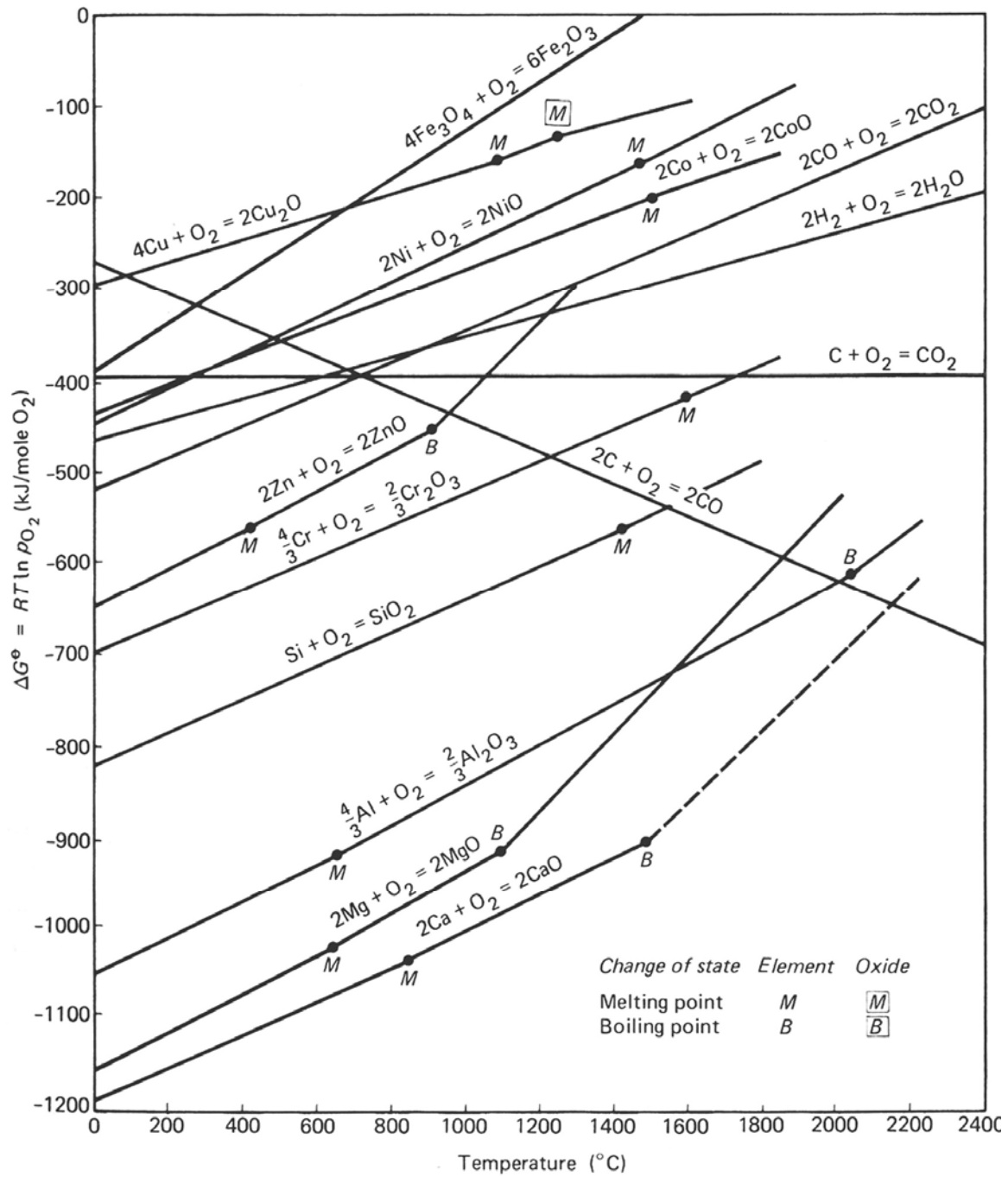
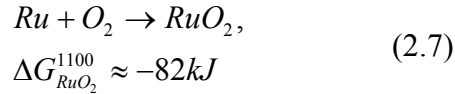


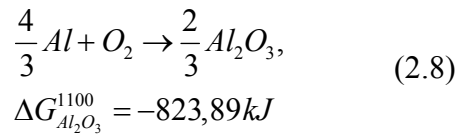
Fig. 2.1 Standard free energy of formation of selected oxides as a function of temperature [Bir 83].

In the case of RuAl the known stable solid oxides at 1100 °C are RuO<sub>2</sub> and Al<sub>2</sub>O<sub>3</sub>:

Ru-O system<sup>1</sup> [Bar89]:



Al-O system [Bar89]:



Energies are calculated for one mole of oxygen, O<sub>2</sub>.

Each solid phase in a thermodynamic system establishes an equilibrium condition with its own vapour phase. The equilibrium vapour pressure varies with temperature. At high temperatures the formation of vapour might influence the corrosion process itself. In this regard the vapour species diagram (Fig. 2.2) might indicate whether the partial pressures of the different components may influence the corrosion mechanism by plotting the pressure values versus the oxygen partial pressure.

For the construction of the diagram, all the reactions involved in the oxidation process must be taken into account. The equilibrium points of the reactions at the oxidation temperature must be calculated. The equation (2.6) is used to calculate the dissociation pressure of the oxide, which is defined as the oxygen partial pressure at which the metal and the oxide coexist.

In the case of Ru-O system

---

<sup>1</sup> Literature's data [Bar89] is reported until 1200 K, the values for the free energy of formation of solid RuO<sub>2</sub> are estimated considering a linear law in the variation of the energy value versus temperature.



$$\begin{aligned}
Ru + O_2 &\leftrightarrow RuO_2 \\
\Delta G^0 &= -RT \ln \left( \frac{1}{p_{O_2}} \right) \quad (2.9) \\
\Rightarrow \log p_{O_2} &= -3,04
\end{aligned}$$

where the activity of Ru and RuO<sub>2</sub> are taken as one ( $a_{Ru}, a_{RuO_2} = 1$ ), and  $\Delta G^0$  can be obtained from (2.7).

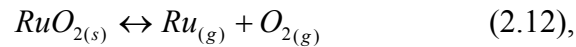
The equilibrium between Ru and RuO<sub>2</sub> is represented by the vertical line in Fig. 2.2. For lower values of the  $p_{O_2}$  Ru<sub>(s)</sub> is stable and Ru<sub>(g)</sub> does not depend on the oxygen partial pressure



and

$$\log p_{Ru} = \log K_p^{Ru_{(g)}} = -16,615 \quad (2.11)$$

When RuO<sub>2</sub> is the stable solid phase, then the vapour pressure of Ru can be calculated according to:



which results in

$$\log p_{Ru_{(g)}} = -19,66 - \log p_{O_2} \quad (2.13)$$

The diagram is completed calculating the pressures for the gaseous species of RuO<sub>3</sub> and RuO<sub>4</sub>.

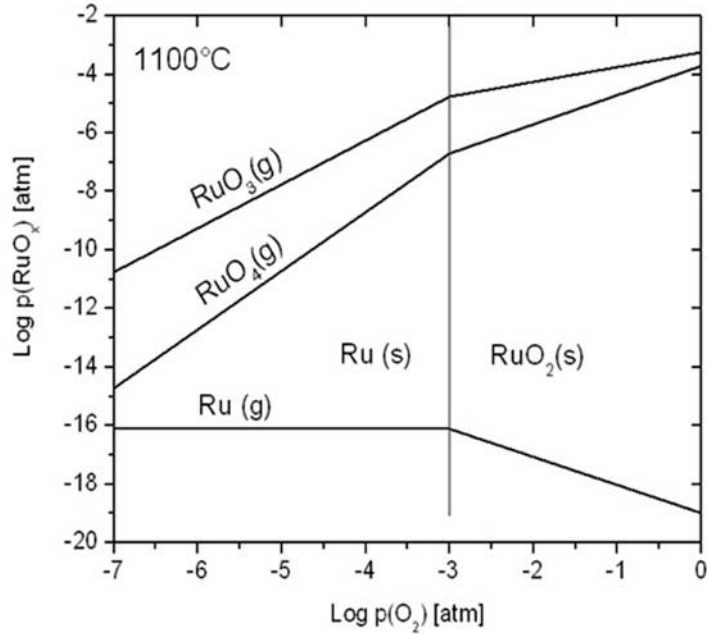


Fig. 2.2 Vapour Species Diagram of the Ru-O system at 1100°C (Thermodynamic data from [Bar89]).

## 2.2 KINETICS OF THE OXIDE GROWTH

The weight change of a specimen versus time during oxidation at high temperature, results in information on the kinetics. There are four characteristic behaviours that can be identified (Fig. 2.3): linear, parabolic, logarithmic and inverse logarithmic.

The linear behaviour is characteristic for an oxidation during which no protective oxide layer is formed. The parabolic behaviour is characteristic for the formation of a continuous and dense oxide layer, which protects the metal substrate by acting as a barrier against the oxidizing atmosphere. Logarithmic laws (direct and inverse) are typically observed at temperatures lower than 400 °C, where the initial oxide formation, up to 1000 Å range, is characterized by an initial rapid reaction that quickly reduces to a very low rate of reaction

The oxidation at high temperature proceeds in three steps: (i) diffusion of the oxidizing agent through the vapour phase, (ii) transport through the scale of the different components, and (iii) the chemical reaction.

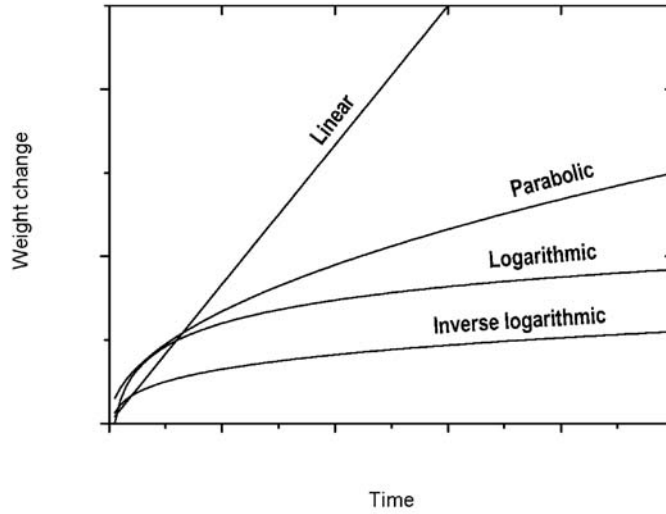


Fig. 2.3 Characteristic behaviours of dry corrosion.

If the scale is not protective, then the determining factor might be the diffusion through the vapour phase or the chemical reaction. Both these phenomena are independent of the thickness of the oxide scale; therefore there is no reason why the kinetics of the reaction should change in time. A linear law is obtained.

If the formed oxide scale is protective and continuous, then its growth can be described as the result of an electro-chemical migration of different species (anions, cations and electrons) through the oxide scale (Fig. 2.4).

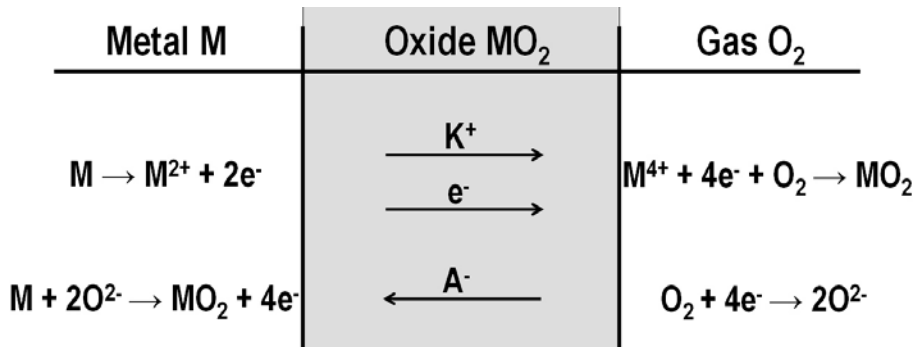


Fig. 2.4 Schematic diagram of the transport mechanism across the oxide scale:  $K^+$  stands for cations,  $A^-$  for anions and  $e^-$  for electrons.

Wagner's theory is still the most valid model to describe the scale growth [Wag33, Bir83].

With the following assumptions:

- 1) the oxide layer is continuous, dense and adherent,
- 2) the diffusion of ions and electrons across the scale is the rate controlling process,
- 3) thermodynamic equilibrium is present locally across the scale and at both the interfaces, metal/oxide and oxide/gas,
- 4) the oxide scale presents only small deviations from stoichiometry,
- 5) oxygen solubility in the metal is negligible,

Wagner's model predicts a parabolic behaviour:

$$\frac{dx}{dt} = e_{ox,ech} \frac{t_e(t_a + t_c)\Delta G}{\delta_{ox}\rho'zF} \frac{1}{x} \quad (2.14)$$

In the equation 2.14,  $x$  represents the thickness, and the other terms are constants during oxidation:  $e_{ox,ech}$  is the electrochemical equivalent of the oxide,  $\delta_{ox}$  is the density of the oxide,  $\Delta G$  is the free energy variation for the oxidation reaction,  $z$  is the number of charges involved in the oxy-reduction process,  $F$  is the Faraday constant and  $\rho'$  is the electrical resistivity of the oxide.

$t_e$ ,  $t_a$  and  $t_c$  represent the ratios between electronic, cationic, anionic currents and the total electrical current:

$$\frac{i_e}{i_{tot}} = t_e \quad \frac{i_c}{i_{tot}} = t_c \quad \frac{i_a}{i_{tot}} = t_a \quad (2.15)$$

The oxidation kinetics depends on  $t_e(t_a+t_c)$  and, since

$$t_e + t_c + t_a = 1 \quad (2.16),$$

the fastest oxidation rate belongs to the case in which the electronic current is equal to the ionic current,

$$t_e = t_a + t_c \quad (2.17).$$

An interesting observation following the previous conclusion is that oxidation kinetics can be reduced if one of the two conductive mechanisms is being reduced. This effect can be achieved by doping the alloy with some elements that would participate in the oxide formation [Bir83].

The oxides can be classified in n-type or p-type semiconductors; this classification is based on the sign of the electrical carriers. For n-type the carriers are negative and for p-type are positive. ZnO represents a good example of n-type semiconductor. In order to allow the metal excess in the compound is necessary to assume the presence of interstitial cations (ZnO is characterized by an excess of Zn,  $Zn_{1+x}O$ ). These cations, in order to maintain electroneutrality, result in an equivalent number of electrons in the conduction band and available for the charge migration.

In the n-type semiconductors the presence of metal doping elements with a smaller valence than the main metal element increases the interstitial metal cations and decreases the number of electrons, which are available for conduction. In the case when the oxidation kinetics is determined by ionic diffusion, doping will result in a faster growth.

In the p-type semiconductors the presence of metal doping elements with a valence smaller than the main metal element decreases the interstitial metal cations and increases the number of electrons available for conduction. If the oxidation kinetics is still determined by the ionic diffusion, then the doping will result in a slower growth.

This doping will only work if the doping elements are soluble in the grown oxide and until concentrations that do not allow the formation of new phases. For example, in the case of Ni-Cr alloys it happens that the spinel structure NiO-Cr<sub>2</sub>O<sub>3</sub> can form when the Cr content is too high.

### 2.3 OXIDATION OF ALLOYS

The case of having pure oxide and a pure metal is only a special case. There is often the case when the oxidation of alloys containing several metal elements raises consistently the level of complexity of the oxidation behaviour. The standard Ellingham diagrams give information about the most stable oxides. This can eventually not predict the oxidation reaction, since different activation energies of the reactions and the eventual formation of mixed oxides can create unexpected scenarios.

A classification of simple types of alloy oxidation has been proposed by Birks and Meier [Bir83]. The classification distinguishes the alloys in two groups: (a) noble parent with base alloying elements and (b) base parent with base alloying elements.

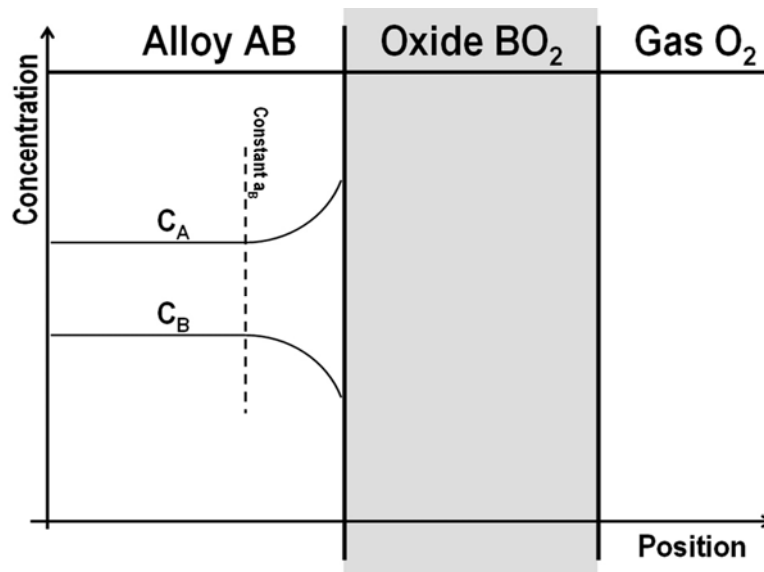


Fig. 2.5 Schematic representation of the concentration profiles for a general alloy AB, where A, noble metal, and B, base metal, have total miscibility.

The first group refers not only to alloys containing noble elements such as Au, Ag, Pt, but also to metals, such as Cu, Ni and Co, which form not very stable oxides and that at reduced oxygen activity conditions (e.g. under a dense oxide scale) might behave as a noble parent metal (Ru can also be considered a noble parent metal).

Due to the low solubility of oxygen in the noble (or noble parent) metal, the oxide cannot be formed by an internal oxidation. This results in an outward migration of the base metal of the alloy. If the noble metal is not solvable in the oxide layer, then an increase of concentration of the noble metal at the oxide/substrate interface will develop. A decrease of composition of the other metal will be observed owing to its consumption (Fig. 2.5).

When the concentration of the base metal next to the oxide/substrate interface is (i) high, then the rate determining factor is the diffusion across the oxide scale; when it is (ii) low, then the rate determining factor is the diffusion across the alloy.

Both processes are diffusion controlled and both result in a parabolic growth law.

An important aspect of the diffusion controlled mechanism is that the oxide/substrate interface becomes unstable (Fig. 2.6). For instance, every inward protusion shortens the diffusion distance and this enhances locally the oxidation rate by increasing the concentration gradient.

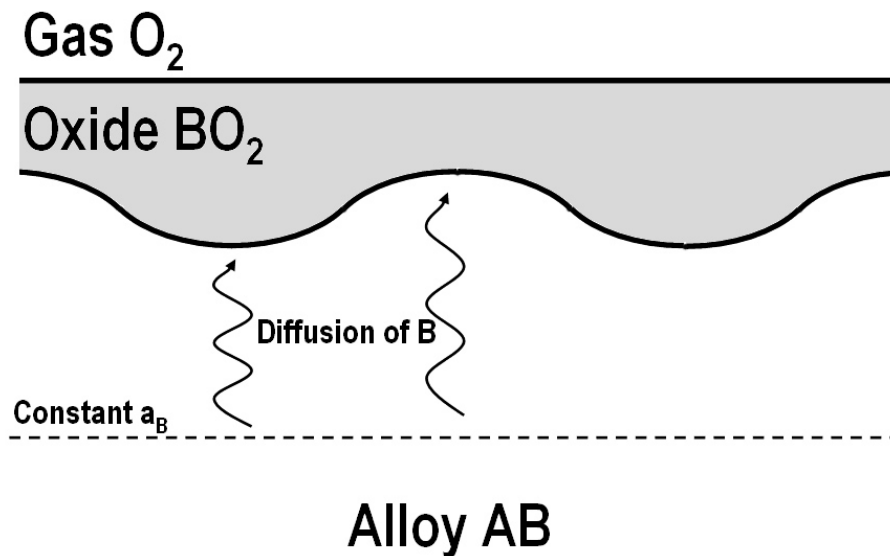
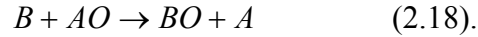


Fig. 2.6 Schematic representation of an unstable oxide/substrate interface forming due to an alloy interdiffusion process.

The oxidation mechanism is more complicated, when an alloy is composed of two elements AB, which can both form oxides AO and BO. Let's assume that BO is more stable than the oxide AO, according to the standard Ellingham diagrams. Then any AO formed in contact with B should convert to BO by the reaction



Nevertheless, if AO grows rapidly compared to BO and the conversion reaction is slow, AO can be the main oxide found in the TGO. The morphology of the TGO may also change significantly depending on the diffusion properties of the alloy. If A and B diffuse slowly through the substrate then two separate oxide layers will form; on the contrary, if the diffusion of A and B is rapid, then a mixed TGO is expected (Fig. 2.7).

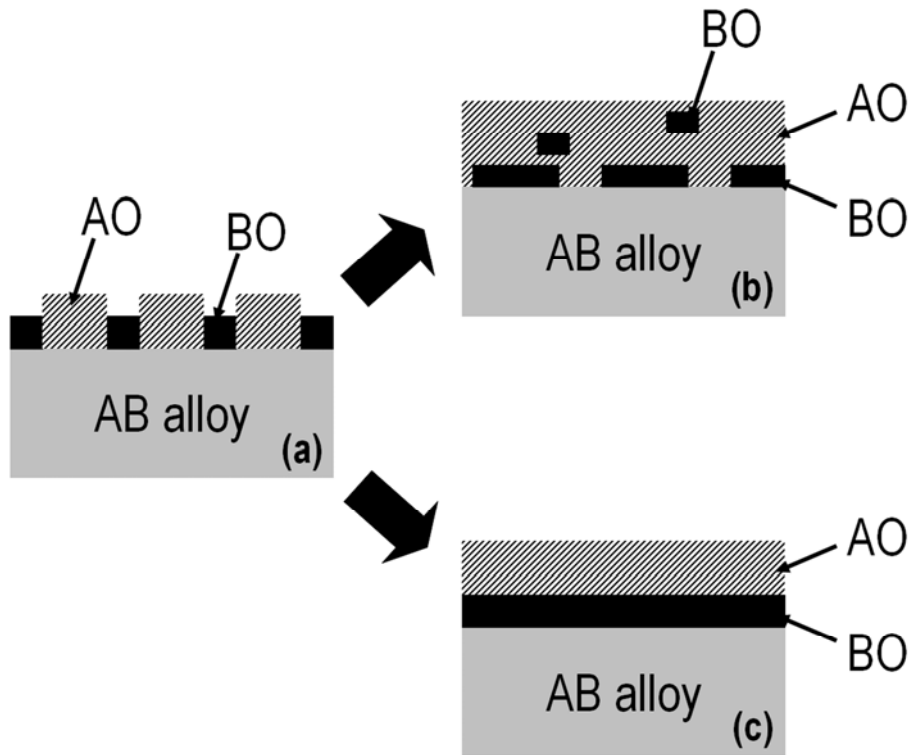


Fig. 2.7 Simultaneous growth of competing oxides. BO is thermodynamically more stable but the growth of AO is faster. (a) Initial stage shows the nucleation of both oxides. (b) A later stage is shown in case of rapid diffusion in the alloy. (c) A later stage is shown in case of slow diffusion in the alloy.



## 2.4 DIFFERENT OXIDIZING ATMOSPHERES

Oxygen is the most common oxidant; however it is difficult to have an oxidizing atmosphere of pure O<sub>2</sub>, it is almost impossible to avoid the presence of other gases. Some general aspects of the most common oxidizing environments will briefly be introduced.

The effect of **water vapour** at high temperature can result in an increase of the oxidation rate. It is suggested that the increase of the ion-transport might be caused by the incorporation of hydrogen in the oxide, which can change its defect-dependent properties. For instance, in the case of NiCrAlY coatings the enhanced kinetics has been attributed to the increase in Ni and Cr transport ions in the oxide [Zho04].

The presence of **sulfur** during the oxidation might lead to the formation of sulfur compounds which may alter drastically the properties of the oxide scale. For example the formation of sulfurs with a low melting temperature (i.e. Ni<sub>3</sub>S<sub>2</sub>) neglects a continuous and protective scale by offering favorites paths to the metal substrate. In addition, it has been suggested that sulfur segregation at the oxide-metal interface may be responsible of spallation even at very low concentrations [Smi91, Gra91].

**Combustion gases** are usually mixtures of CO, CO<sub>2</sub>, H<sub>2</sub>O, O<sub>2</sub> and N<sub>2</sub>. The concentration ratio between the different species determines the corrosive characteristic of the environment. In the case of a higher concentration of CO and CO<sub>2</sub> the atmosphere will enrich the substrate with C, and vice versa in the case of a higher concentration of the other gases, if the substrate contains C, there can be a C depletion.

In specific conditions, the presence of **nitrogen** can lead to the formation of nitrides that can influence the corrosion process. For instance, in the case of the high temperature oxidation of TiAl, the formation of titanium nitrides prevents the formation of a continuous Al<sub>2</sub>O<sub>3</sub> layer, resulting, then, in an enhanced oxidation [Lan97].

## 2.5 STRESSES IN THE TGO

The resistance to high temperature oxidation requires the formation of a continuous and dense protective barrier; therefore, the generation of stresses is an important aspect in the high temperature oxidation of metals.

There are two principal sources of stress: growth stress and thermal stress.

**Growth stresses**, which develop during the isothermal formation of the scale, may be generated by different reasons.

The stress, in the case of volume differences between the oxide and the metal, originates from the difference in the specific volume of the oxide compared with the one of the metal which is consumed in its formation: the sign of the stress may be related to the Pilling-Bedworth ratio,

$$PBR = \frac{V_{metal\_ion\_in\_oxide}}{V_{metal\_atom\_in\_metal}} = \frac{Md}{nmD} \quad (2.18)$$

where  $m$  indicates the atomic weight of the metal,  $d$  its density,  $n$  the number of metal atoms in the oxide molecule,  $M$  the molecular weight of the oxide and  $D$  its density.

If the Pilling-Bedworth ratio is smaller than one ( $PBR < 1$ ), then the oxide that forms cannot be continuous, and so cannot be protective.

The oxide is expected to be in compression for values of the Pilling-Bedworth ratio bigger than unity ( $PBR > 1$ ); then easily a continuous layer can be formed. For values much bigger than one, especially in systems in which the oxide grows at the scale/metal interface, the compression state of the oxide layer can lead to spallation.

At the initial stages of the oxidation, the first oxide that forms might have an epitaxial relationship with the substrate. In the case of a coherent interface, the mismatch of the lattice parameters between the oxide and the metal substrate will result in the formation of stresses. As the scale thickens, the epitaxial constraints are reduced; therefore this mechanism is probably significant only at the beginning of the oxidation process.

The depletion of one or more elements due to selective oxidation and the formation of internal oxides due to oxygen dissolution in the metal substrate may form compositional changes across the alloy that influence the lattice parameters leading to the formation of growing stresses. This type of stress is more significant in the case of alloys with high oxygen solubility, such as Nb and Ta.

During oxidation, high intense compressive stresses be generated across the oxide layer, when the oxide does not grow specifically at any interface, but forms within the scale

itself. The simultaneous inward diffusion of oxygen and outward diffusion of the metal cation is the cause of this stress formation [Cla03].

Recrystallisation processes in the oxide phase are also phenomena that can induce stresses. For instance, it is known that the oxidation of Al may result in a metastable  $\text{Al}_2\text{O}_3$ , which, depending on time and temperature, transforms eventually to the more stable  $\alpha\text{-Al}_2\text{O}_3$ . This phase transformation induces tensile stresses in the  $\alpha\text{-Al}_2\text{O}_3$  phase, due to its higher density compared to the  $\theta$  phase. [Tol00]

An important source of growth stresses arises due to the oxidation mechanism (anionic or cationic) and the curvature of the surface (convex or concave).

The oxide scale grows at the oxide/substrate interface (gas/oxide interface), when the oxidation mechanism is based on anionic transportation (cationic transportation).

In the case of cationic transport, for instance, the oxide will result in compression (tension) growing on a convex surface (concave surface), because the consumption of the substrate will move the oxide/substrate interface towards smaller surfaces (larger surfaces) (Fig. 2.8).

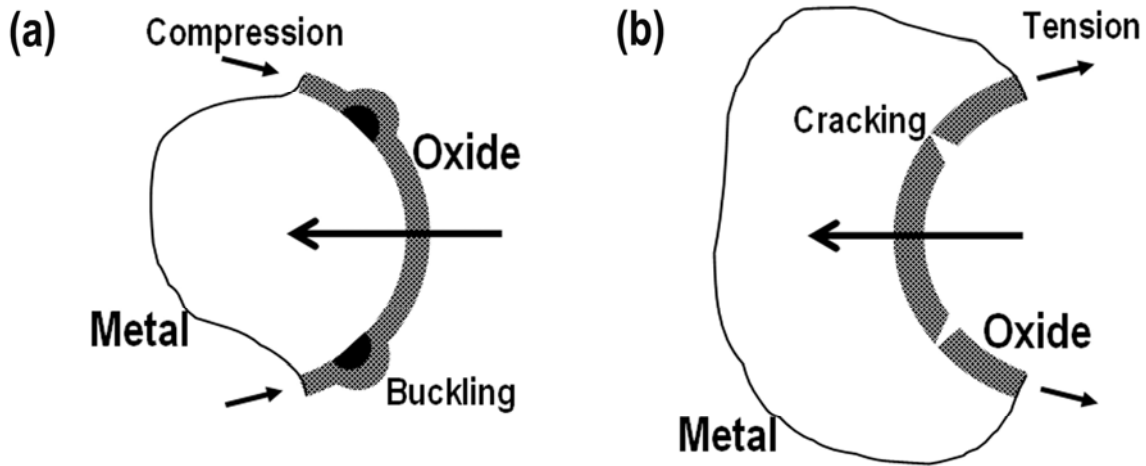


Fig. 2.8 Stresses generated in the oxide scale due to surface curvature during a cationic-transport oxidation-mechanism. The big arrow indicates the shifting direction of the oxide/substrate interface due to the metal consumption of the substrate. a) convex surface, b) concave surface.

Stresses will also be generated during cooling due to different thermal expansion coefficients of the metal and oxide. These are **thermal stresses**. The magnitude of these stresses is expressed as [Bir83]

$$\sigma_{ox} = \frac{E_{ox} \Delta T (\alpha_{ox} - \alpha_m)}{1 + 2 \left( \frac{E_{ox} t_{ox}}{E_m t_m} \right)} \quad (2.19)$$

where  $E$  is the elastic modulus,  $\alpha$  is the coefficient of thermal expansion and  $t$  is the thickness.

The subscripts ox and m stand for the oxide and the metal substrate respectively. The coefficient of thermal expansion for the oxide is generally smaller than that of metals, and so, commonly, the oxide after cooling is in a compressive state. The presence of thermal stresses generally results in the spallation of the oxide from the metal surface.

### 3. LITERATURE OVERVIEW

#### 3.1 THE THERMAL BARRIER COATING SYSTEM

##### 3.1.1 The Top Coat

Thermal Barrier Coatings (TBC) consist in a system meant to protect the parts exposed to the higher temperatures in gas turbine engines by covering them with a ceramic layer (Fig. 3.1).

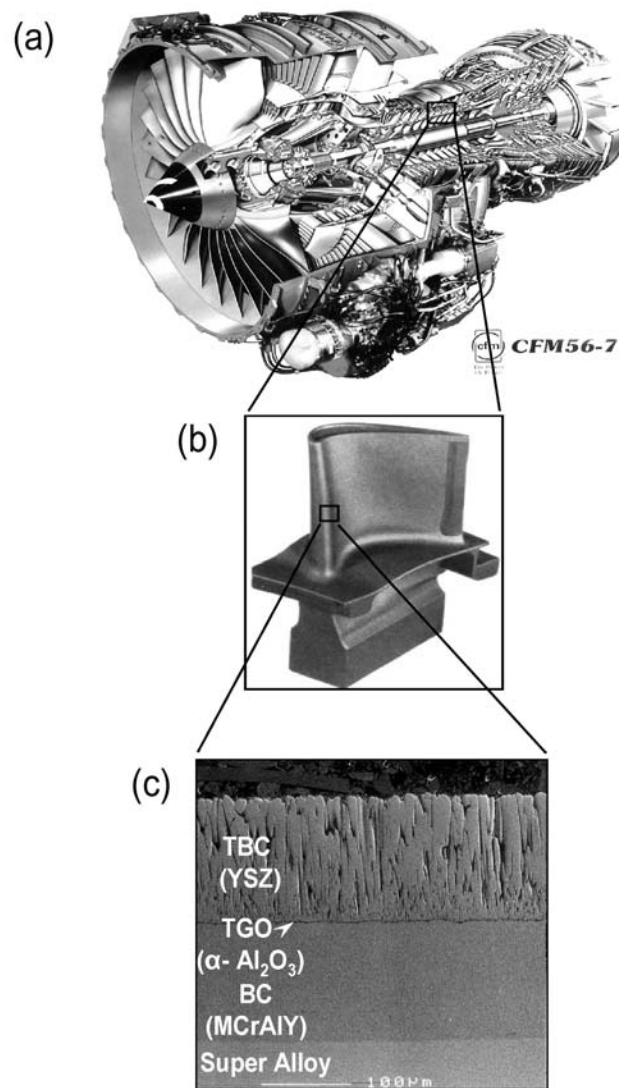


Fig. 3.1 Schematic representation of (a) airplane engine, (b) turbine blade, (c) TBC system. (Courtesy of Boriana).

The TBC system was firstly adopted in order to improve the durability of the metal components. Nowadays it is considered as a prime reliant element since it can offer an improvement in temperature capability of almost 200 °C, equivalent to three generations of progress in alloy design. The evolution over the years of the commonly known superalloys is shown in Fig. 3.2.

The progress achieved was based originally on material advances, where the efforts have been concentrated in the research of alloy compositions that are both more creep resistant and oxidation resistant. The improvements in casting techniques, then, have facilitated (i) the formation of large single-crystal blades, (ii) the creation of the internal channels in the blades necessary for cooling and (iii) the development of a coating technology to deposit the thermally insulating layer.

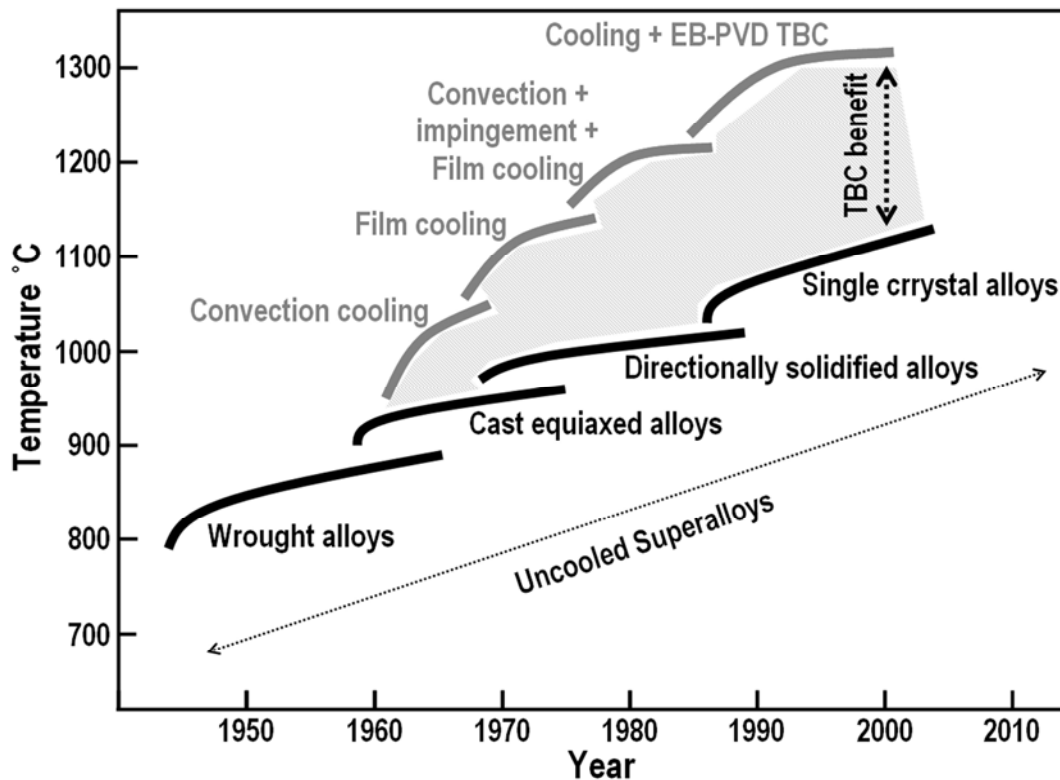


Fig. 3.2. Increase in working temperature over the last six decades through materials advances and cooling temperature techniques developments. [Cla03].

The schematic drawing in Fig. 3.1c describes the generic constituents of the TBC system: top coat, TGO and BC.

The top coat is a 125-250  $\mu\text{m}$  layer of porous  $\text{ZrO}_2$  partially stabilized with  $7 \pm 1$  wt. %  $\text{Y}_2\text{O}_3$  (7YSZ), applied either by air plasma spray (APS) or electron-beam physical vapor deposition (EB-PVD) [Lev04]. The requirement for this top coat is that it must have a low thermal conductivity with good strain tolerance, corrosion resistance and erosion resistance since it is directly in contact with the hostile atmosphere of the engine. Morphological phase stability is also necessary in order to avoid residual stresses, caused by volume changes during phase transformations, which may form cracks and enhance the spallation of the coating.

In particular, thermal expansion mismatch with the underlying substrate compromises survivability upon severe thermal cycling, inherent in engine operation. In the case of EB-PVD coatings, the lateral strain compliance results from the columnar structure and inter-columnar gaps produced during deposition [Cla03].

### **3.1.2 The Thermal Grown Oxide and Bond Coat**

Beneath the top coat a chemical barrier is needed to protect the underlying superalloy from the thermal oxidation, because the porous 7YSZ is permeable to oxygen. This chemical protection is based on the formation of a thermally grown oxide (TGO), which forms either during processing or service, and consists of a thin ( $<10 \mu\text{m}$ ) and dense oxide layer that prevents further oxidation.

So far the designed materials for a TGO is  $\alpha\text{-Al}_2\text{O}_3$  [Lee85] because of its thermodynamic stability, its compatibility with YSZ on exposure to air at high temperature, low oxygen diffusivity, and its remarkable thermally insulating properties [Cla03, Lev04].

In order to obtain a continuous and protective TGO, the surface of the superalloy must be chemically modified. These modified surfaces are called bond coats (BCs) and are divided in two major groups. The first group (i) consists in single phase  $\beta\text{-(Ni,Pt)Al}$  (B2 structure), applied by electrodeposition of Pt and subsequent aluminizing by some form of chemical vapor deposition (CVD) with concurrent interdiffusion. The second group

(ii) consists in overlying two-phase ( $\gamma' + \beta/\gamma$ ) MCrAlY's, applied by low pressure plasma spray (LPPS) or by EB-PVD [Nic03], where M refers to one or more of the elements Co, Ni, and Fe [Lev04].

In particular the aluminizing process exploits the interdiffusion properties of Ni (from the superalloy), Pt (from the electrodeposition) and Al (from CVD). Varying the temperature and the Al activity, it is possible to control the process in order to obtain a single phase  $\beta$ -(Ni,Pt)Al.

The selection of the two classes of alloys for BCs,  $\beta$ -(Ni,Pt)Al and ( $\gamma' + \beta/\gamma$ ) MCrAlY's, is primarily based on their prior use as oxidation and corrosion resistant coatings for alloys at high temperature working conditions.

Bond coat oxidation has been clearly established as a factor contributing to the failure of a TBC (Fig. 3.3). It is well known that BC properties of oxidation, creep, coefficient of thermal expansion (CTE) and roughness, all strongly influence ceramic layer stresses. BC oxidation, for example, has been clearly linked to the spallation of the ceramic top coat.

Therefore, the quest for materials feasible for BCs is based on specific properties. The major requirements for BCs are (i) outstanding mechanical properties (yield/creep strength to minimize cyclic plasticity effects); (ii) good diffusion stability, to reduce interdiffusion with the substrate; and (iii) be an efficient TGO former. The grown TGO must act reliably as a stable oxide diffusion barrier; it must adhere to thermal barrier and BC, and must possess a very slow growing rate in order to reduce the concomitant increase of strain energy.

During high temperature oxidation also transient  $\text{Al}_2\text{O}_3$  phases ( $\theta$  and  $\gamma$ ) may form, especially at temperature lower than 1000 °C. Their formation is generally undesirable in TBCs, since (i) they are characterized by a larger growing rate [Bru92] and (ii) the transformation to the stable  $\alpha$ -phase is always connected to a volume shrinkage which induces dangerous strains in the oxide scale [Tol00].

Different techniques have been developed in order to enhance the direct formation of the stable  $\alpha$ -phase, avoiding transient alumina to form. These techniques are based on surface preparation of the BC either by mechanical or chemical treatments. It has been reported that (i) the nucleation of  $\alpha$ - $\text{Al}_2\text{O}_3$  is easier on rougher surfaces [Tol00] and (ii) the formation of  $\alpha$ - $\text{Al}_2\text{O}_3$  is enhanced by doping the BC surface with elements like Fe



and Cr; these two elements form oxides with the same crystal structure as  $\alpha$ -Al<sub>2</sub>O<sub>3</sub> during a controlled pre-oxidation prior to TBC deposition [Sch00, Spi03].

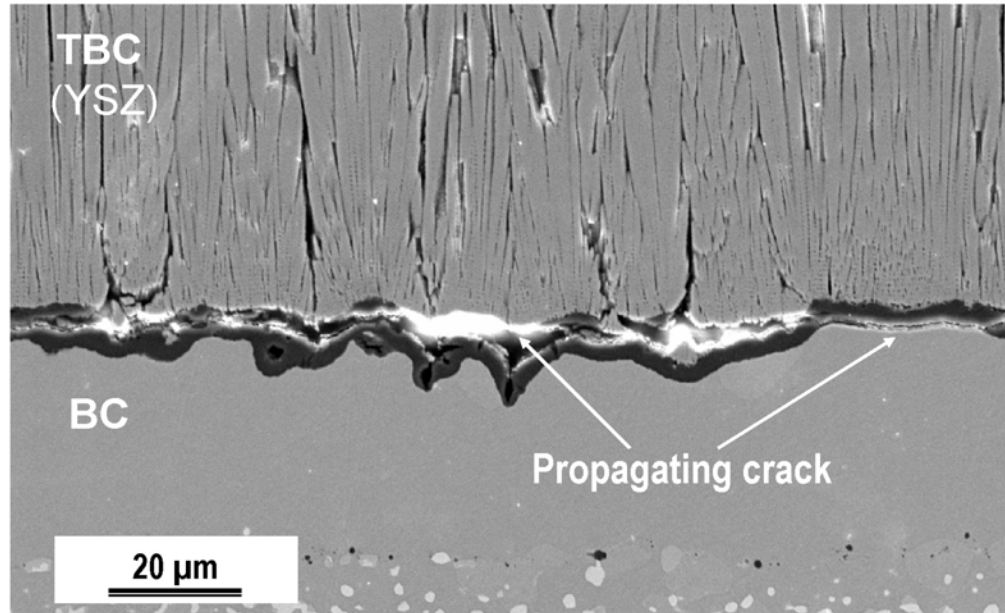


Fig. 3.3. SEM micrograph of a crack propagating at both the TBC/TGO and TGO/BC interfaces.

## 3.2 DESCRIPTION OF THE SYSTEMS INVOLVED IN THE OXIDATION OF RuAl

### 3.2.1 The RuAl system

RuAl is an intermetallic compound with a B2 (cP2) structure (Fig. 3.4) which unlike most structural intermetallics, is found to combine a very high melting point, high-temperature strength, and room-temperature toughness [Fle91]. Fleisher tested several compositions of RuAl and in Tab. 3.1 some of the mechanical properties are presented. Also of interest is that RuAl has a lower CTE than other common B2 aluminides (Fig. 3.5) [Try04].

The RuAl alloys exist over a range of different compositions (Fig. 3.6). It has been reported that off-stoichiometry compositions in the Ru-rich area lead to the formation of a thin region of Ru or Ru plus RuAl eutectic phase wetting the RuAl grain boundaries [Wol96]. This factor has been shown to enhance the ductility of the material [Fle91].

The TEM investigation evidenced the presence of Ru acicular precipitates which appear to have favorite orientation dependence in the RuAl matrix, even after annealing at 1350 °C for 20 h [Fle91].

Nominal Atomic Composition	Measured Atomic Composition	Melting Temperature (°C)	Young's Modulus (GPa)	Volume Fractions Observed
AlRu	52:48	2060	267	1.0
Al <sub>53</sub> Ru <sub>47</sub>	55:45	1920	242	0.99
Al <sub>48.5</sub> Ru <sub>51.5</sub>	45:55	1940	277	0.98
Al <sub>47</sub> Ru <sub>53</sub>	50:50	1920	280	0.93

Tab. 3.1 Some mechanical properties of different RuAl compositions. [Fle91].

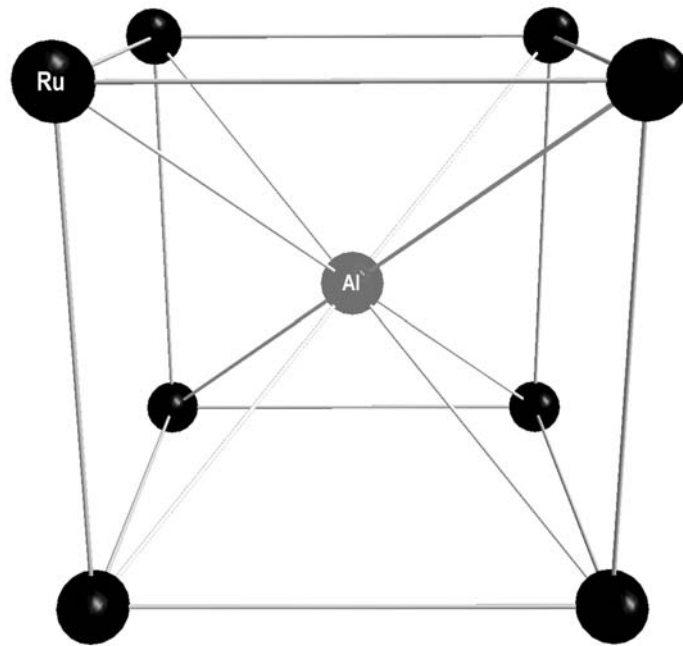


Fig. 3.4 Crystalline structure of RuAl.

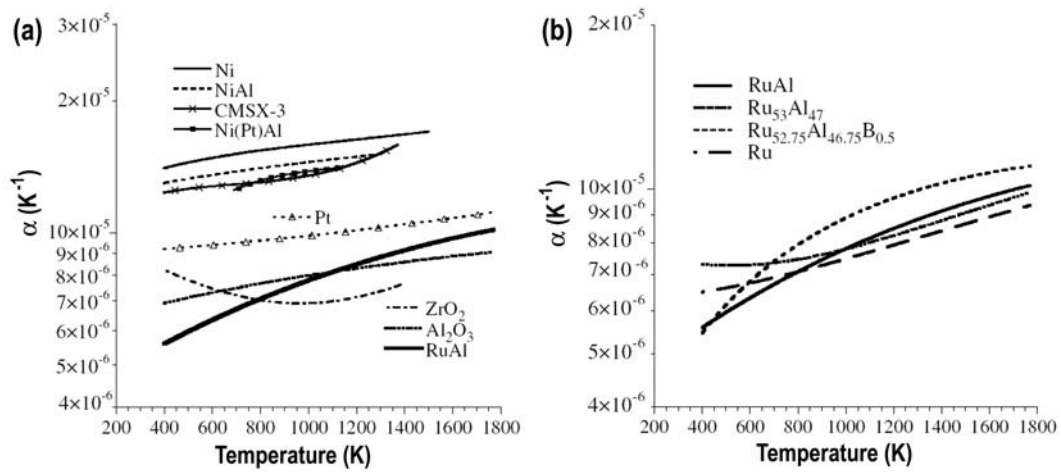


Fig. 3.5 Thermal expansion coefficients for different materials used in TBC systems (a) and for different RuAl compositions (b). [Try04].

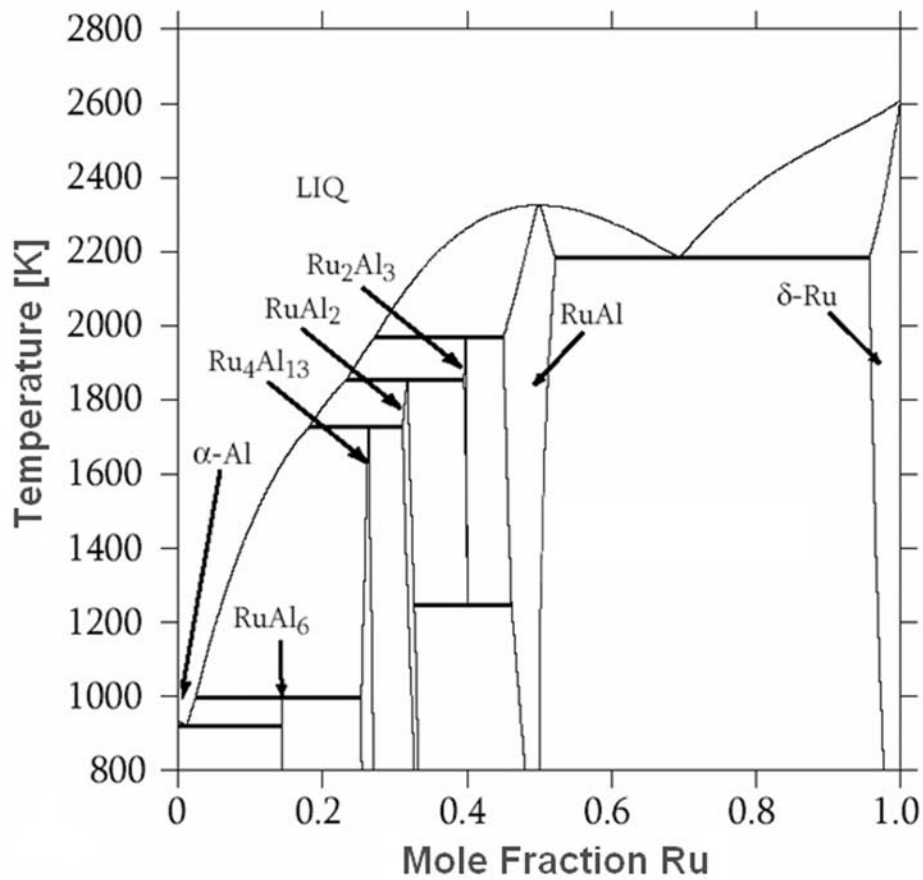


Fig. 3.6 Ru-Al phase diagram. [Pri03].

### 3.2.2 The Ru-O system

Metallic Ru (Tab. 3.2) reacts with oxygen forming three stable phases: solid  $\text{RuO}_2$ , and gaseous  $\text{RuO}_3$  and  $\text{RuO}_4$ .  $\text{RuO}_2$  is tetragonal and has two atoms per unit cell [Gol58].

Property	Ru
Atomic Number	44
Atomic Weight	101.07
Lattice Structure	Hcp

Tab. 3.2 General information about Ru.

The gaseous Ru-oxides form at temperatures above 800 °C depending on temperature and pressure (see the following par. 3.4). In Fig. 3.7 is reported the vapour phase diagram for the Ru-O system (calculated previously, see par. 2.1).

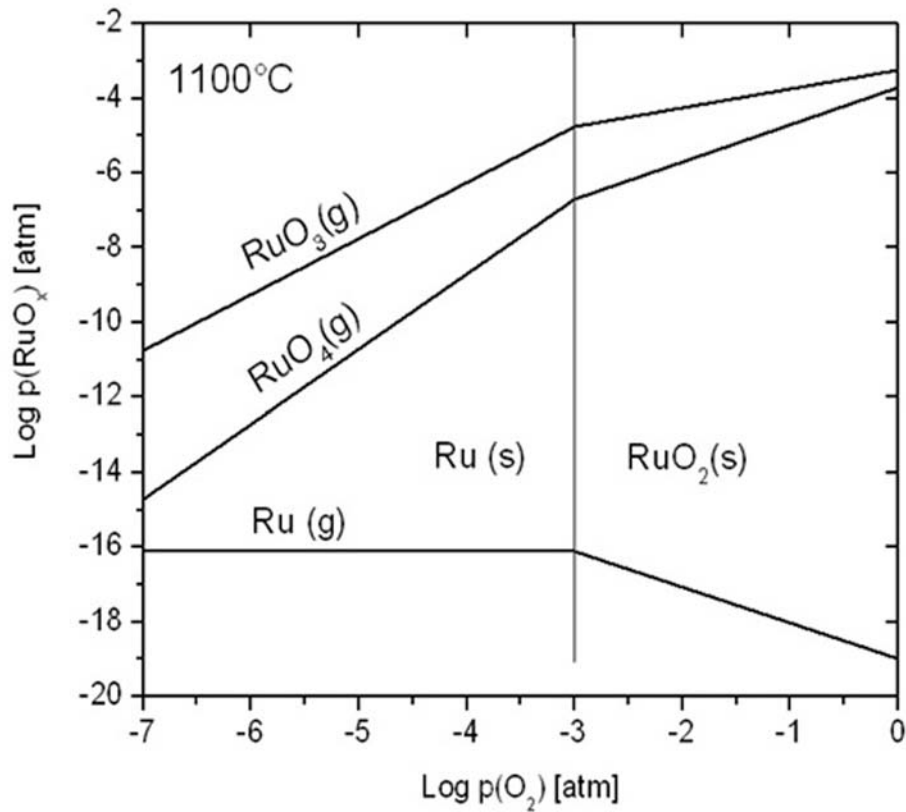


Fig. 3.7 Vapour phase diagram for the Ru-O system.

### 3.2.3 The Al-O system

Alumina ( $\text{Al}_2\text{O}_3$ ) is a very important ceramic material, which has many technological applications. It is an insulator with great hardness, chemical inertness and high melting point.

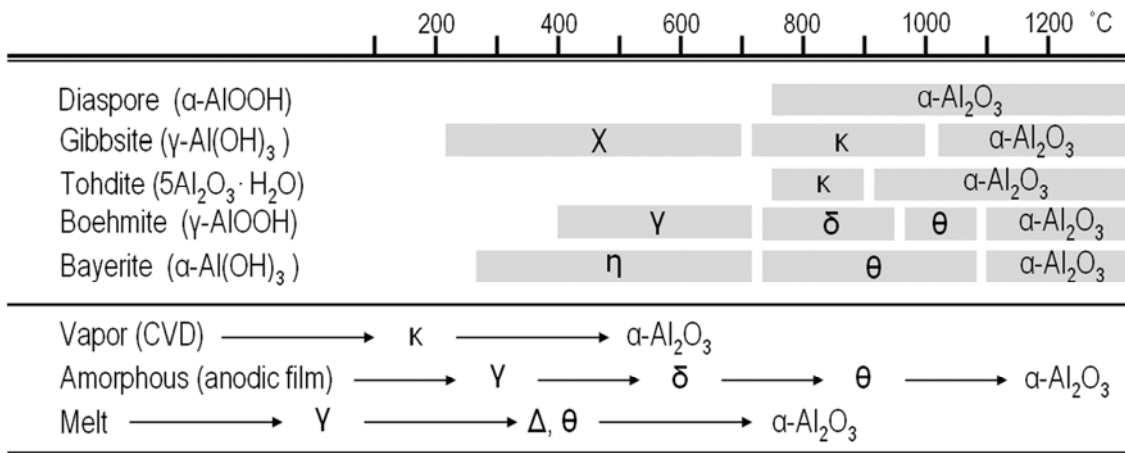
Besides the thermodynamically stable  $\alpha$ - $\text{Al}_2\text{O}_3$  (sapphire or corundum) there are several metastable phases of alumin (transition aluminas), which form at temperatures lower than 1100 °C.

There have been identified five different aluminum hydroxides: gibbsite, bayerite, nordstrandite, diaspore and boehmite [Stu50]. It has been showed that between the temperatures of dehydroxilation of the aluminum hydroxides and the  $\alpha$ -phase crystallization, several intermediate crystalline structures are formed [Lev98, San00] (Tab. 3.3).

There are seven different  $\text{Al}_2\text{O}_3$  phases, and only the  $\alpha$ -phase is thermodynamically stable:  $\chi$ -,  $\kappa$ -,  $\gamma$ -,  $\delta$ -,  $\theta$ -,  $\eta$ -,  $\alpha$ - $\text{Al}_2\text{O}_3$ .

- 1)  $\chi$ - $\text{Al}_2\text{O}_3$  forms from gibbsite,  $\gamma$ - $\text{Al}(\text{OH})_3$ . It has an hexagonal crystal structure where the aluminum cations occupy octahedral interstitial sites within the hexagonal oxygen layers. The arrangement of the layers in  $c$ -axis is strongly disordered [Lev98, San00].
- 2)  $\kappa$ - $\text{Al}_2\text{O}_3$  forms from  $\chi$ - $\text{Al}_2\text{O}_3$  and transforms to  $\alpha$ -phase above 1000 °C. It has an orthorhombic crystal structure with close-packed planes of oxygen in an ABAC stacking sequence along the  $c$ -axis. Al cations occupy for  $\frac{1}{4}$  tetrahedral positions and for  $\frac{3}{4}$  octahedral [Lev98].
- 3)  $\gamma$ - $\text{Al}_2\text{O}_3$  forms from monohydroxide boehmite,  $\gamma$ - $\text{AlOOH}$ . It has a fcc crystal structure where the stacking sequence of oxygen planes in the  $c$ -axis is ABCABC. This structure is often described as a defect cubic spinel structure with vacancies on part of the cations positions [Lev98].
- 4)  $\delta$ - $\text{Al}_2\text{O}_3$  forms from  $\gamma$ - $\text{Al}_2\text{O}_3$ . Its structure has been described as a superlattice of the  $\gamma$ -spinel structure with ordered cation vacancies [Wil79].

- 5)  $\theta$ - $\text{Al}_2\text{O}_3$  forms from  $\delta$ - or from  $\eta$ -  $\text{Al}_2\text{O}_3$ . It has a monoclinic symmetry where the aluminum cations are equally distributed over octahedral and tetrahedral sites. It has been reported that the structure is multiple twinned, primary on the (001) plane [Wil79].
- 6)  $\eta$ - $\text{Al}_2\text{O}_3$  forms from bayerite,  $\alpha$ - $\text{Al}(\text{OH})_3$  or from boehmite. Its structure has been described as defect spinel structure, similar to  $\gamma$ -phase. The differences between  $\eta$ - and  $\gamma$ -structures consist in a different tetragonally distortion ( $c/a$  ratio 0.985-0.993 for  $\eta$ , 0.983-0.987 for  $\gamma$ ) and a more ordered oxygen sublattice of the  $\gamma$ -structure [Lev98].
- 7)  $\alpha$ - $\text{Al}_2\text{O}_3$  is the only stable alumina phase at all temperatures. In this material the coordination number for Al is six with a valence of three; therefore four  $\text{Al}^{3+}$  are required next to each  $\text{O}^{2-}$  [Kin76]. Although its structure is rhombohedral, it is often described as an approximately hcp arrangement of  $\text{O}^{2-}$  anions with  $\text{Al}^{3+}$  cations occupying two-thirds of the octahedral interstices [Lee85], as shown in Fig. 3.8. The fact that only two thirds of the octahedral interstices sites are occupied gives to the crystalline structure a certain distortion.



Tab. 3.3 Sequences of phase transformations towards stable  $\alpha$ - $\text{Al}_2\text{O}_3$  phase. [Lev98].

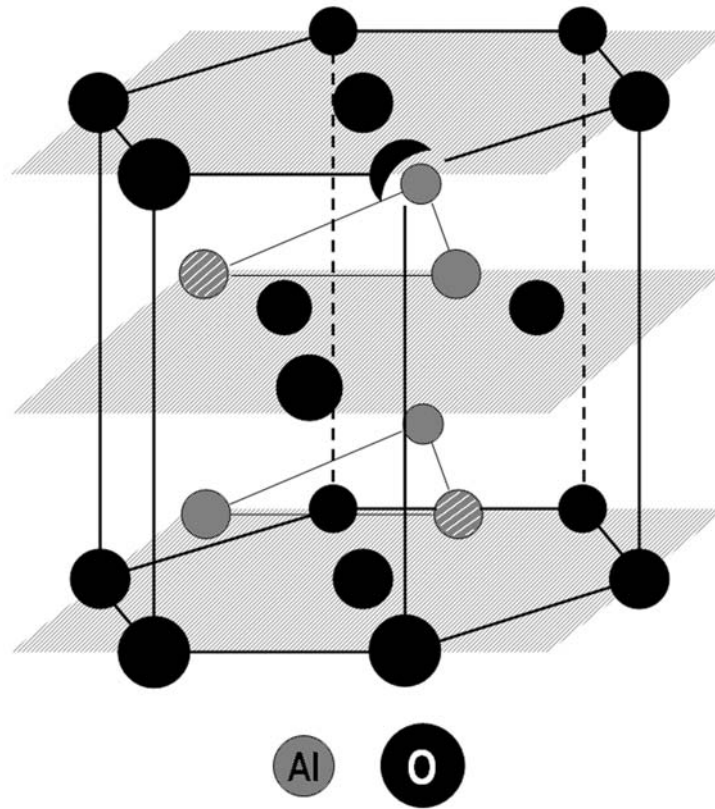


Fig. 3.8 Crystalline structure of  $\alpha$ - $\text{Al}_2\text{O}_3$  phase. The Al atoms fill two-thirds of the octahedral interstices.

### 3.3 OXIDATION AT HIGH TEMPERATURE OF IrAl, Ru AND RuAl

#### 3.3.1 High temperature oxidation of IrAl alloy [Cho90]

IrAl is an intermetallic alloy with a B2 crystal structure as RuAl and has a phase diagram similar to that of RuAl (Fig. 3.9).

Cho and al. performed oxidation experiments on IrAl (50-50 at%), at 1300 °C and 1600 °C for different times. The results showed the formation of an  $\text{Al}_2\text{O}_3$  scale accompanied by an Ir-rich phase next to the oxidized areas. This phase showed a similar to pure Ir crystal structure.

All the oxidation experiments evidenced only a weight loss, which was attributed to the formation of gaseous Ir-oxides ( $\text{IrO}_2$  and  $\text{IrO}_3$ ).

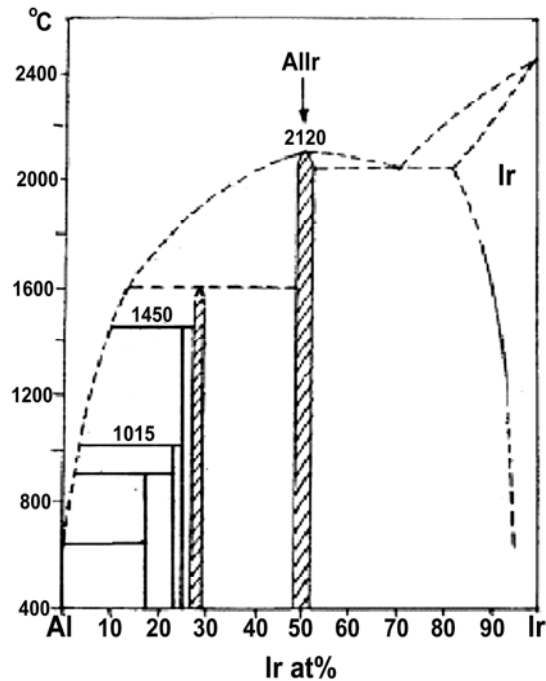


Fig. 3.9 Ir-Al phase diagram. [Mof77].

Unlike the oxidation of RuAl samples, the surfaces of the oxidized IrAl samples did not present bare metals areas, showing to be completely oxidized. The alumina analyzed by Raman microprobe resulted only  $\alpha$ -phase.

The cross section of the oxidized samples showed alternating layers of  $\text{Al}_2\text{O}_3$  and Ir-rich phase (Fig. 3.10). In the areas close to the surface only oxide layers are observed: the Ir-rich phase layers are supposed to be lost due to evaporation.

The nucleation and growth of  $\text{Al}_2\text{O}_3$  is not expected to occur in the Ir-rich phase layer, due to the low concentrations of both Al and O. Instead the discontinuities of the  $\text{Al}_2\text{O}_3$  layer are believed to form due to Al and O diffusion fluxes.

The inward diffusion of oxygen across the Ir-rich phase is suggested by Chou to be fast by considering (i) *the low solubility of oxygen in Ir-rich phase*, (ii) *the existence of the IrAl alloy as an oxygen diffusion sink*, and (iii) *the availability of vacancies in the Ir-rich phase layer as a result of the depletion of Al atoms*.



It is concluded that the overall oxidation process is affected by a relative slow Al diffusion kinetics compared to the O diffusion kinetics. Once the growth of an  $\text{Al}_2\text{O}_3$  layer is interrupted, a new pair of layers,  $\text{Al}_2\text{O}_3$  and Ir-rich, forms.

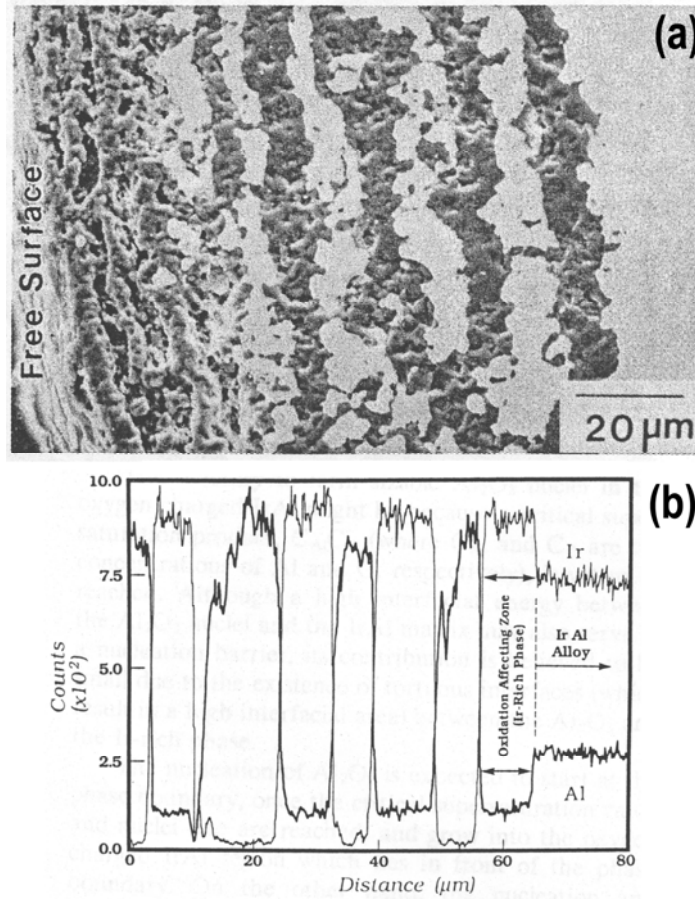


Fig. 3.10 Alternating layers of  $\text{Al}_2\text{O}_3$  and Ir, resulting from high temperature (1300 °C) oxidation of IrAl; (a) SEM micrograph, (b) EDS line scan. [Cho90].

### 3.3.2 High temperature oxidation of Ru [Jeh84]

Ru belongs to the platinum group metals, which are known as oxidation resistant metals. At RT the oxidation consists in the formation of a thin tarnish thin film on the surface. Above a “critical temperature” the thin film is no longer stable due to the high dissociation pressure of the oxides. The dissociation temperature for  $\text{RuO}_2$  in oxygen at atmospheric pressure is 1580 °C.

In the case of Ru oxidation, even if pressure and temperature conditions allow the formation of an oxide film, a loss of weight can still be observed because of the formation of gaseous Ru-oxides.

From the mass loss measurements performed during high temperature exposure, the volatilization rate of Ru could be plotted versus temperature (Fig. 3.11). The straight line indicates the weight loss due to the pure metal evaporation under high vacuum conditions. In fact at very high temperatures and low oxygen pressure the weight loss is mainly due to the metal evaporation.

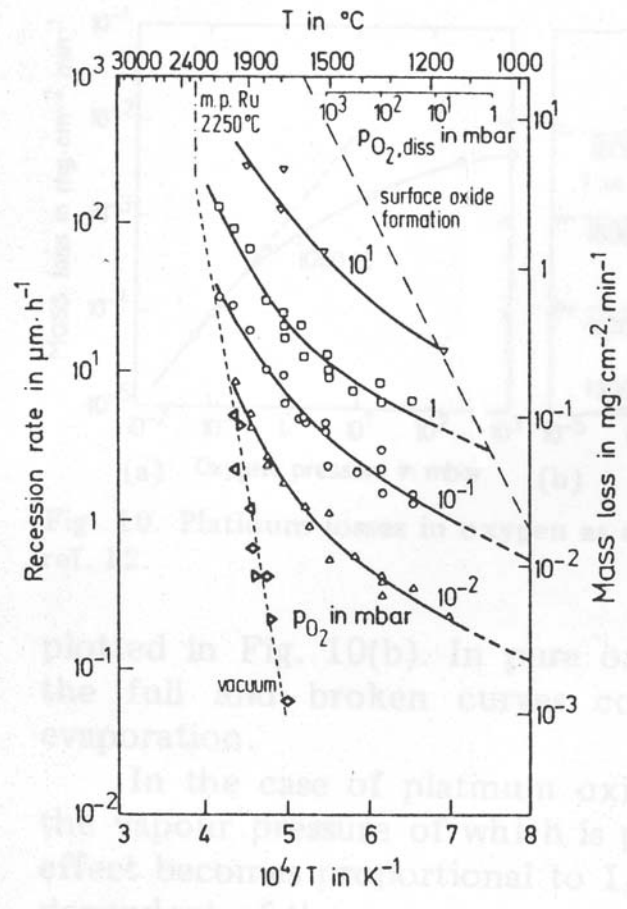


Fig. 3.11 Ruthenium weight losses as a function of oxygen pressure and temperature. [Jeh84].

It must be noticed, then, that the mass loss in oxygen compared to vacuum is higher by several orders of magnitude and is caused by the  $\text{RuO}_3$  and  $\text{RuO}_4$  evaporation. The Ru weight losses during high temperature oxidation are summarized in Fig. 3.12.

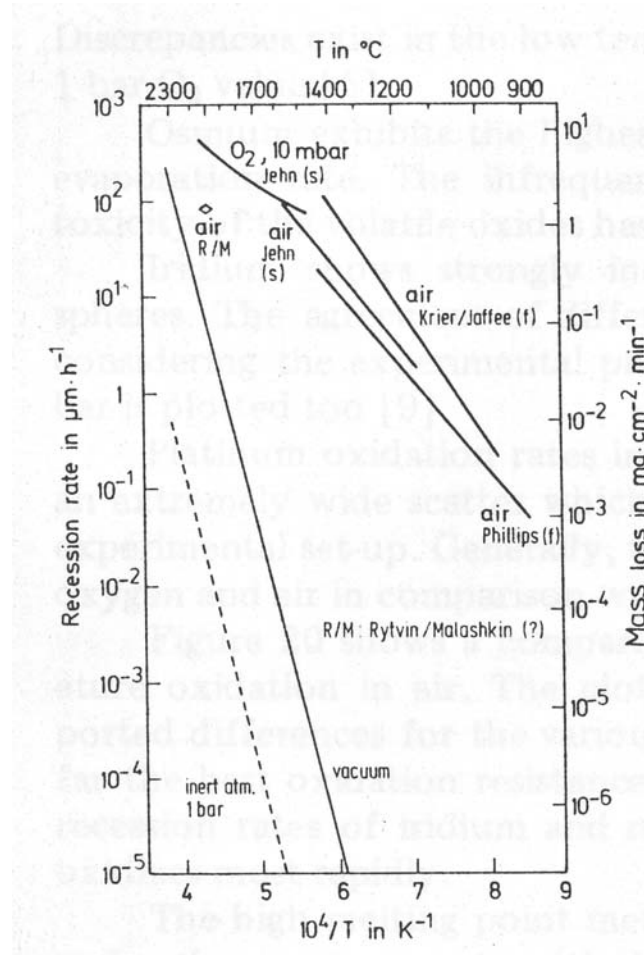


Fig. 3.12 Ruthenium weight losses during high temperature oxidation in air at atmospheric pressure. [Jeh84].

### 3.3.3 High temperature oxidation of RuAl alloy [Sol03, Fle93]

Fleischer and McKee [Fle93] have examined the mechanical and oxidation properties of a group of intermetallics based on the B2 (cP2) compound RuAl.

The oxidation tests were conducted in flowing oxygen at 1100  $^{\circ}\text{C}$ . After an initial parabolic gain of weight, many of the alloys are reported to lose weight, either through volatilization or spalling of the oxide.

The initial parabolic rate constants are summarized in Fig. 3.13.

More recently Soldara and co-authors have investigated the oxidation of a single phase RuAl oxidized at 1000 °C by SEM and XRD.

The results showed that a dense and protective  $\alpha$ -Al<sub>2</sub>O<sub>3</sub> scale and an Al depleted sub-layer have formed. The oxide morphology showed the formation of needles, which suggested an oxidation mechanism based on the Al outward diffusion.

Due to the outward diffusion of Al a concentration gradient profile is formed that enhances the nucleation and growth of a Ru-rich phase, similarly to the case of IrAl seen previously.

Differently to the NiAl case in which the formation of needles on the surface has been related to the transient  $\theta$ -Al<sub>2</sub>O<sub>3</sub>, the needles formed on RuAl have an  $\alpha$ -phase.

A parabolic rate constant has been evaluated by analyzing the oxide thickness after different oxidation times (ca 0.042  $\mu\text{m}^2/\text{h}$  which corresponds to  $2 \cdot 10^{-12} \text{ g}^2/\text{cm}^4\text{s}$ ). But the oxidation process appeared to obey to a parabolic behaviour only at the initial stages, showing a lower oxidation rate after 100 h.

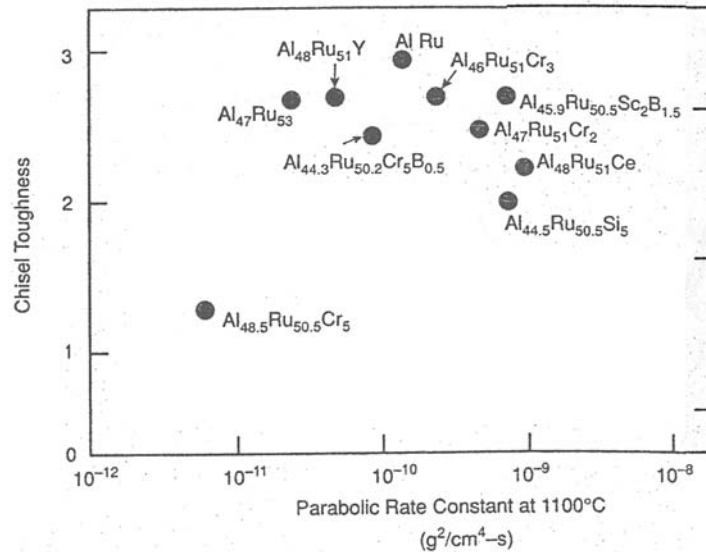


Fig. 3.13 Parabolic rate constants ( $k$ ) at 1100 °C for initial oxidation of various alloys vs the chisel toughness (CT). [Fle93].

## 4. EXPERIMENTAL METHODS AND SAMPLE PREPARATION

### 4.1 PROCESSING OF RuAl

RuAl alloy is a difficult material to prepare by melting processing, because (i) it has a high melting point, (ii) the volatility of aluminum in the molten bath is severe and (iii) RuAl alloy has a very narrow stoichiometric gap. During preparation Ru and Al powders are mixed together in the crucible, and the big difference of their melting points (660 °C for Al and 2300 °C for Ru) results in a higher volatility of Al. Thus, the depletion of Al concentration in the molten bath leads to the formation of second phases, which can be either inter- or intra-granular due to the dendritic solidification.

All the experiments performed in this study were conducted on near stoichiometric polycrystalline RuAl (B2 structure) obtained by *arc-melting* and *induction-melting*.

*The arc-melting technique* uses an electrical arc, which occurs in a gas-filled space between two conductive electrodes. This electrical arc develops very high temperatures, through which it is possible to melt and/or vaporize any material.

*Induction-melting* is a process that heats and melts metals by using the inducted electric current. The material, which has to be melted, is placed in a water-cooled crucible, and surrounded by a coil carrying a high variable current. After the induction-melting process, the samples have been isostatically hot pressed (HIP: 200 MPa, at 1600 °C, in Ar, for 8 h).

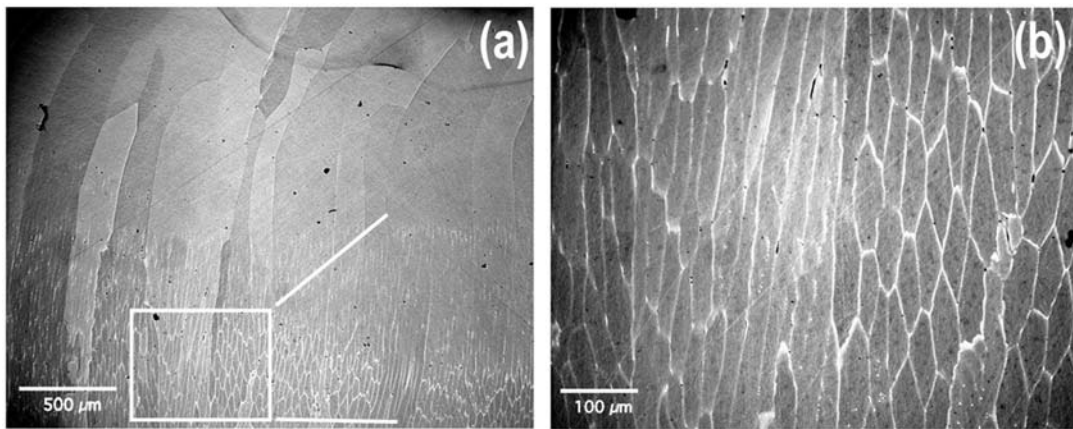


Fig. 4.1 Optical micrographs showing: (a) the polished surface of an arc-melted RuAl binary alloy; (b) detail of the infra and inter granular Ru segregation.

The arc-melted samples consisted of elongated grains (length: 0.5-3 mm, diameter: 50-500  $\mu\text{m}$ ) containing traces of a  $\delta$ -Ru second phase (Fig. 4.1): the RuAl elongated grains are caused by the fast cooling during casting and the Ru segregation originate from the dendritic solidification, as already described elsewhere [Fle91, Fle93, Wol97]. The induction melted samples also consisted of elongated grains but bigger compared to those of the arc-melted material (~5 mm in length and 0.2-1 mm in diameter).

The processing can be summarized as follows”

<p><b><u>Starting material:</u></b></p> <ul style="list-style-type: none"> <li>• Ru powder provided by Alfa AESER with a purity of 99.99%</li> <li>• Al with a purity of 99.999%, cut and polished</li> </ul>
<p><b><u>Processing by Arc-melting</u></b></p> <ul style="list-style-type: none"> <li>• Ru molten, pushed into Al (arc melting) strong exothermic reaction.</li> <li>• Prior processing: evacuation, <math>2 \cdot 10^{-5}</math> mbar.</li> <li>• Processing in 500mbar Ar 6.0.</li> <li>• 2 x Remelting.</li> </ul>
<p><b><u>Processing by Induction-melting</u></b></p> <ul style="list-style-type: none"> <li>• Prior processing: 2 times evacuation to <math>10^{-3}</math> mbar, filling in between with Ar 6.0 to 1100 mbar.</li> <li>• Processing in 1100 mbar Ar 6.0.</li> <li>• 2 x Remelting.</li> <li>• Hot Isostatic Press (HIP): 200 MPa, at 1600 °C, in Ar, for 8 h.</li> </ul>

## 4.2 THERMOGRAVIMETRIC ANALYSIS

The TGA is a useful technique that describes the kinetics of the oxidation in-situ by measuring the change of weight of the sample during oxidation at high temperature.

The used TGA instrumentation is shown schematically in Fig. 4.2. The sample hangs on a quartz wire, in a quartz tube, connected to a microbalance (Cahn D200 digital recording balance). The oxidizing atmosphere can be controlled using a flow controller at the gas inlet (MKS type 247D), allowing the operator to choose different compositions of the oxidizing gas or to conduct the experiment in air.

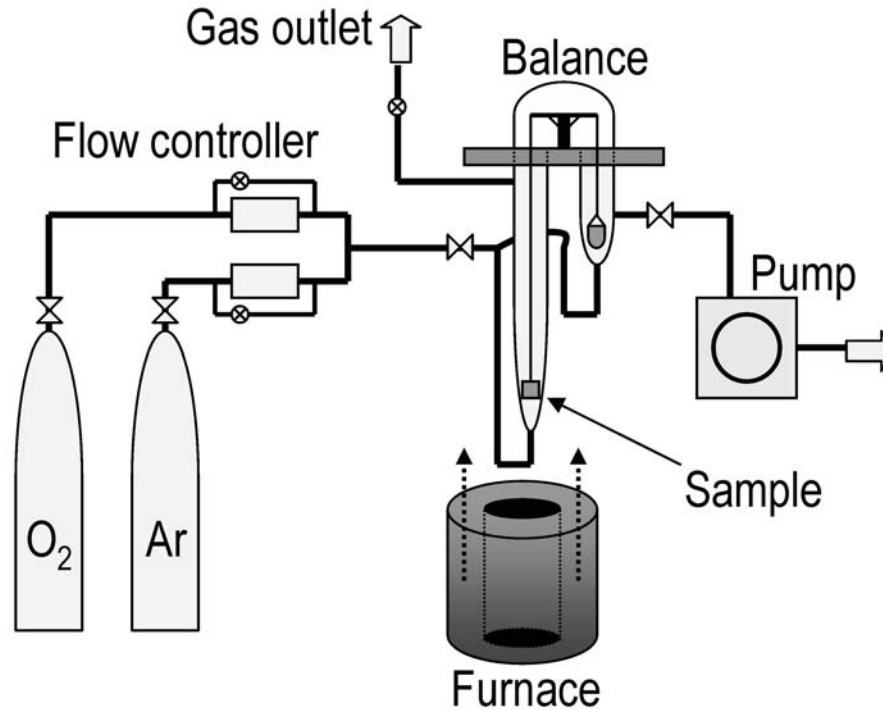


Fig. 4.2 Schematic drawing of the thermogravimetric equipment.

It must be noticed that this technique is sensible to errors due to the Archimedian buoyancy effect. To describe this effect let's consider a system formed by an object immersed in a fluid. This system can be described as the super-imposition of two sub-systems: (i) the object itself and (ii) the void in the fluid, which is occupied by the object. The resulting force, applied to the object immersed in the fluid, is the sum of the force applied to the object plus the force applied to the void in the fluid. The latter force has the same intensity, same direction and opposite versus of the force, which would have been applied to the fluid replaced by the void. This force is the Archimedian force.

Therefore, when the gas composition or the temperature is altered, the density of the atmosphere changes and consequently also the Archimedian force changes. This influences the weight measurement.

The weight variation is depending on the volume of the specimen, while the weight variation due to the oxide growth is proportional to the surface. Therefore, it is advisable to use large specimens with a large flat surface and a small volume/surface ratio, in order to minimize the influence of the buoyancy effect.

Recording continuously the weight variation of the specimen is possible to identify several features [Bir83], which cannot be observed with other methods, such as non-continuous weight measurement and the evaluation of the oxide thickness at different times. In fig. 4.3 these features are exaggerated for a better description.

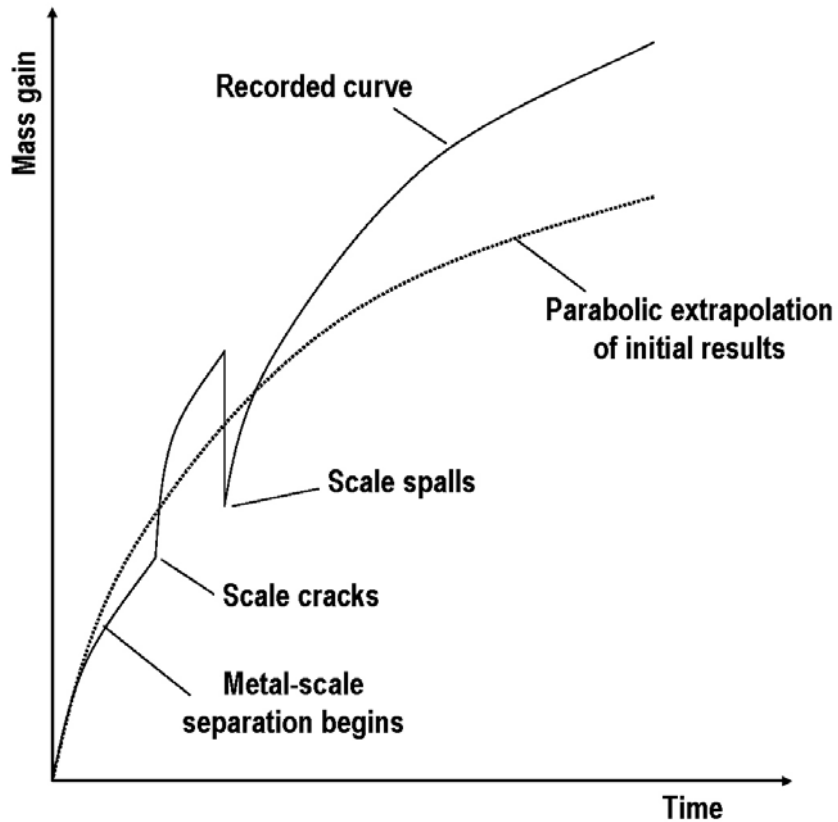


Fig. 4.3 Features detectable through TGA with a continuous monitoring. After decohesion of the oxide scale, oxygen has to diffuse through the vapour phase to reach the substrate, resulting in a slower kinetic. Cracks offer oxygen a free path to the substrate. Spalling of small areas of the oxide scale can be detected registering immediate weight loss followed by a faster kinetic due to the direct contact between the oxidizing atmosphere and the bare metal.



When there is a loss of contact between the oxide scale and the substrate, the oxygen has to diffuse through the vapour phase to reach the substrate, resulting in a slower kinetic.

When cracks form in the oxide scale, free paths are offered to oxygen to reach the substrate, resulting in a faster kinetic.

When portions of the oxide scale spall, an instantaneous loss of weight is recorded by the balance. This weight loss is then followed by a faster kinetic caused by the direct contact between the oxidizing atmosphere and the bare metal.

#### **Sample preparation for TGA**

- RuAl bulk material prepared by arc-melting or induction-melting.
- RuAl slices cut with a Struers Acutom-50: 10 x 10 x 1 mm.
- The surfaces were then prepared by polishing through 1  $\mu\text{m}$  diamond paste.

### **4.3 X-RAY DIFFRACTION (XRD)**

XRD methods were used to characterize the phases of the oxide while growing during oxidation and to evaluate the in-plane stresses of the  $\alpha\text{-Al}_2\text{O}_3$  and the  $\delta\text{-Ru}$  phases.

#### **Bragg law**

When a material is exposed to X-ray radiation, the radiation interacts with the atoms of the material.

If the atoms form a crystalline structure and the distances between the atoms are of the same magnitude as the wavelength of the X-rays, constructive and destructive interference will occur (diffraction).

Each set of planes in a crystalline structure has a specific interplanar distance and will give rise to a characteristic angle of diffracted X-rays. The relationship between wavelength, atomic spacing ( $d$ ) and angle was solved geometrically by Bragg (Fig. 4.4) as:

$$2d \sin \Theta = n\lambda \quad (4.1)$$

If the wavelength is known (depends on the type of X-ray source used) and the angle can be measured, then the interplanar distance can be calculated from the Bragg equation (4.1).

The interplanar distances of a crystalline structure are characteristic of the material and of the phase; therefore, comparing the acquired pattern to reference patterns, it is possible to determine the phases of the analyzed compound.

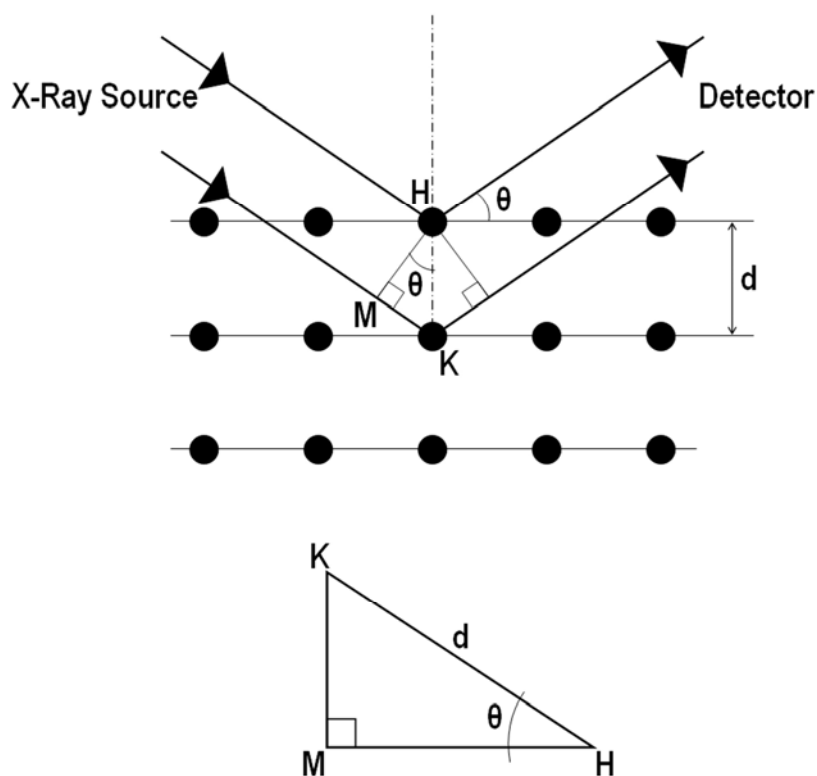


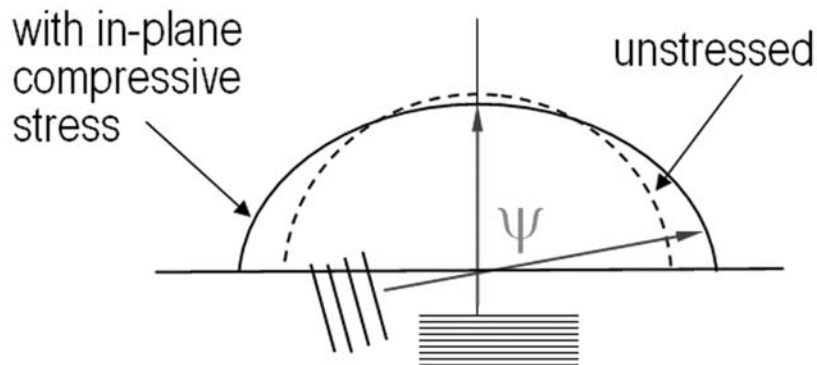
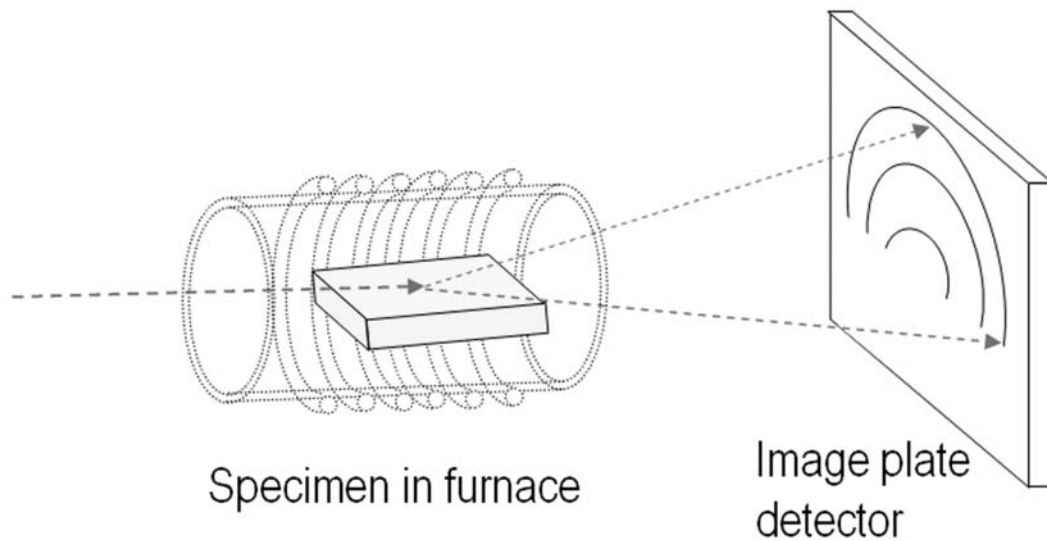
Fig. 4.4 Geometric explanation of Bragg law in two dimensions, by representing the atoms with black spots.

### **Distortion of the Debye-Scherrer rings**

In-situ measurements of the Debye-Scherrer diffraction patterns from the oxide scale are recorded during oxidation, and the elliptical distortion of the diffraction rings is analyzed to determine the in-plane strain [Hou04].

The measurements were performed using synchrotron radiation at beamline 12BM at the Advanced Photon Source at Argonne National Laboratory. A schematic drawing of the

experimental setup is shown in Fig. 4.5. The test specimen is placed on an alumina shelf mounted in a horizontal tube furnace. The X-ray beam has a spot size of about 0.2 mm and 21.6 keV of energy; it hits the sample at an incidence angle in the range of 2 to 5°. Half circles of Debye-Scherrer diffraction rings from the sample are recorded using an image plate detector.



Courtesy of Dr. B. Veal

Fig. 4.5 Schematic drawing of the experimental procedure for the in-situ stress analysis during oxidation at high temperature.

For precise determination of the X-ray scattering center, a porous, sintered alumina is used as reference. The reference is placed into the X-ray path, and a reference spectrum is acquired after five successive sample measurements. Each measurement takes 5 min.

The technique is a single exposure method, where diffraction rings, from all diffracting planes are simultaneously acquired in the accessible range of  $\psi$  (7 - 75°);  $\psi$  is the angle between the sample normal and the scattering vector. Since in-plane and out-of-plane d-spacings of diffracting planes in a stressed film are different, the resulting Debye-Scherrer rings are elliptically distorted.

It is assumed that the layers are isotropic with no shear and are under a biaxial stress.

The in-plane and out-of-plane d-spacings ( $d_{in}$  and  $d_{out}$ ) for a given (hkl) line have been measured and the ratio

$$D = \frac{d_{in} - d_{out}}{d_{out}} \quad (4.2)$$

has been calculated. The in-plane strain for a homogeneous biaxially stressed polycrystal film is

$$\varepsilon_{11} = \frac{D(1-\nu)}{(1+\nu)} \quad (4.3)$$

where  $\nu$  is the Poisson's ratio, and the stress is

$$\sigma = E \frac{\varepsilon_{11}}{(1-\nu)} \quad (4.4)$$

where  $E$  is the Young's modulus.

#### 4.4 ELECTRON MICROSCOPY TECHNIQUES

After de Broglie's ideas of the wave-particle duality, it has been possible to relate the particle momentum  $p$  to its wavelength  $\lambda$  through Planck's constant:

$$\lambda = \frac{h}{p} \quad (4.5).$$

In electron microscopes, a momentum is imparted to the electron by accelerating it through a potential drop,  $V$ , giving it a kinetic energy,  $eV$ . The relation between accelerating voltage and the wavelength of the electron is given by:

$$\lambda = \frac{h}{(2m_0eV)^{1/2}} \quad (4.6)$$

where  $m_0$  stands for the electron mass.

Electron microscopes were developed in order to achieve a better resolution than the optical microscopes. In fact the resolution of light microscopes is limited by the wavelength of visible light, which is not sufficient to describe materials at atomic scale (the resolution of a good light microscope is about 300 nm).

In the case of electron microscopes, the resolution is limited no more by the wavelength of the beam, which can be in the order of picometers, but by the efficiency of the magnetic lens (the spatial resolution of the last generation TEMs is approaching 1 Å).

When an electron beam interacts with matter, the incident electrons can scatter elastically or inelastically. The elastic scattering consists in a deflection of the incident electron trajectory, in which the kinetic energy of the electron is conserved. The deflection results from Coulomb interactions between the incident electron and the atoms in the sample.

The electronic beam scatters inelastically, when a part of the kinetic energy of the incident electrons is absorbed by the matter. There are many interaction processes, which result in an energy loss of the primary electron. This energy is transferred to the specimen in different ways, for example: phonon scattering, plasmon scattering and inner shell excitation.

Scanning electron microscopes are used for surface investigations, while transmission electron microscopes are used for bulk investigations.

#### 4.4.1 Scanning Electron Microscopy (SEM)

The SEM used for the investigations was a field emission SEM (JEOL 6300F), which is equipped with a Schottky emitter. The emitted electrons are accelerated by an electric potential in the range of 1-40 kV. The beam is then focused by the objective lens onto the surface and scanned across the surface using scanning coils (Fig. 4.6).

When the electron beam hits the sample surface, secondary and backscattered electrons form. The secondary electrons are emitted because the primary electrons transfer part of their energy to the electrons of the sample through inelastic scattering. These electrons are characterized by energies typically in the range of 10 to 50 eV.

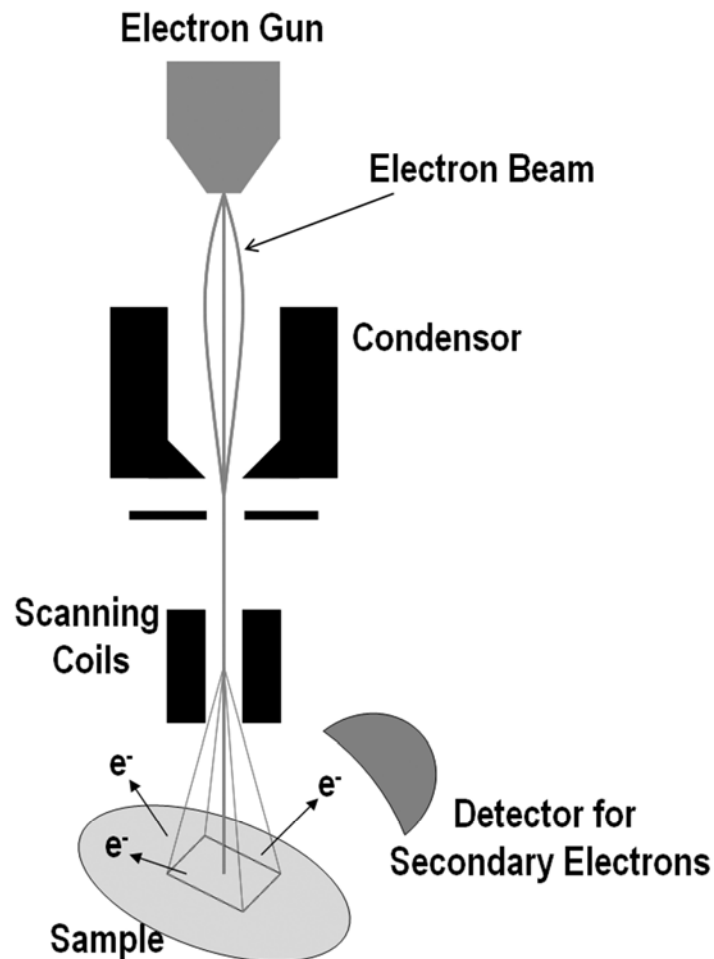


Fig. 4.6 Schematic drawing of a scanning electron microscope (SEM) [But03].

Secondary electron imaging gives information about the topography of the sample's surface because the low kinetic energy that characterizes these electrons restricts their free path in the sample. In general the information collected refers to the first 1-2 nm close to the surface.

The backscattered electrons, instead, are formed due to elastic scattering of the primary electrons with the sample.

Backscattered imaging gives good compositional contrast but is less surface sensitive. In fact the average energy of the backscattered electrons is less than the primary incident beam but of the same order of magnitude; therefore the higher kinetic energy increases the main free path of the backscattered electrons compared to the secondary electrons. In general the information collected refers to the first 100 nm close to the surface.

More detailed information is given in [Sch94, Bra99].

### **Auger Electron Spectroscopy (AES)**

The Auger investigations were performed with a JEOL JAMP-7810 Auger Electron Spectrometer. In AES the sample is irradiated with an electron beam, in which the electrons are typically accelerated by an electric potential in the range of 1-5 keV. The information acquired refers to the first 3-5 nm close to the surface.

The incident electron ejects an electron from the inner electron shells of the atoms of the sample, and an empty state is created. An electron in a higher shell then fills the empty state and energy is released, either as a characteristic X-ray photon or a secondary electron. The secondary electron, which is ejected from a higher shell, is called an Auger electron (Fig. 4.7), and its kinetic energy is dependent only on the energies of the electron levels involved. Since the electron energy levels in the matter are discrete, peaks are visible in the energy distribution of the emitted electrons, which are characteristic of the elements present at the surface of the sample.

Usually Auger data are presented as a differentiated signal to enhance the visibility of the peaks.

More detailed information about Electron Spectroscopy is given in [Sea88].

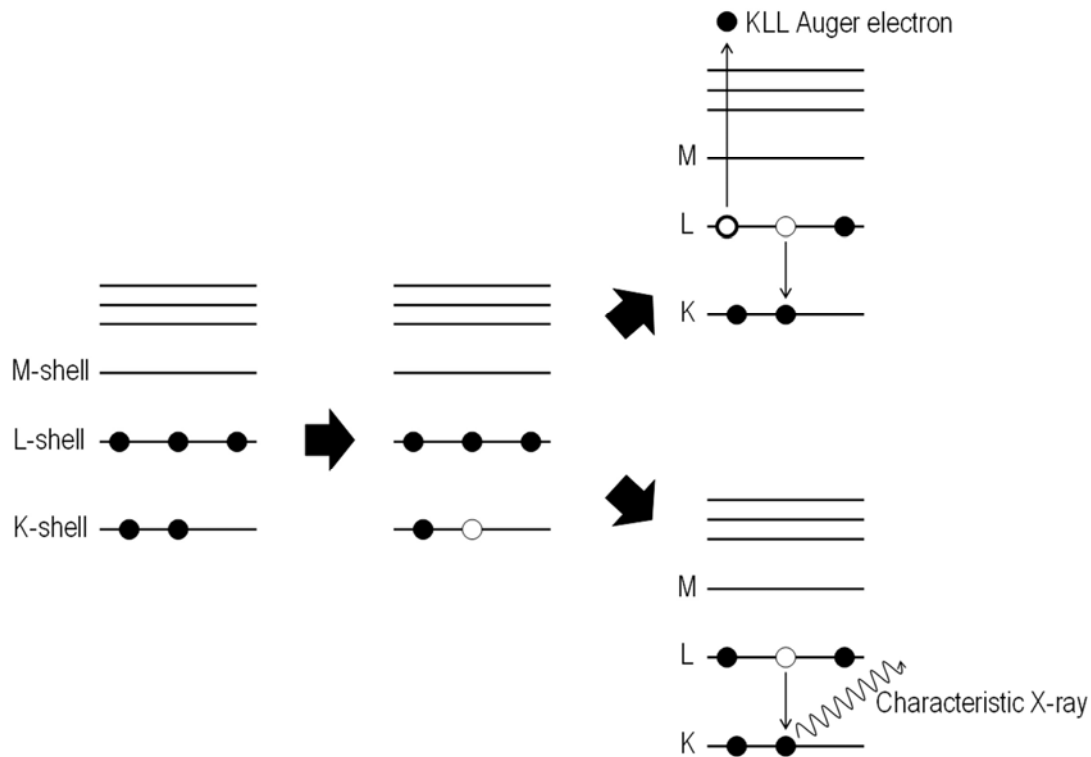


Fig. 4.7 Process of Auger electron transition.

#### 4.4.2 Transmission Electron Microscopy (TEM)

There are two possible ways to operate a TEM. The two operation modes are (i) for imaging and (ii) for diffraction. A schematic drawing of the ray diagram is shown in Fig. 4.8: In the imaging mode, an image is projected on the viewing screen, while in the diffraction mode the intensity of the intermediate lens are changed, allowing a diffraction pattern to be observed in the viewing screen.

The electronic beam scatters with the matter propagating across the specimen. The scattering varies on the atomic number, the thickness of the specimen and the crystal orientation, resulting in different contrast.

When the matter is organized in a crystalline structure, the diffraction pattern shows ordered diffraction spots in the viewing screen. These spots form due to the constructive interference between the diffracted beams, and obey the Bragg condition, mentioned previously (eq. 4.1).



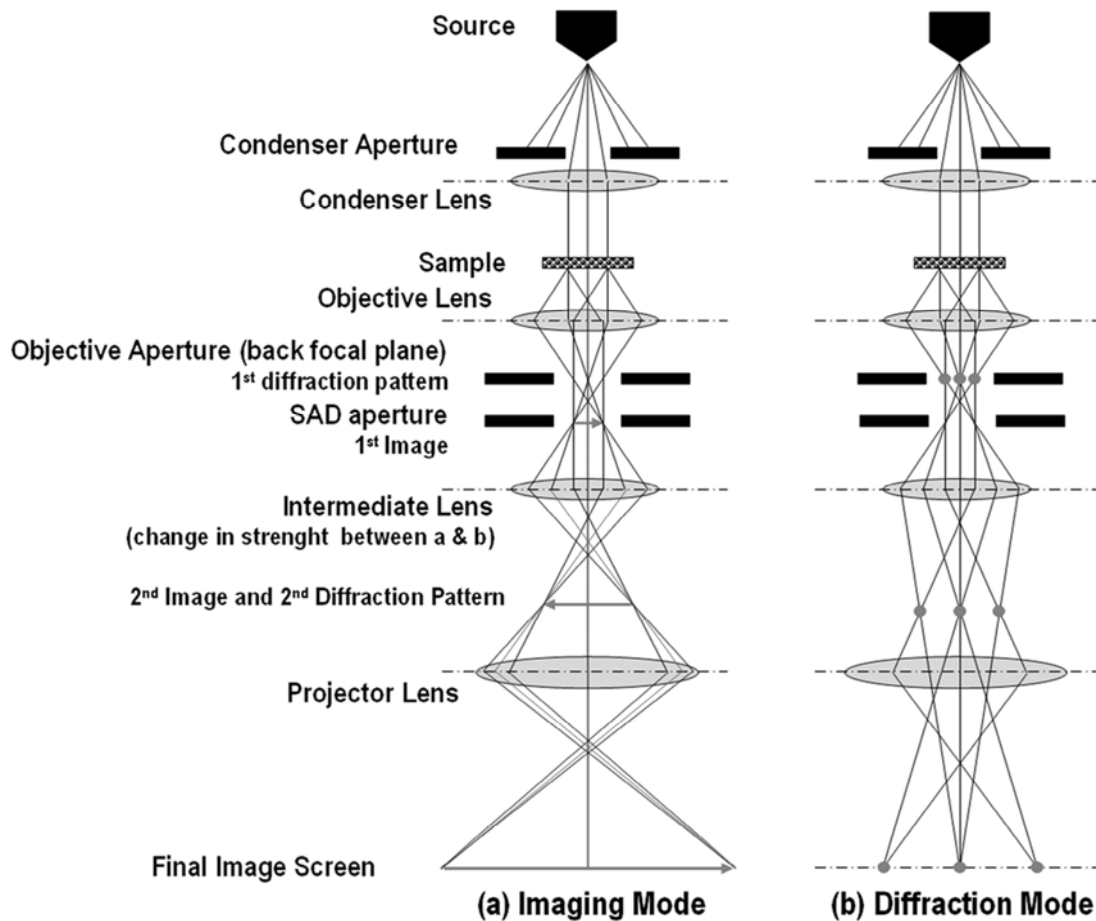


Fig. 4.8 Ray diagram for a conventional TEM, (a) in imaging mode and (b) in diffraction mode. [Wil96].

By inserting an aperture (Objective aperture) in the back focal plane of the objective lens, it is possible to select which diffracted beams will form the image. Bright field (BF) imaging is formed when only the direct beam is selected; while dark field (DF) imaging is formed when only one of the diffracted beams is selected. When a perfect crystal is investigated, the contrast in BF and DF images raises from thickness and crystal orientation.

To obtain the diffraction pattern from a selected area of the specimen, selected area diffraction (SAD), an aperture (Selective Area aperture) must be inserted in the imaging plane of the objective lens. This is the plane where the first intermediate image is formed.

In this case, only the beams selected by the SAD aperture contribute to the final diffraction pattern, which is observed onto the viewing screen.

More detailed information about Electron Spectroscopy is given in [Wil96, DeG03].

The TEM investigations were performed with a JEOL JEM-2000FX, a JEOL JEM-4000FX, a JEOL ARM-1250 and a dedicated scanning transmission microscope (STEM) VG-501.

### **Analytical TEM**

As mentioned previously, the electronic beam scatters inelastically, when a part of the kinetic energy of the incident electrons is absorbed by the matter. The amount of energy absorbed during the inelastic scattering depends on the nature of the element; therefore these interactions can be used to obtain chemical composition information. In particular, there are two techniques in TEM which are used for chemical analysis: (i) X-ray electron dispersive spectroscopy (XEDS or EDS) and (ii) electron energy loss spectroscopy (EELS).

(i) X-rays are generated from the interaction between the incident electron beam and the atoms of the sample. This interaction takes place when an incident electron penetrates through the outer electron shell of the atom and interacts with inner-shell (or core) electrons. If the energy, which has been absorbed by the inner-shell, is sufficient to eject one electron, then the atom will be left in an excited state (ionized atom). The atom will return to its lowest energy state by filling the missing electron with one electron from the outer-shell. This loss of energy is accomplished by the emission of an X-ray or an Auger electron (Fig. 4.7). Due to the discrete energy levels of the matter, the energy of the emitted X-rays characterizes the different elements.

The probability of X-ray versus Auger emission is described by the fluorescence yield,  $w$ , which is the ratio of X-ray emissions to inner shell ionizations. The fluorescence yield is strongly depending on the atomic number (Fig. 4.9); one approximate expression for  $w$  is:

$$w = \frac{Z^4}{a + Z^4} \quad (4.6)$$

where  $a \sim 10^6$  for the K shell.

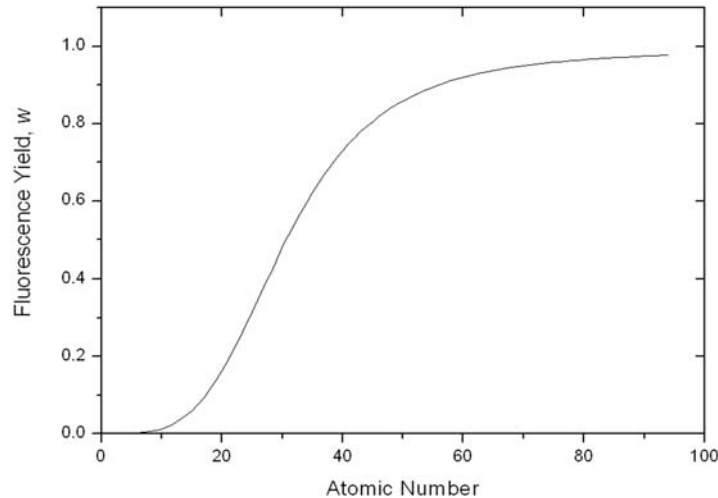


Fig. 4.9 Fluorescence yield,  $w$ , versus Atomic number.

(ii) EELS. The intensities of the electrons, which underwent an energy loss, are represented in an “energy-loss” spectrum. This can be divided in three regions: (i) the zero-loss peak, which consists primarily of elastic forward-scattered electrons; (ii) the low-loss region (up to  $\sim 50$  eV), which refers to electrons that have interacted with the outer-shell electrons of the atoms in the specimen; and (iii) the high loss region, which refers to electrons that have interacted with the inner-shell (or core) electrons.

The low-loss energy region contains information about the electronic properties of the specimen, while the high-loss region contains information characteristic of the atoms, which belong to the sample.

The processes of inner-shell ionization (EELS and EDS) are different aspects of the same phenomenon. The advantage of EELS is that the scattering in this case is not influenced by the fluorescence yield limitation that restricts light elements X-ray analysis.

Since the analyzed atoms are not isolated but integrated in a crystal lattice or amorphous structure, the spectra becomes more complex (Fig. 4.10). The ionization edges are superimposed on a decreasing background formed by plural inelastic scattering events. This background may also show some fine features, which are formed due to the bonding

with the surrounding atoms. These fine structures are defined as energy loss near edge structure (ELNES). More than  $\sim 50$  eV after the edge, small oscillations may be detectable due to diffraction effects, which are called extended energy loss fine structure (EXELFS).

More detailed information about Electron Spectroscopy is given in [Wil96, Goo01].

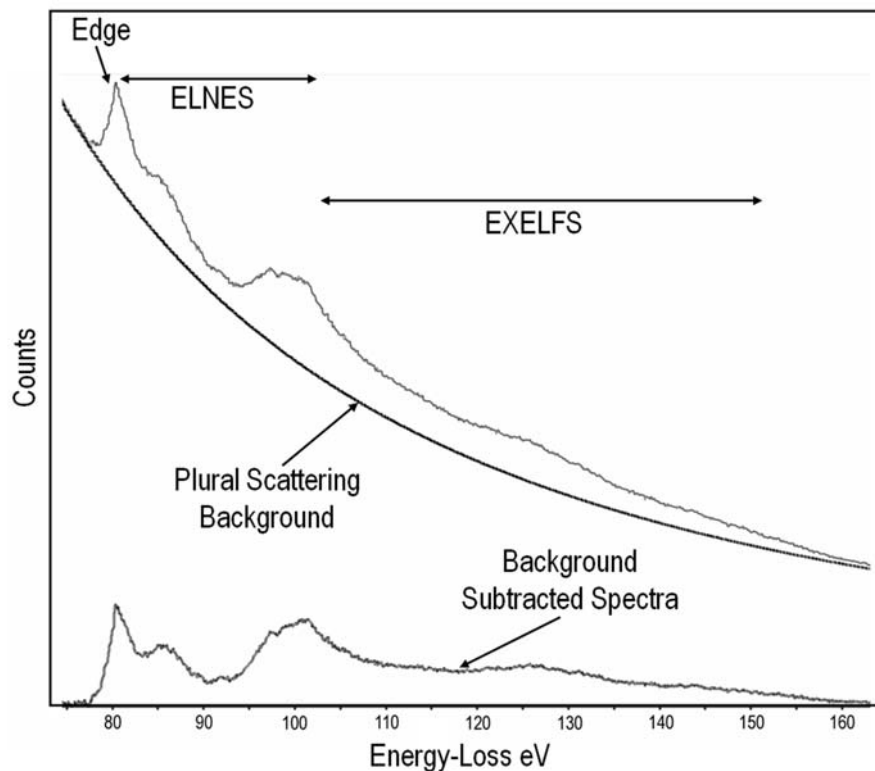


Fig. 4.10 Electron energy loss spectra (EELS) from an Al<sub>2</sub>O<sub>3</sub> specimen. The characteristic features are highlighted: (i) the edge, (ii) the energy loss near edge structure (ELNES), and (iii) the extended energy loss fine structure (EXELFS).

### **High-angle Annular Dark Field (HAADF) Imaging**

A TEM equipped with a scanning unit is required for acquiring HAADF images. The images are formed, in fact, by scanning the electron beam across the specimen while simultaneously the HAADF signal is registered at each point.

The HAADF detector collects mainly the electrons that are scattered incoherently at relatively high angles, from 75 to 150 mrad, (Fig. 4.11); a small noise is given by thermal diffused scattering.

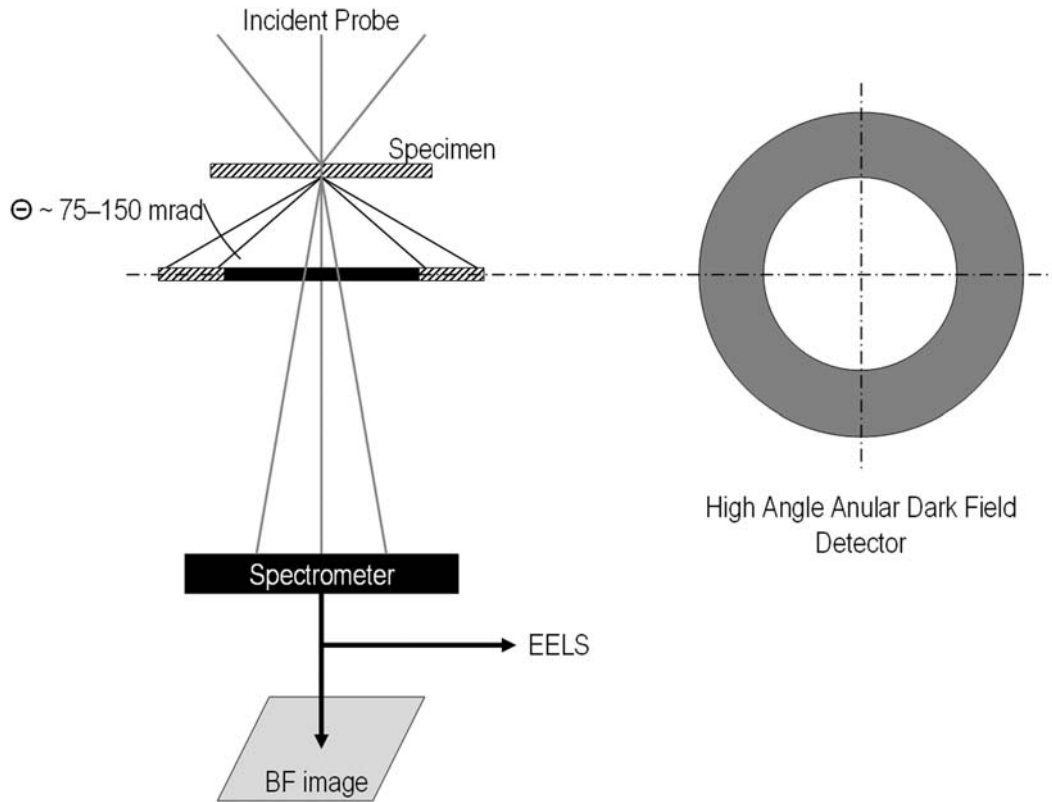


Fig. 4.11 Schematic drawing of the STEM-HAADF imaging system.

HAADF imaging can be explained by Rutherford scattering, as a scattering from the unscreened nucleus of the atoms in the sample:

$$\frac{d\sigma}{d\Omega} = \frac{Z^2 e^4}{16E^2 \sin^4 \Theta} \quad (4.7)$$

where  $\sigma$  is the scattering cross-section,  $Z$  the atomic number,  $e$  the elementary charge,  $\Theta$  the scattering angle and  $E$  the energy of the scattered electron.

The intensity of the image is proportional to the square of the atomic number,  $\sigma \propto Z^2$  (see equation 4.7); this technique is, indeed, called *Z-contrast*.

More detailed information about Electron Spectroscopy is given in [Wil96].

### **High-resolution TEM (HRTEM)**

HRTEM imaging shows a magnified image of the specimen in projection up to finest details, such as atomic columns. The formation of the image is in accordance with Abbe's theory [Bor99], which states that at least one diffracted beam and the direct beam have to be used to create the image; in order to resolve the atomic columns, also large values of the  $\mathbf{k}$  vector (reciprocal space) have to contribute to the image formation.

The HRTEM image can be described as a complex interference pattern of the diffracted beams and the direct beam, which depends on the imaging conditions and the thickness of the specimen. A schematic drawing of the image formation is shown in Fig. 4.12.

There are two main interactions that contribute to the creation of the image, (i) the interaction of the incident plane wave with the electrostatic crystal potential of the specimen and (ii) the interaction between the exit wave function and the microscope lens system. The first one is susceptible to multiple electron scattering, which increases with thickness, while the second is influenced by electric current instabilities and aberrations of the lens.

The aberrations of the lens lead to the projection of disks rather than spots in the image plane. Due to the overlap of the disks, the direct correlation between an image point and an object point is lost. As a consequence of the image formation mechanism a direct interpretation of the image will not allow an accurate investigation, and the use of computer simulations is, therefore, required in order to deeply analyze the sample's structure.

In this work, the HRTEM has been used specifically to distinguish in-situ, crystalline from amorphous structures in nanometric features depending on the temperature (see par. 5.1). Therefore the use of computer simulation was not required; more detailed information about HRTEM can be found in [Wil96].

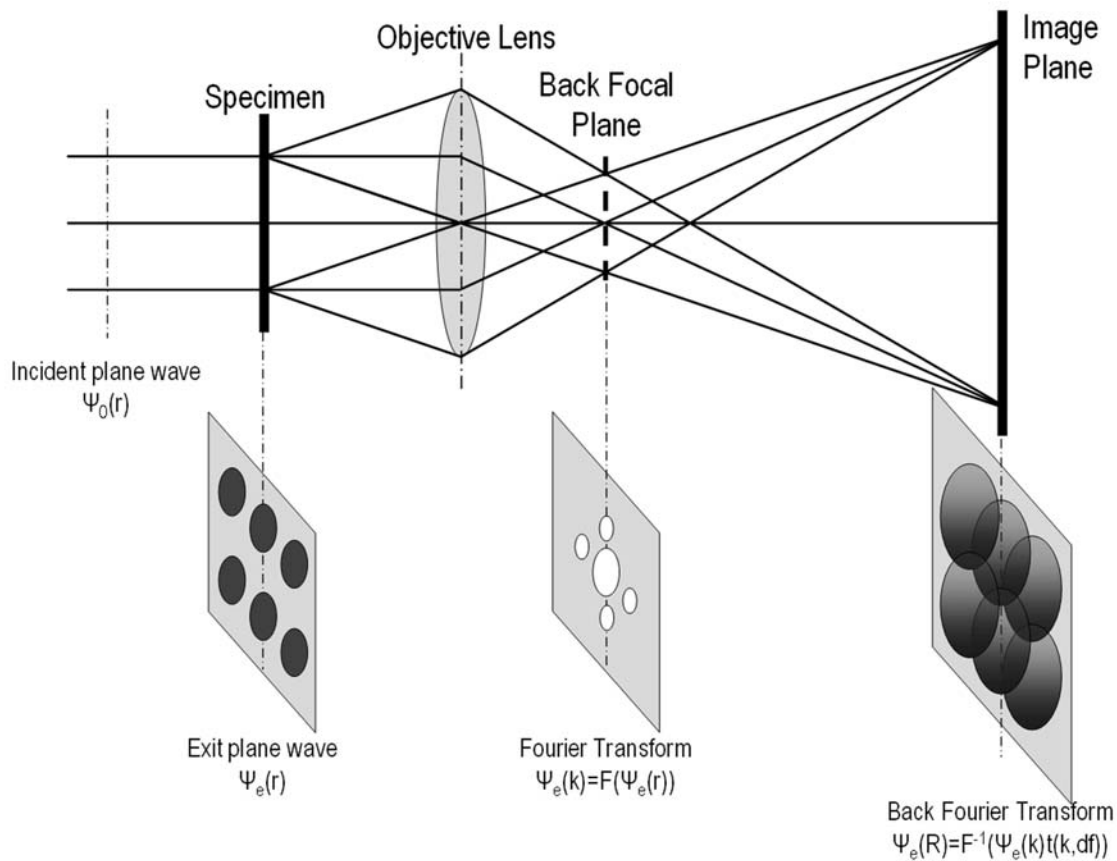


Fig. 4.12 Image formation in HRTEM;  $t(k, df)$  is the Contrast Transfer Function (CTF), which describes the transmitted frequencies  $\mathbf{k}$ .

### **Sample preparation for TEM investigations**

Specimens for TEM investigations must be mechanically stable and electron transparent; therefore, the specimen thickness typically is lying in the range of 5 to 100 nm.

Several techniques are used in order to prepare such specimens, such as mechanical grinding, chemical etching, electrolytic thinning, ion-beam cutting techniques and ion-thinning techniques.

The preparation of cross section samples of metal/ceramic interfaces, as it is the case for  $\text{Al}_2\text{O}_3$ /metal substrate interfaces, which form after oxidation at high-temperature, proved to be a challenging task. In fact the metal and the ceramics possess different properties

(conductivity, hardness, plasticity), which lead to different behaviours of the materials during the preparation (mechanical or ion treatment).

For the preparation of the cross section specimens, preparation techniques based on methods developed by Strecker et al. [Str93] were employed (Fig. 4.13):

### **Sample preparation for TEM**

- Oxidized samples are cut in stripes 2 mm large and ground from the backside to 180  $\mu\text{m}$  thickness.
- The stripes are inserted in alumina holders (3 mm diameter) and glued with G1 Gatan glue.
- Then the tubular alumina holder is cut in 500  $\mu\text{m}$  thick discs.
- The discs are polished until  $\sim 100$   $\mu\text{m}$  thickness.
- The specimen is then dimpled until 20 to 30  $\mu\text{m}$  thickness.
- One-sided ion-thinning (from the backside of the oxide) is performed until the formation of a hole.

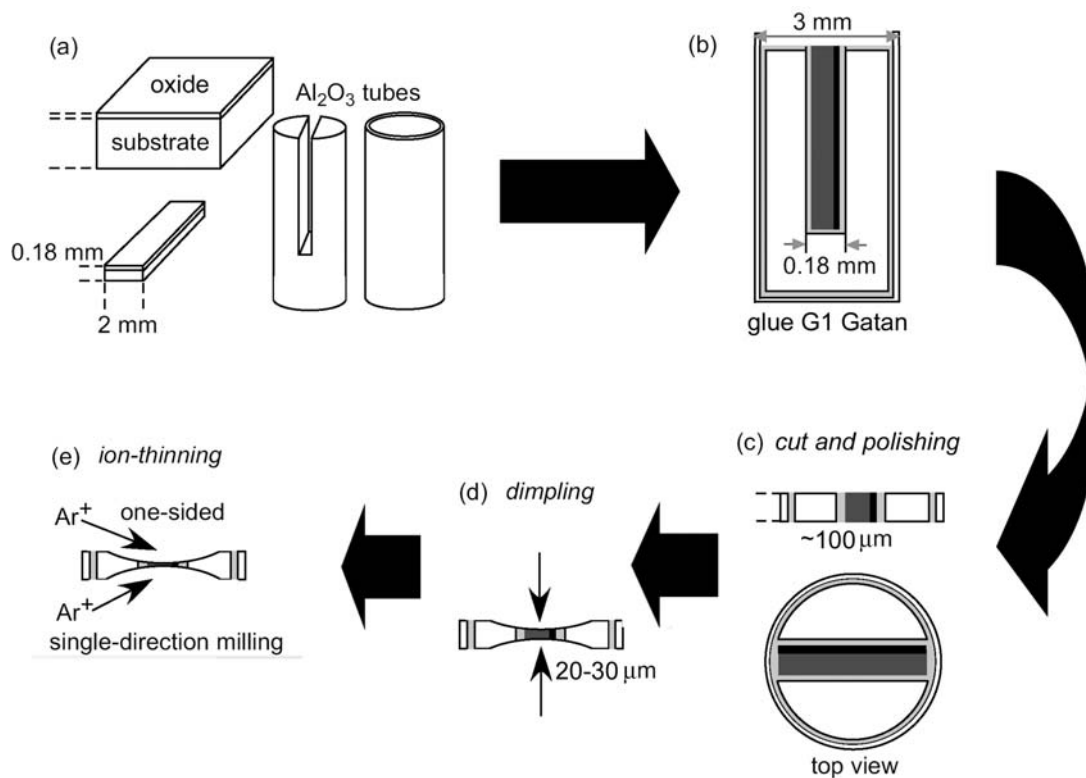


Fig. 4.13 Schematic drawing of the preparation of a TEM cross-section specimen.



## 5. RESULTS AND INTERPRETATION

### 5.1 MORPHOLOGICAL INVESTIGATION OF RuAl OXIDIZED IN AIR

#### Oxidation of RuAl samples with ground surface (600 SiC) at 1100 °C in static air

The samples used in this study were all prepared by arc-melting technique. As already mentioned in par. 4.1, this method leads to the formation of intra and inter-granular second phases rich in Ru (Fig. 4.1). The choice of using 600SiC paper for grinding the samples prior to oxidation was motivated by the wish of getting closer to the real working conditions.

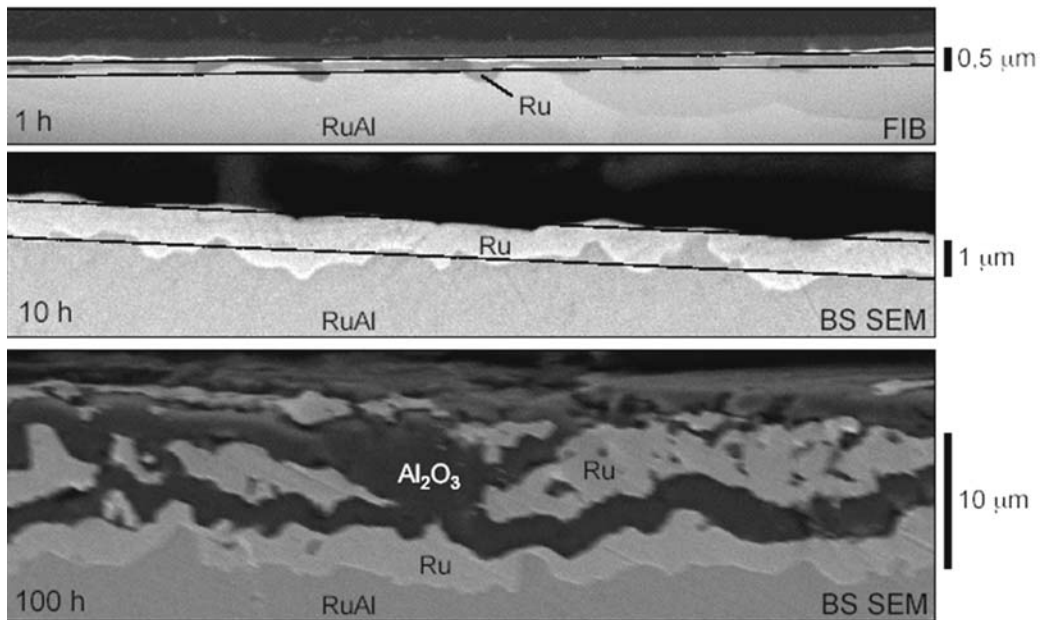


Fig. 5.1 SE-SEM picture of polished cross sections, showing a ground RuAl sample oxidized for (a) 1 h., (b) 10 h (oxide spalled during preparation), (c) 100 h.

The three samples used for this experiment were oxidized in a furnace (in air, no ventilation) already in temperature at 1100 °C for 1, 10 and 100 hours. The experiment showed that two layers form during oxidation: a  $\delta$ -Ru layer next to the substrate and a  $\alpha$ -

Al<sub>2</sub>O<sub>3</sub> layer on top of this layer. During long-time oxidation (100h), several couples of alternating Ru – Al<sub>2</sub>O<sub>3</sub> layers could be observed (Fig. 5.1).

The oxidation had also as a result the spallation of the  $\alpha$ -Al<sub>2</sub>O<sub>3</sub> layer (TGO) as can be clearly seen in fig. 5.2. The scratches present on this sample are from grinding and they seem to be one of the reasons for TGO spallation. Also, the bare metal suggests that the spalling occurred during cooling, due to the difference in thermal expansion coefficient between the oxide and the metal.

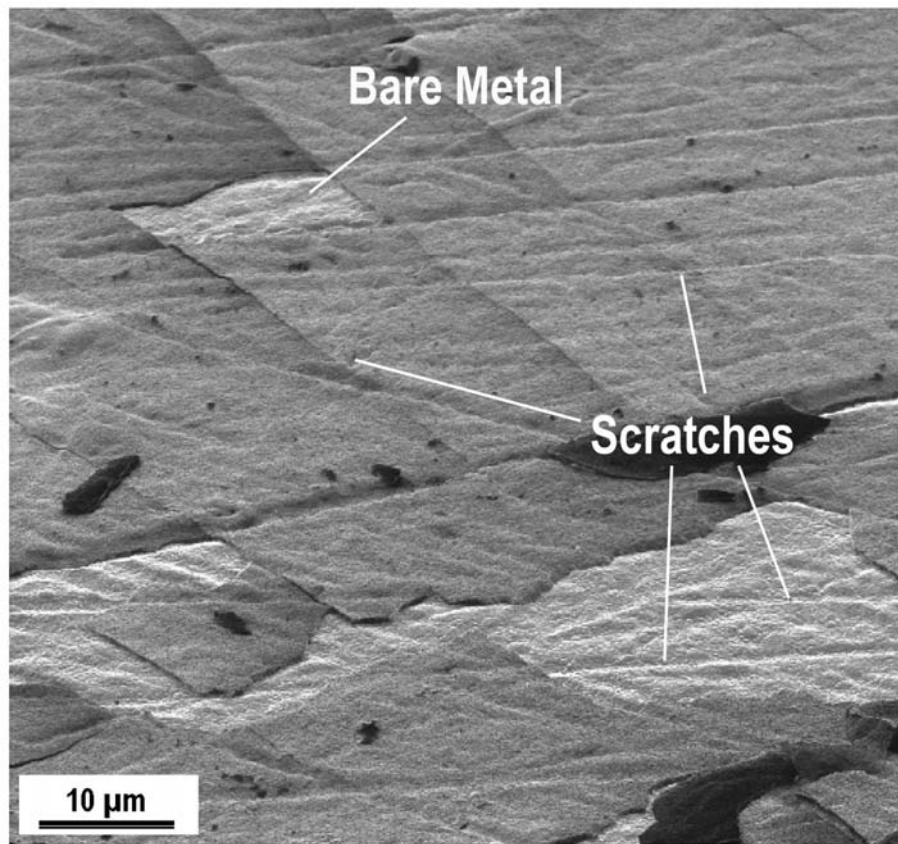


Fig. 5.2 FIB planview picture, showing a 600 SiC ground sample oxidized for 1 h. The imprints of the grinding favor the cracking of the oxide scale.

### **Oxidation of RuAl samples with polished surface at 1100 °C in static air**

The formation of the  $\delta$ -Ru layer, due to the Al depletion of the substrate, is considered the fundamental aspect of the oxidation behaviour of RuAl. Short oxidation times have

been of particular interest in order to understand when the Ru phase nucleates. Long oxidation times, instead, should indicate how the multilayer morphology, previously observed, evolves in time.

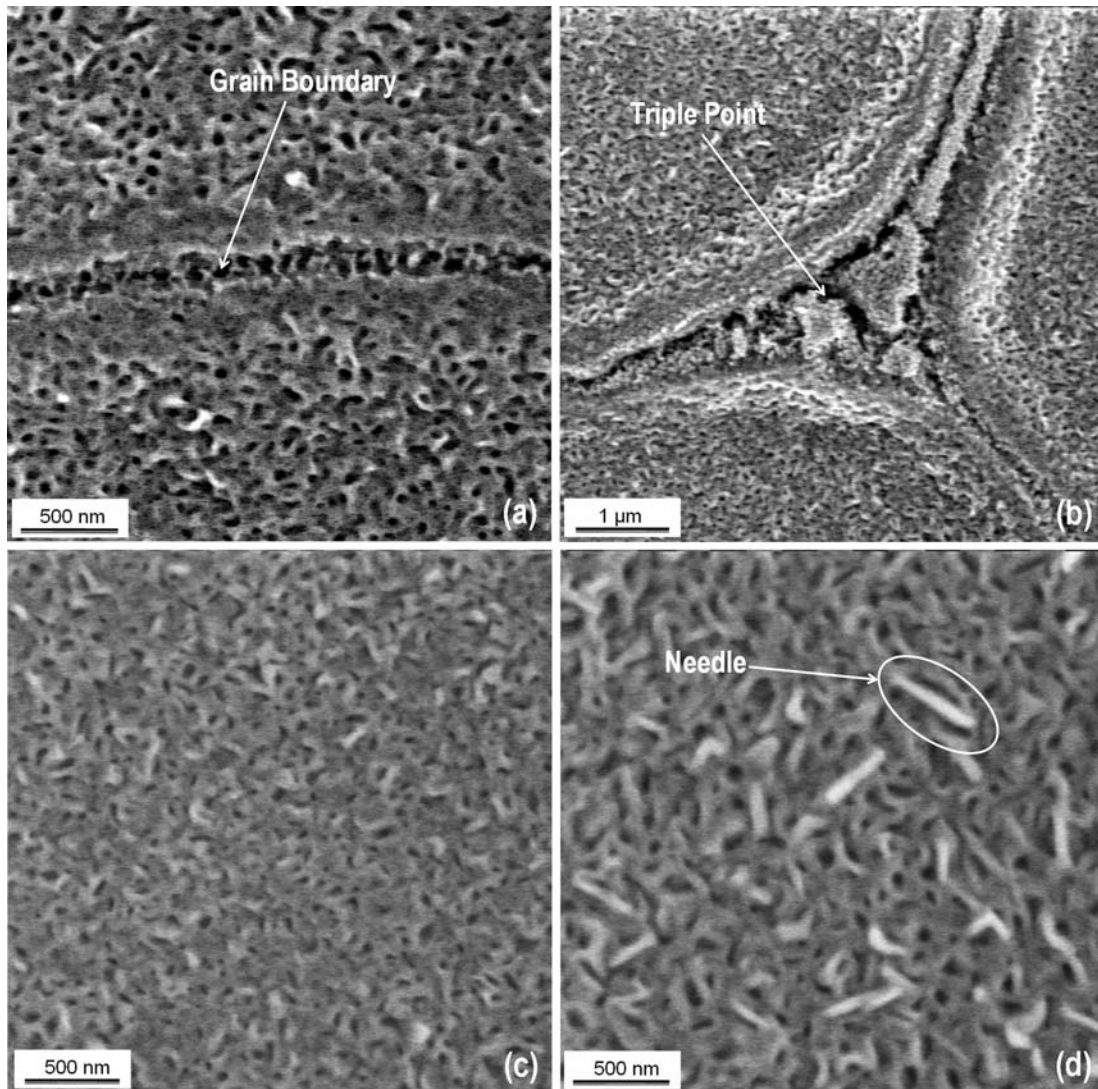


Fig. 5.3 SE-SEM plan view pictures of different features observed after oxidation at 1100°C. (a) The porosities forming at the grain boundaries after 0.1 h. (b) The porosities are more evident on triple points, always after 0.1 h. In fig. (c) and (d) a comparison between 0.1 and 1 h. oxidation shows that the roughness does not change considerably and that nucleating needles can be detected after 1 h.

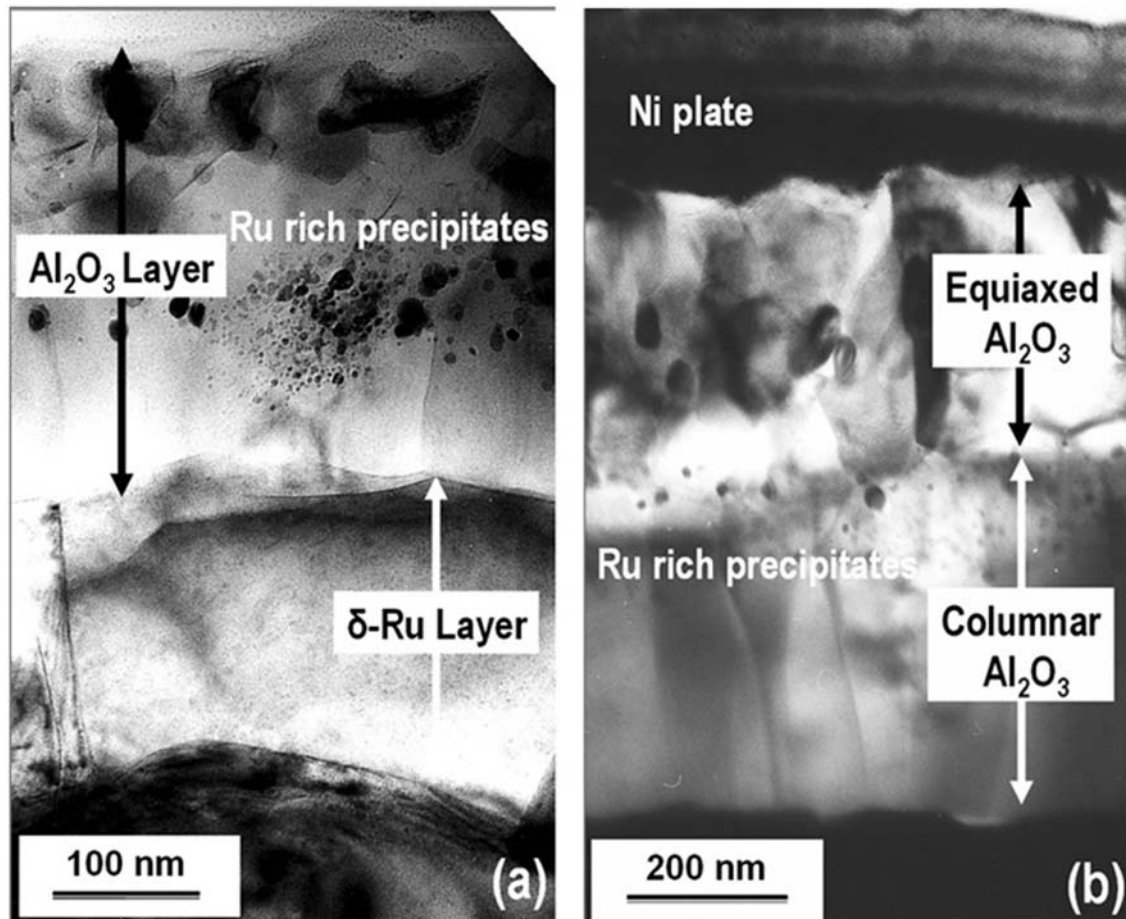


Fig. 5.4 Bright field (BF) cross section TEM pictures of the oxide formed after oxidation in air at 1100°C for: (a) 0.1 h; (b) 1 h. (JEOL JEM 4000 FX)

Three arc-melted RuAl specimens have been mirror-like polished with a 1 μm diamond paste and then inserted in the furnace (air, no ventilation) already in temperature for 0.1, 1 and 500 h. The polishing treatment of the surface has been chosen in order to simplify the oxidation mechanism by avoiding non planar stresses and diffusion dis-homogeneities induced by grindings scratches.

Plan-view images after short oxidation times (0.1 and 1 h) offer the possibility to observe the result of the evaporation of Ru. In fact porosities can be seen at grain boundaries and triple points of the specimen, which are sites usually enriched with Ru (Fig. 5.3a, b). In

general, after a short oxidation time (0.1 h) the oxide shows a nano-roughness that remains constant up to 1 hour oxidation, when the only evident difference consists in the starting of needles nucleation (Fig. 5.3 c, d).

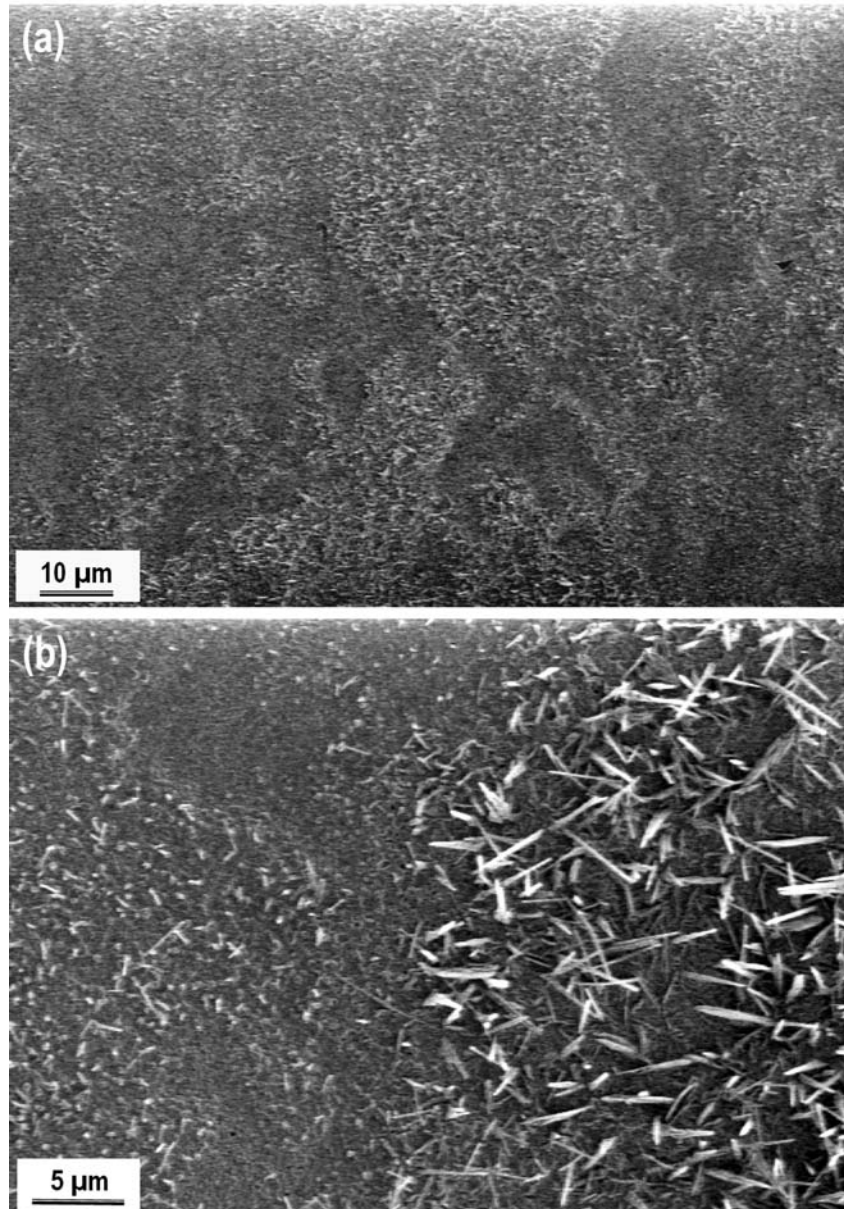


Fig. 5.5 SE-SEM plan view picture, showing a polished sample oxidized for 500 h. Alumina needles are observed, covering the majority of the surface.

TEM cross-section investigations were used to provide accurate information on the microstructure and chemistry of the system. After 0.1 h oxidation,  $\alpha$ -Al<sub>2</sub>O<sub>3</sub> and  $\delta$ -Ru layers have an average thickness of about 300 and 180 nm respectively, and nucleated columnar grains are already visible in the oxide layer (Fig. 5.4a). After 1 h oxidation the equiaxed and columnar zones can clearly be distinguished and the columnar grains show a thickness of about 300nm with a diameter similar to the 0.1 h ones (Fig. 5.4b). Furthermore Ru-rich particles, analyzed by energy dispersive spectroscopy (EDS), are observed at the boundary between the equiaxed and columnar  $\alpha$ -Al<sub>2</sub>O<sub>3</sub> grains.

After 500 h oxidation the plan view shows different surface features. Some areas are covered by platelets and needles and others are not (Fig. 5.5). This might be the result of either spallation of the oxide or different orientation of the grains of the substrate.

Fig. 5.6 shows the chemical profiles of the cross sections that have been performed with an electron probe micro analysis, EPMA. The different layered components, RuAl bulk,  $\delta$ -Ru and  $\alpha$ -Al<sub>2</sub>O<sub>3</sub>, are well distinguished; the magnified profile reveals that the Al content along the Ru layer thickness is 3 at% next to the RuAl bulk and less than 1 at% next to the scale.

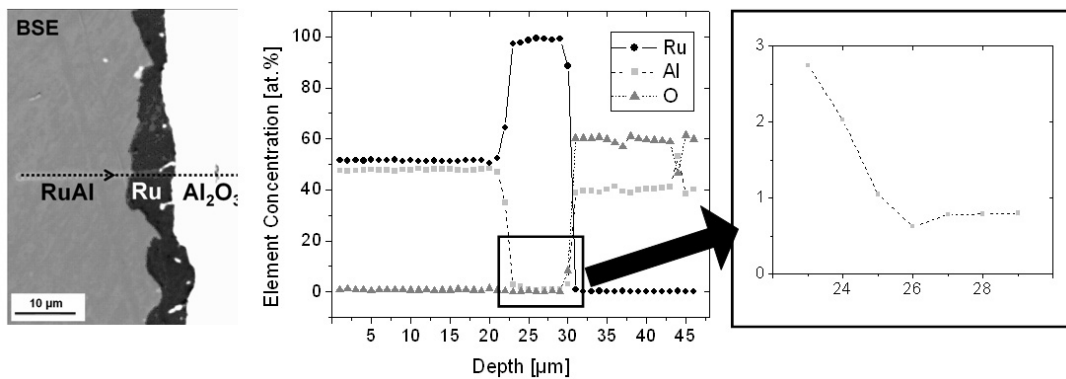


Fig. 5.6 EPMA line scan of the cross section of an arc-melted sample oxidized for 500 h. at 1100°C. The profile of the Al concentration within the  $\delta$ -Ru layer is shown in detail; an electron back scanned picture of the analyzed area is also reported.

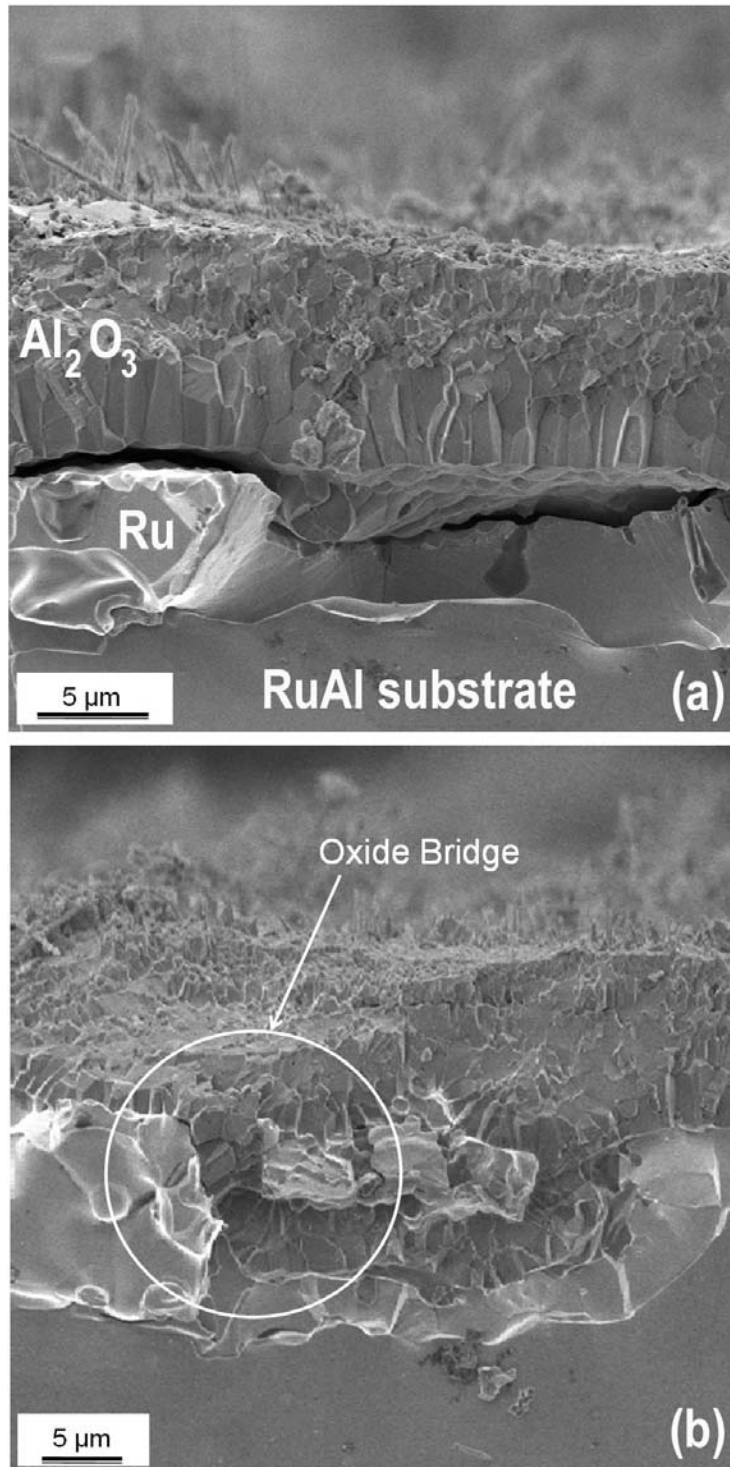


Fig. 5.7 SEM pictures of a fractured cross-section after oxidation in air for 500 h at  $1100^\circ\text{C}$ . (a)  $\text{Al}_2\text{O}_3$  scale, Ru layer and RuAl substrate are observed. The oxide is composed of needles, equiaxed and columnar grains. (b)  $\text{Al}_2\text{O}_3$  columns growing perpendicular to the Ru layer in the bridges.

Fig. 5.7a is a SEM micrograph of a fractured cross-section of a sample oxidized for 500h showing the TGO microstructure: equiaxed  $\alpha\text{-Al}_2\text{O}_3$  grains next to the gaseous phase and columnar morphology next to the  $\delta\text{-Ru}$  layer. It can be seen that in some areas the oxide has broken through the  $\delta\text{-Ru}$  layer and a consequence of this cracking is the formation of a new oxide layer parallel to the initial one, where the two layers are connected by “oxide bridges” (Fig. 5.7b). These bridges show a columnar structure, and the columnar grains are always perpendicular to the  $\delta\text{-Ru}$  phase.

A polished cross-section shows different features of the oxide (Fig. 5.8). In some areas just two layers ( $\alpha\text{-Al}_2\text{O}_3$  and  $\delta\text{-Ru}$ ) are present (Fig. 5.8b). Numerous cavities are also present, whose shape gradually changes from the surface to the substrate, becoming rounder and thicker (Fig. 5.8c). At the edge of the specimen couples of alternating layers of  $\alpha\text{-Al}_2\text{O}_3$  and  $\delta\text{-Ru}$  are formed and some oxide protrusions (highlighted in Fig. 5.8d) seem to have grown following cracking of the  $\delta\text{-Ru}$  layer.

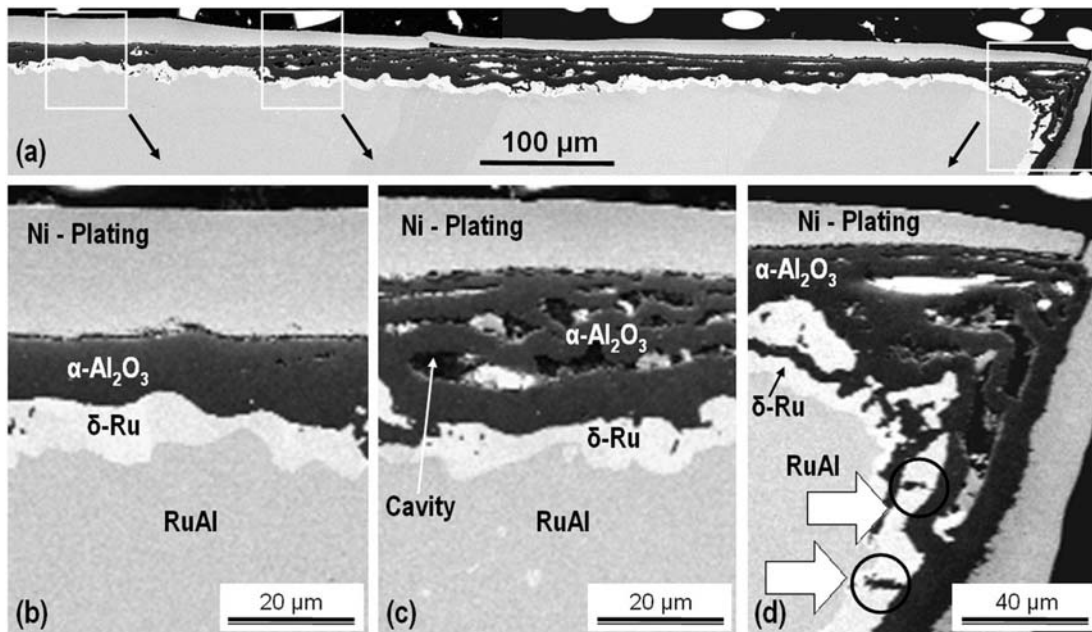


Fig. 5.8 SEM picture of the polished cross section after oxidation in air at 1100°C for 500 h. (a) Evolution of Ru-Al<sub>2</sub>O<sub>3</sub> layers over a large area: (b) a single couple of layers,  $\alpha\text{-Al}_2\text{O}_3/\delta\text{-Ru}$ ; (c) multi-cavities within the  $\alpha\text{-Al}_2\text{O}_3$  phase; (d) multi-cavities and multi-layers formed at the edge. Oxide protrusions growing at the cracks in the  $\delta\text{-Ru}$  layer are highlighted.



TEM was used in this study to provide more accurate information on the microstructure and chemistry of the system, especially at the cavity sites whose formation is considered fundamental for the understanding of the oxidation behaviour.

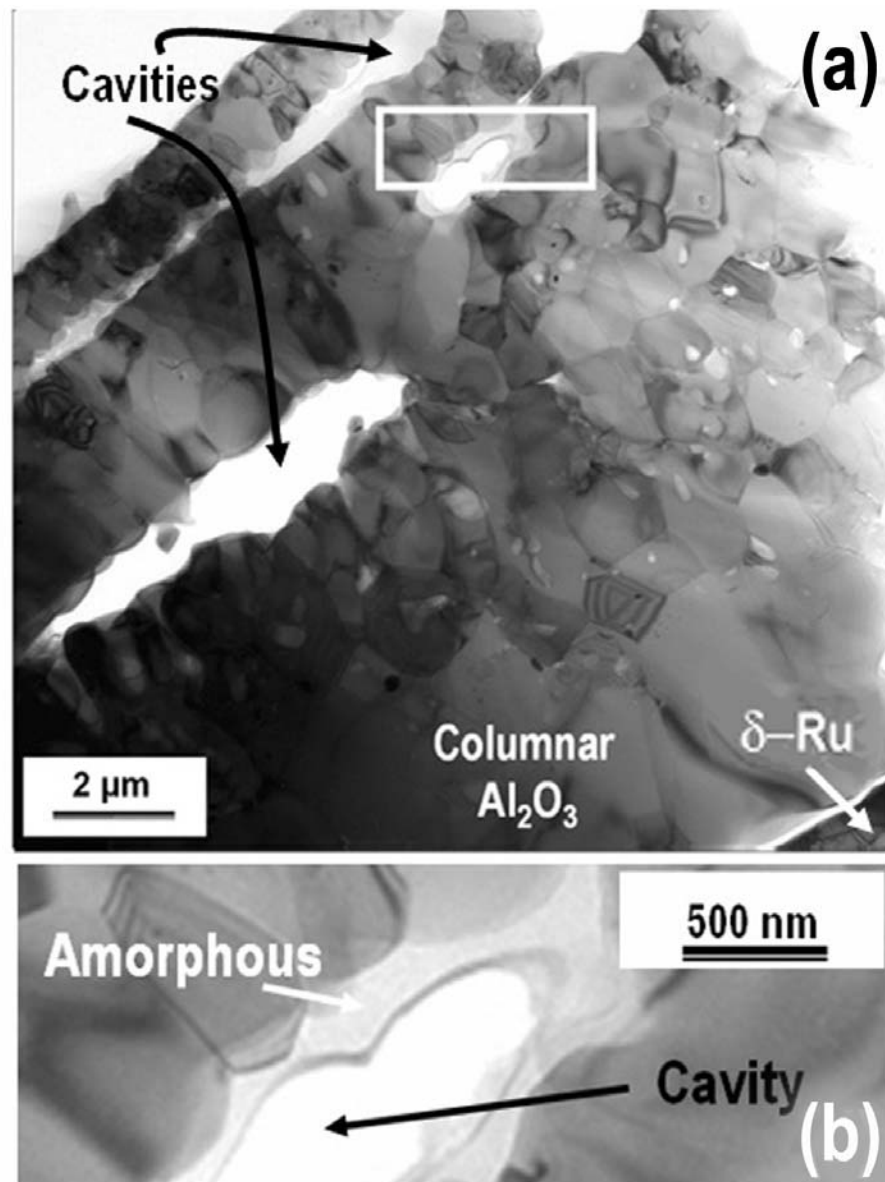


Fig. 5.9 Bright field (BF) cross section TEM pictures of the oxide formed after oxidation in air at 1100°C for 500 h, multi cavities are observed (a); detailed view of area squared in 'a' where an amorphous material is observed (b). (JEOL JEM 4000 FX)

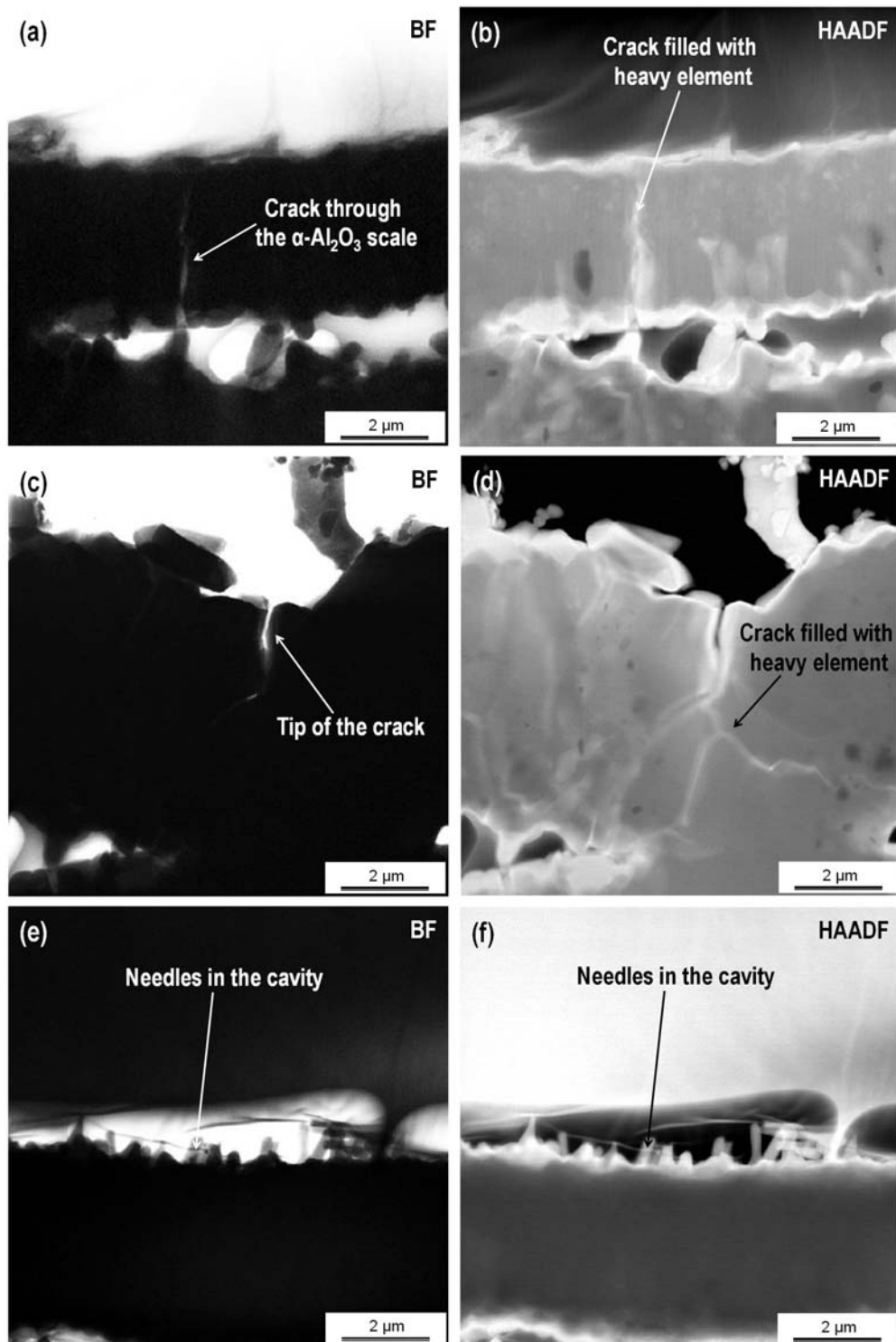


Fig. 5.10 BF/HAADF pictures after oxidation in air for 500 h. at 1100°C: (a/b, c/d) cracks through the  $\alpha$ -Al<sub>2</sub>O<sub>3</sub> scale filled with heavy element; (e/f) needles growing in a cavity. (VG 501)

It has been noticed that the columnar grains, that are parallel to the growing direction, are always oriented perpendicular to the  $\delta$ -Ru phase or to the cavities, as can be clearly seen after 500 h of oxidation (Fig. 5.9a), and are one order of magnitude larger than those observed after 1 h.

No evidence of texture was observed in the  $\alpha$ -Al<sub>2</sub>O<sub>3</sub> columnar structure.

TEM investigation of a sample oxidized for 500h revealed that an amorphous phase was present within the cavities and on the sample's surface (Fig. 5.9b). This amorphous phase is not a single-phase material but a more complete description of this multiphase material is following in par. 5.2.

A very important finding within this study was done using High Angle Anular Dark Field (HAADF) detector which evidences the atomic weight of the different phases through their different scattering properties, Z-contrast [Wil96]. Using this technique, cracks filled with heavy elements were detected in the  $\alpha$ -Al<sub>2</sub>O<sub>3</sub> scale (Fig. 5.10a, b, c, d). Furthermore, Al<sub>2</sub>O<sub>3</sub> needles which are a common sign of oxidation from vapour phase, were identified within the cavity (Fig. 5.10e, f).

### **Singularities of the RuAl substrate**

TEM investigations highlighted interesting features in the RuAl substrate. Composition and structure modifications have been observed.

Acicular Ru has been detected next to the  $\delta$ -Ru layer after 500 h oxidation in air. These needles present a width of approx. 50 nm and a length that can be longer than 500 nm (Fig. 5.11).

An SAD pattern in the [011] zone axis has been acquired from the RuAl substrate. Satellites reflections are observed both next to the principal reflections and in superlattice positions (Fig. 5.12).

The formation of these ordered secondary reflections is believed to be caused by a displacive modulation. More detailed information on Electron Diffraction may be found in [DeG03].

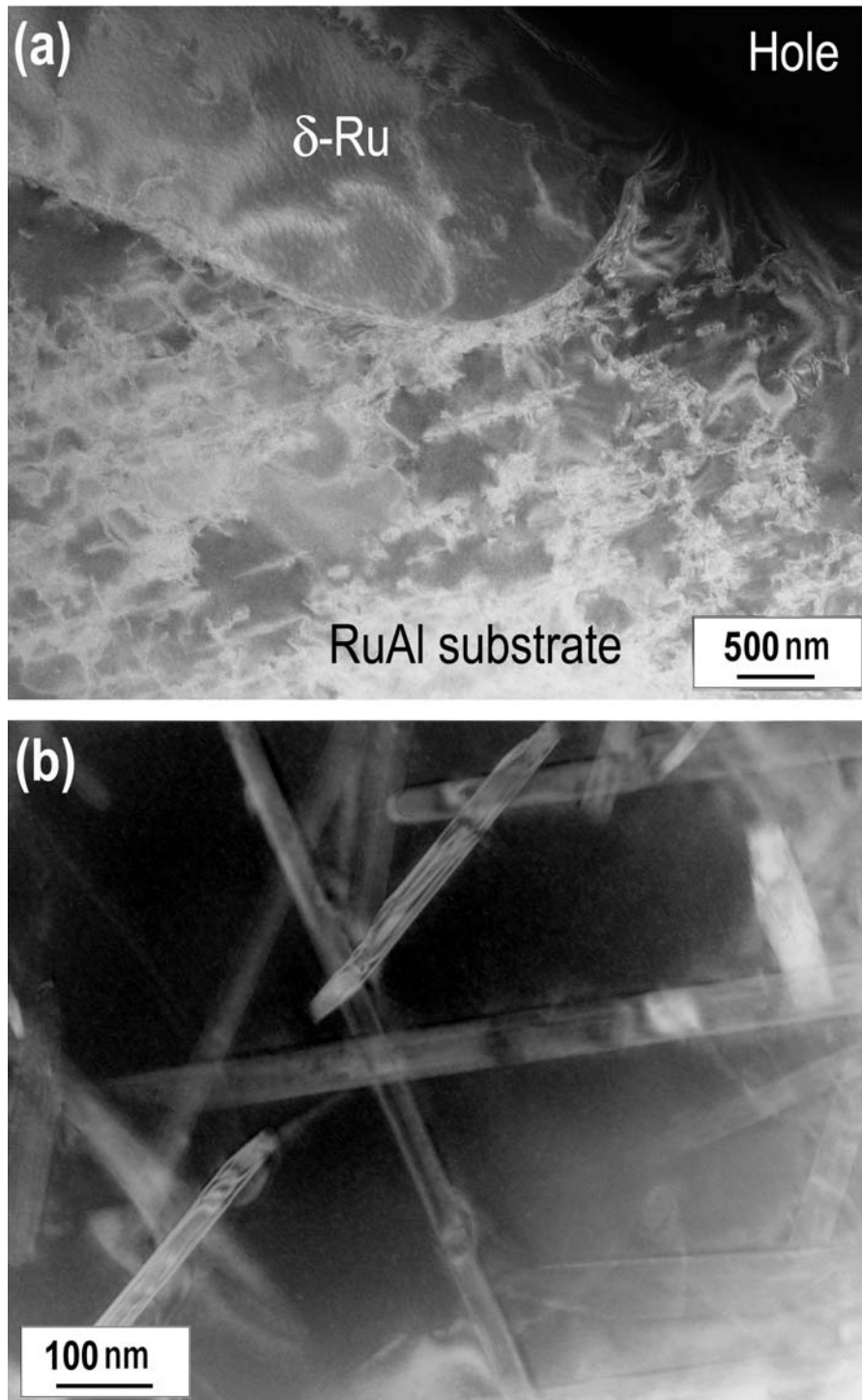


Fig. 5.11 Bright field (BF) cross section TEM pictures of the RuAl substrate after oxidation in air at 1100°C for 500 h. Acicular Ru is formed (a); detailed view (b). (JEOL JEM ARM 1250)

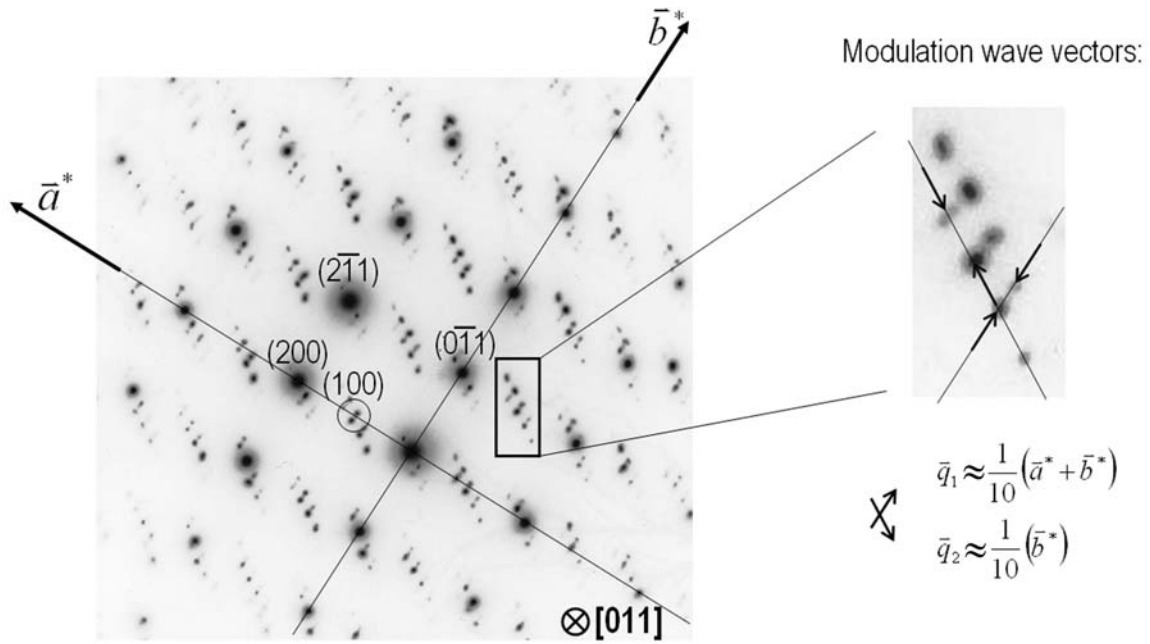


Fig. 5.12 SAD investigation of the RuAl substrate after oxidation in air for 500 h at 1100°C. Reflections arising from structure modulations are observed both next to the principal reflections and in double diffraction reflection sites. (JEOL 2000 FX)

The estimated modulation vectors are approximately:

$$\begin{aligned} \bar{q}_1 &\approx \frac{1}{10}(\bar{a}^* + \bar{b}^*) \\ \bar{q}_2 &\approx \frac{1}{10}(\bar{b}^*) \end{aligned} \quad (5.1)$$

where  $\bar{a}^*$  and  $\bar{b}^*$  are the reciprocal lattice basis vectors.

The cubic crystal structure in the [011] zone axis renders the (100) reflection in the kinematical approximation chemically dependent. Additionally, the large thickness of the sample and the not precise alignment of the Ewald sphere influence the intensities of the (100) reflections based on dynamic scattering.

Investigating at higher magnifications, an ordered contrast can be seen from high-resolution micrographs. This micrograph (Fig. 5.13) shows two RuAl grains. The Fourier transforms of the two grains show that both the grains are close to zone-axis orientations:  $[1\bar{1}3]$  the grain on the left and  $[111]$  the grain on the right.

The contrast effects, which arise from the high resolution image (Fig. 5.13), represent long wave length modulations. The direction and the sharpness of this contrast-effect are different on the two grains. These modulations are oriented in the  $\{112\}$  direction as indicated by the position of the satellite reflections (highlighted in the picture) in the FFT.

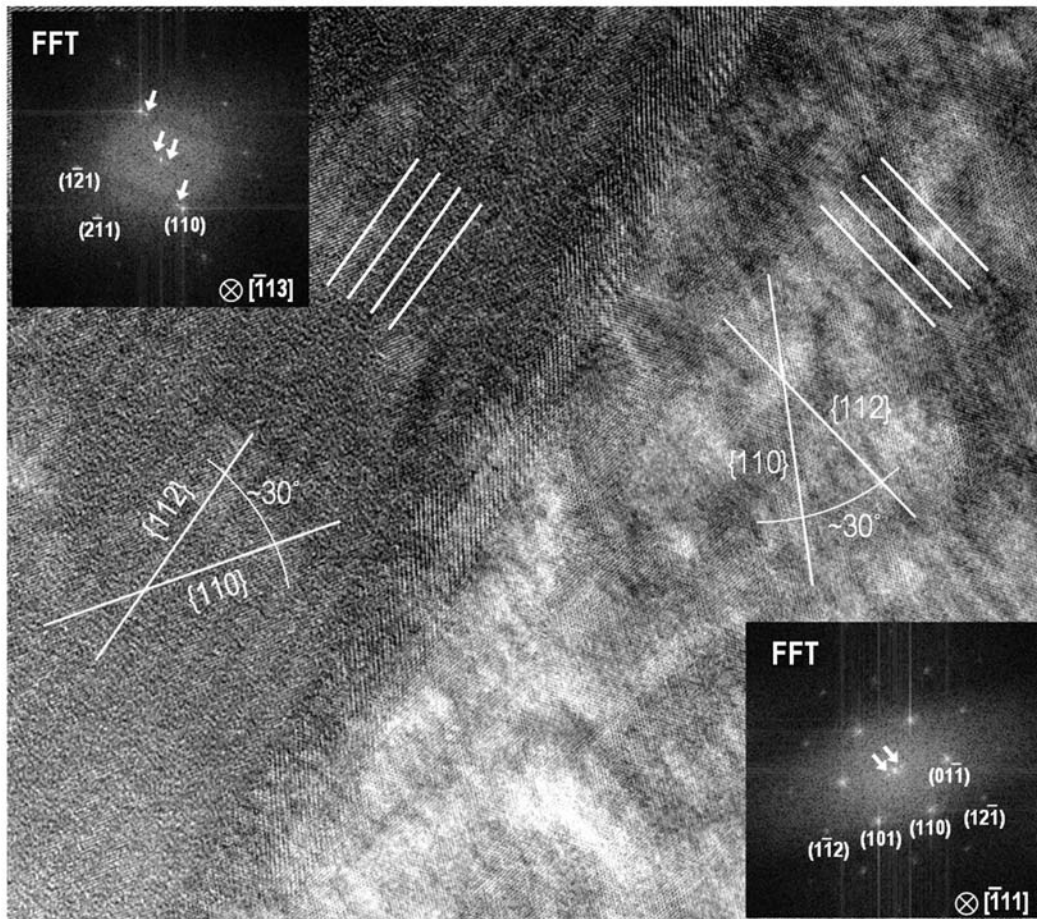


Fig. 5.13 HRTEM pictures of the RuAl substrate after oxidation in air for 500 h at 1100°C. A periodic contrast is observed on the two grains, which is represented by the satellite reflections highlighted in the Fourier transform. This modulation is oriented in the  $\{112\}$  direction. (JEOL JEM ARM 1250)

## 5.2 CHARACTERIZATION OF THE MULTIPHASE MATERIAL

The multiphase material has been detected in different samples after different oxidation times. In order to describe this material, different TEM techniques have been used, such as SAD, Z-contrast, EELS and in-situ high-temperature investigation.

### **SAD investigation**

Selected area diffraction was used to determine the structure of the multiphase material detected within the cavities (Fig. 5.14). A pattern taken from an area containing both the  $\delta$ -Ru layer and the material in the cavity (area C) contains reflections from both phases. The individual ordered diffraction spots originate from a single grain of the  $\delta$ -Ru phase oriented in zone axis, while the diffraction rings arise from the polycrystalline material in the cavity, indicating that small crystalline particles are present in this region. In the SAD pattern obtained from both the material in the cavity and the  $\text{Al}_2\text{O}_3$  on top (area A), the set of ordered diffraction dots correspond to the diffraction of the  $\text{Al}_2\text{O}_3$  grain oriented in the  $[10\bar{1}1]$  direction. It is concluded that diffraction rings do not correspond to polycrystalline  $\text{Al}_2\text{O}_3$  as the corresponding indexed lattice parameters do not fit with any of those interplanar spacings possible for the  $\alpha$ - $\text{Al}_2\text{O}_3$  structure. A SAD pattern obtained only from the material in the cavity (area B) shows rings labeled from 1 to 6 in Fig. 5.14: the rings labeled 1 and 2 are undoubtedly attributable to diffraction of the  $\delta$ -Ru phase, while the remaining rings may correspond to both  $\delta$ -Ru or tetragonal  $\text{RuO}_2$  structures.

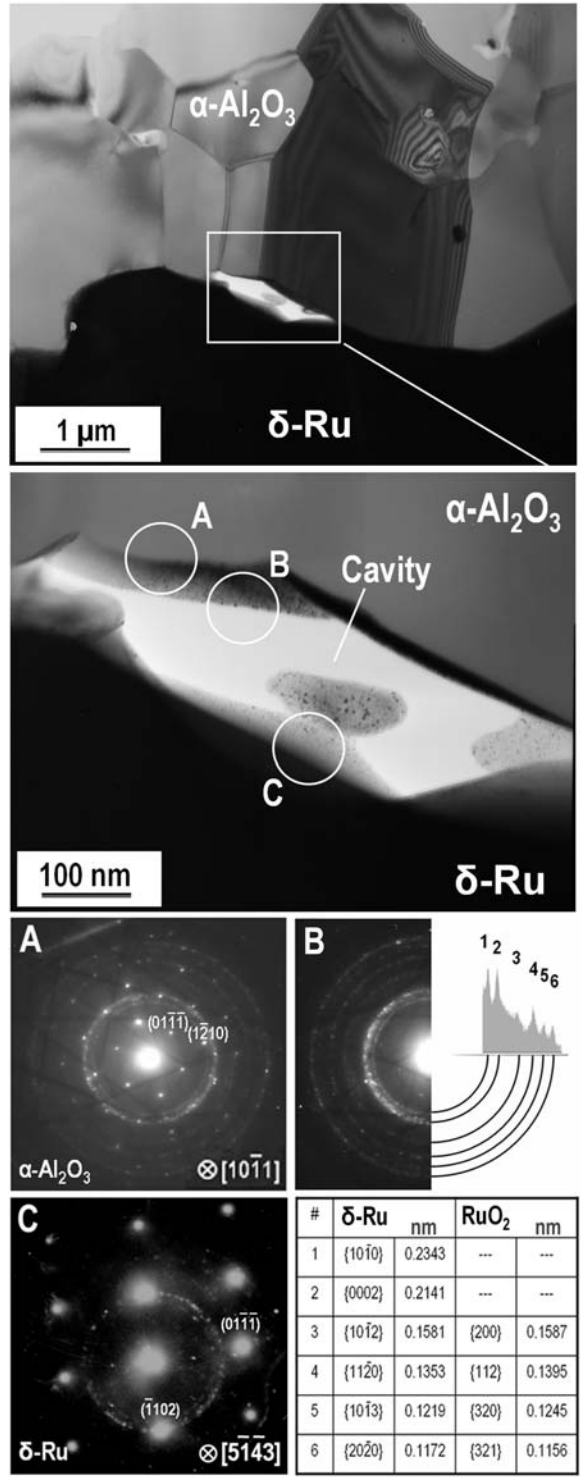


Fig. 5.14 Bright field TEM picture of a cavity (see detail) formed between the oxide scale and the  $\delta$ -Ru layer. SAD investigation at a cavity site formed after oxidation in air for 500 h at 1100 °C. (A)  $\alpha$ -Al<sub>2</sub>O<sub>3</sub> and polycrystalline feature (not  $\alpha$ -Al<sub>2</sub>O<sub>3</sub>); (B) polycrystalline pattern of  $\delta$ -Ru, see Tab; (C)  $\delta$ -Ru and polycrystalline  $\delta$ -Ru. (JEOL 2000 FX)



### **Z-contrast and EELS investigation**

Using Z-contrast technique, the multiphase nature of this material could be identified in an easier way. In fact the crystalline particles embedded in the amorphous matrix are formed by heavier elements (Fig. 5.15). An important finding is that the multiphase material is seen to wet some of the  $\alpha$ -Al<sub>2</sub>O<sub>3</sub> grain boundaries (Fig. 5.15a, b).

This material is present also on the surface of the oxidized specimens. In the examined case (Fig. 5.16), there is no evidence of the crystalline particles; the material appears complete amorphous and made of Al, Ru, O and N. The quantification reported might not be precise due to the fact that oxygen and nitrogen are light elements. EDS is inefficient for the quantification of such elements.

Electron energy loss spectroscopy (EELS) investigations evidenced the presence of Al, O and Ru in the matrix of the multiphase material (Fig. 5.17a, c). The characteristic features of the electron loss near-edge structure (ELNES) for Al (L<sub>2, 3</sub>) do not agree with the amorphous Al<sub>2</sub>O<sub>3</sub> [Bou03], and it is also different from the  $\alpha$ -Al<sub>2</sub>O<sub>3</sub> structure (Fig. 5.17b, [Bou03]). It must be noticed that the EEL spectra, shown as reference for  $\alpha$ -Al<sub>2</sub>O<sub>3</sub>, has been acquired from a needle grown on the oxide surface.

The energy signal from the M<sub>4</sub> and M<sub>5</sub> edges of Ru in the matrix seems to correspond more to the metallic Ru (Fig. 5.17d, [Rei83]) than to the Ru-oxide (Fig. 5.17f, [Ahn04]). However, it must be noticed that this signal can not be related to carbon, despite there is a correspondence with the edge position, due to the fact that carbon contamination has not been observed in other areas of the sample.

The EEL spectra, acquired from a particle of the multiphase material, shows the characteristic Ru edges and a small O edge (Fig. 5.17e). The ELNES from the M<sub>4</sub> and M<sub>5</sub> edges of Ru shows more similarities to Ru-oxide (Fig. 5.17f) than to Ru metallic (Fig. 5.17d). In fact the edge does not appear as steep as it is for the metallic Ru.

The signal from nitrogen could not be detected neither in the matrix nor in the particles. This might be caused by the fact that the nitrogen peak is situated on the shoulder of the Ru peak, which raises the detectibility limit for nitrogen.

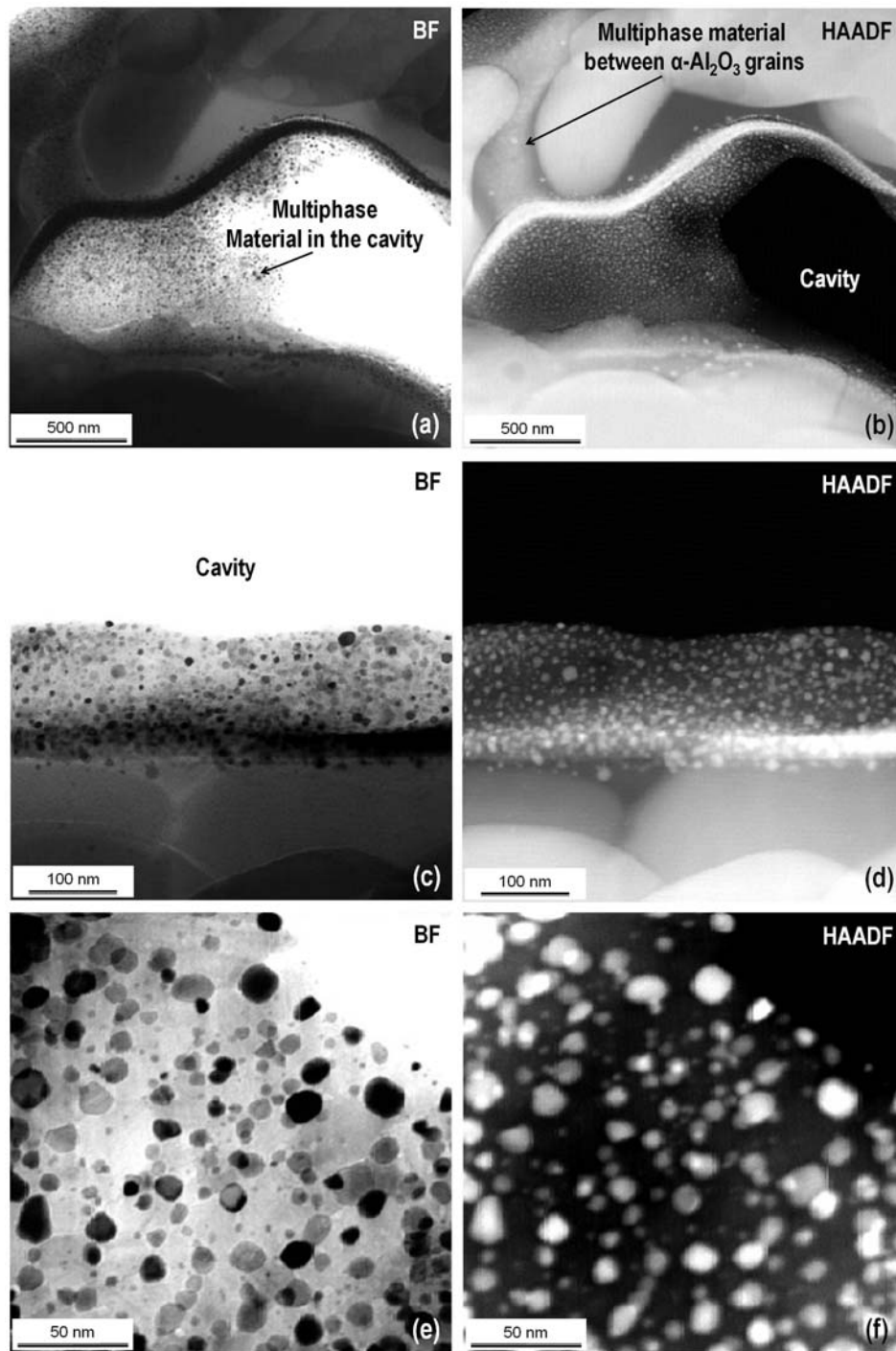


Fig. 5.15 BF/HAADF pictures of the multiphase material formed after oxidation in air for 500 h at 1100°C: (a/b) overview of the multiphase material filling partially the cavity and wetting an  $\alpha$ -Al<sub>2</sub>O<sub>3</sub> grain boundary ; (c/d) the darker (brighter) band in a (b) corresponds to zones with a higher precipitates density; (e/f) detail of the precipitates. (VG 501)

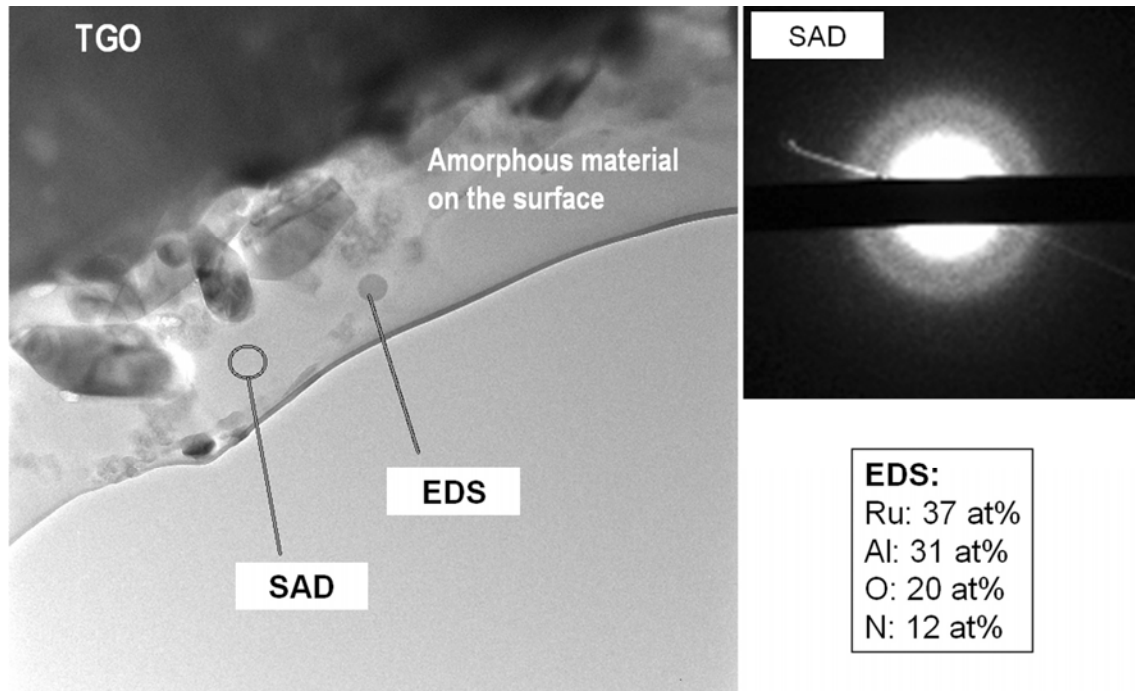


Fig. 5.16 Bright field (BF) cross section TEM pictures of the oxide formed after oxidation in air at 1100°C for 30 h. SAD and EDS of the amorphous material observed on the surface are reported. (ZEISS LIBRA200FE)

### **In-situ High-temperature investigation of the Multiphase Material**

The morphology of the multiphase material consists of nano-particles of Ru, which are partially oxidized and embedded in a Ru-Al-O-N amorphous matrix.

Such morphology suggested that this material does not contain the particles at high temperature and that they form due to precipitation. This statement is based on the assumption that the solubility of Ru decreases during cooling.

An investigation with a JEOL JEM ARM 1250 microscope has been conducted on a sample oxidized for 30 hours in air. The multiphase material was observed in-situ, increasing the temperature at different steps from RT to 950 °C. The experiment was meant to observe the evolution of the particles in the matrix. To conduct this experiment the TEM sample was prepared with a special glue (Gaphi-Bonf 551-R by T-E-Klebtechnik) from a RuAl sample oxidized in air at 1100 °C for 24 hours.

The crystalline structure of the particles can be seen in the high-resolution images (Fig. 5.18). The Fourier transform built from the particles' image is shown up to 500 °C. At

650 °C the particles were still visible but it was not possible to get a pattern from the Fourier transform.

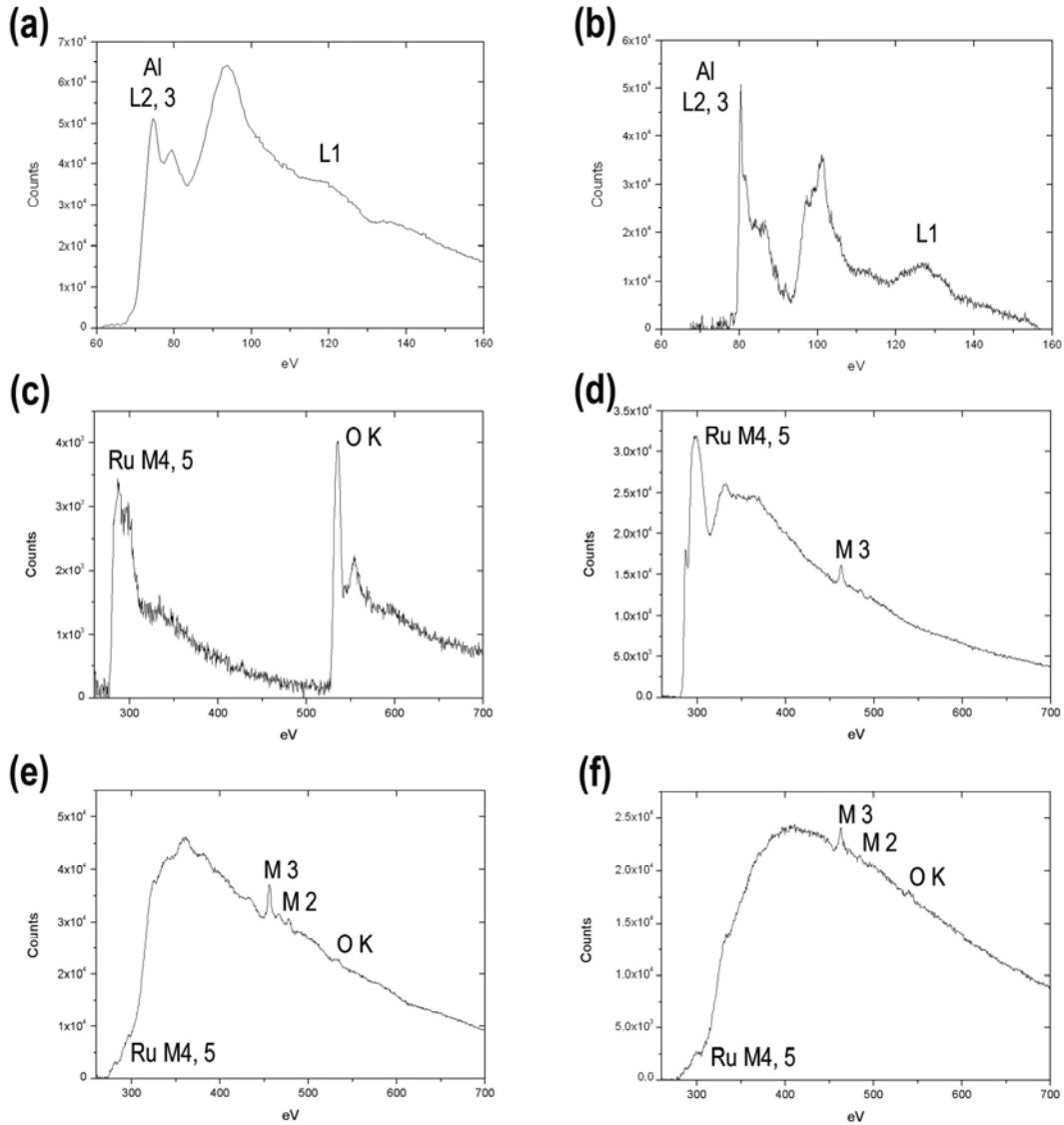


Fig. 5.17 EEL spectra (background subtracted) acquired: (a) from the matrix of the multiphase material showing Al edges; (b) as reference for  $\alpha$ -Al<sub>2</sub>O<sub>3</sub> from an alumina needle formed on the surface; (c) from the matrix of the multiphase material showing O and Ru edges; (d) as reference for the metallic Ru from the  $\delta$ -Ru layer; (e) from a particle belonging to the multiphase material showing Ru edges, a small signal from the O edge is also visible, no Al was detected in this spot; (f) as reference from a Ru-oxide particle located in the  $\alpha$ -Al<sub>2</sub>O<sub>3</sub> scale (not in the multiphase material), no Al was detected in this spot. (VG 501)

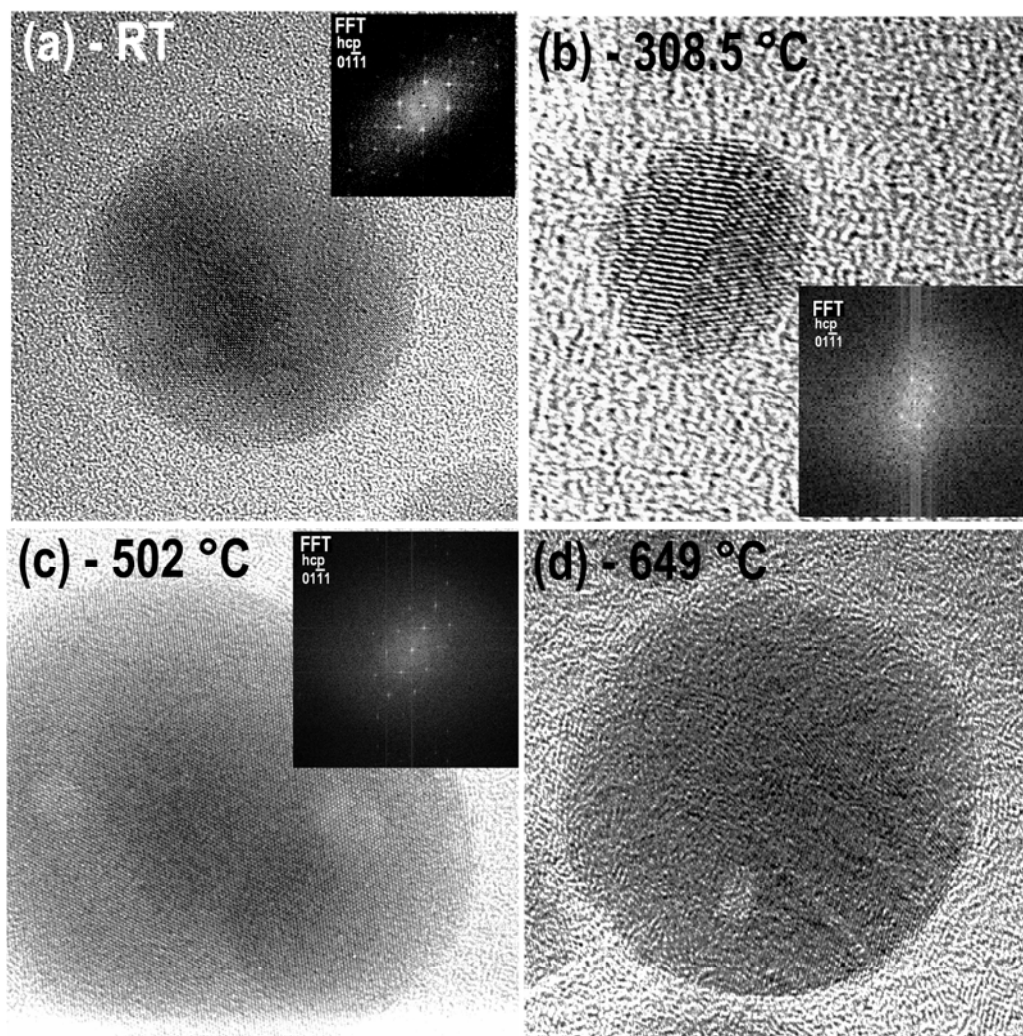


Fig. 5.18 HRTEM pictures of the multiphase material: Ru-rich particles are shown depending on temperature. (JEOL JEM ARM 1250)

The Fourier transform of the HR-pictures evidenced a hexagonal structure, which is characteristic of metallic Ru, whereas RuO<sub>2</sub> has a tetragonal crystal structure.

At temperatures higher than 800 °C the particles vanished, dissolved in the matrix. During cooling, some particles reappeared, confirming that their formation might be caused by a temperature dependence of the solubility of Ru in the Ru-Al-O-N phase.

The matrix of the material, which always appeared amorphous at RT, developed a partially ordered structure, known as turbostratic, at temperatures higher than 650 °C. This structure presented in some areas filament-like arrangements (Fig. 5.19).

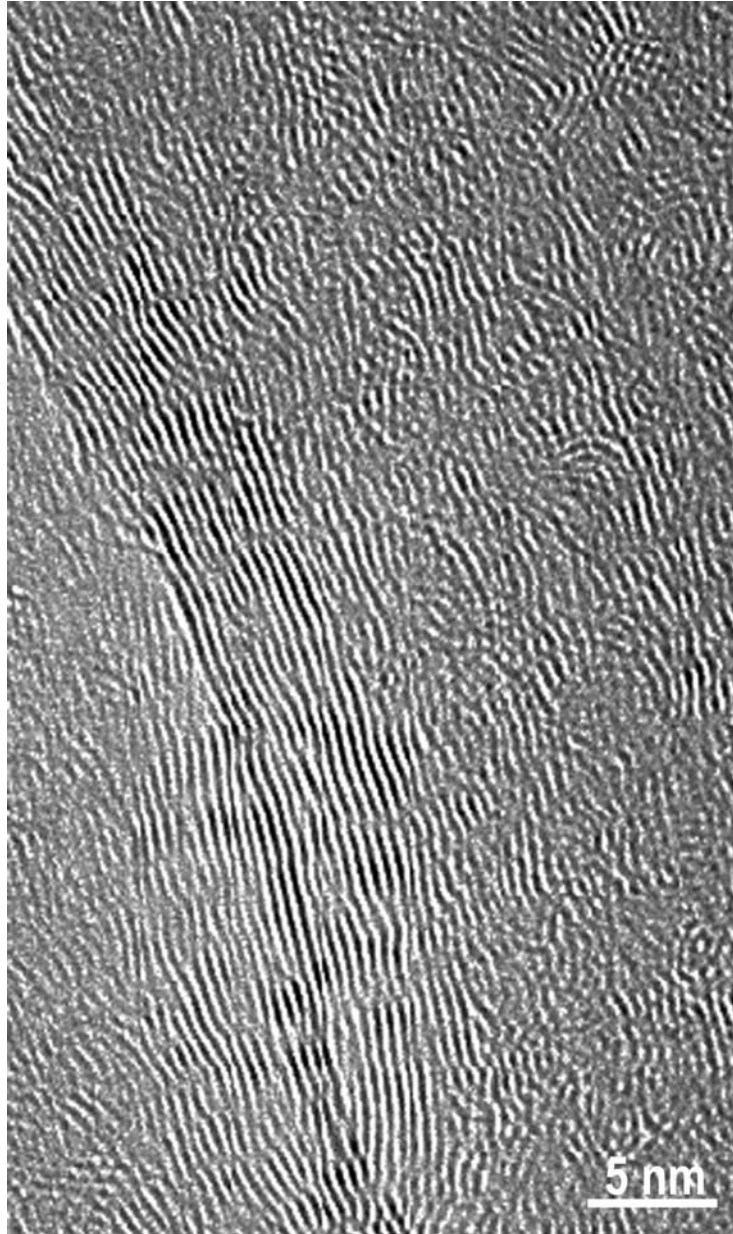


Fig. 5.19 HRTEM pictures of the multiphase material: the matrix is shown at 649 °C. The matrix that appeared completely amorphous at RT, shows in temperature a turbostratic morphology and some filament arrangement is also observed. (JEOL JEM ARM 1250)

### 5.3 OXIDATION'S KINETICS: AIR vs. O<sub>2</sub> PLUS Ar

In-situ XRD and TGA have been conducted in order to describe the growth kinetics of the oxide.

RuAl was obtained by induction melting and three RuAl specimens (10 x 10 x 1 mm) were polished to a mirror-like surface through 1  $\mu\text{m}$  diamond paste. The first specimen was analyzed with X-rays of the synchrotron at Argonne National Laboratory. In-situ diffraction investigation was performed during high temperature oxidation in static air. The other two specimens have been investigated using TGA in two different oxidizing atmospheres: (i) in static air and (ii) in static O<sub>2</sub> plus Ar.

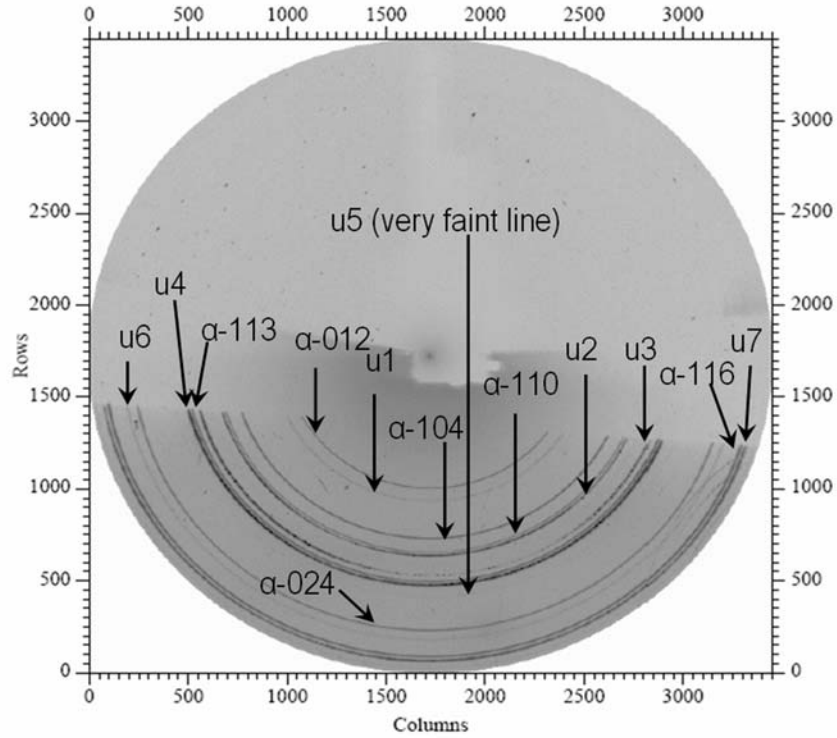
The same thermal cycle has been run for all the three specimens analyzed: heating at a rate of approximately 1000 °C/h, maintaining constant temperature at 1100 °C for 24 h, and cooling to RT at a rate of approximately 300 °C/h.

During the in-situ XRD experiment, several Debye-Scherrer rings have been observed. To every ring corresponds a phase and an orientation; the rings are shown and listed in Fig. 5.20. Intensities and stresses information (see par. 5.4) have been obtained from the signals highlighted in the figure.

The  $\alpha\text{-Al}_2\text{O}_3$  and the  $\delta\text{-Ru}$  layers grown during the experiment are thin; thus the intensities of X-rays should be proportional to the oxide thickness. The evolution in time of the intensities is plotted in Fig. 5.21.

It should be noticed that at the beginning the growth of  $\alpha\text{-Al}_2\text{O}_3$  and  $\delta\text{-Ru}$  followed a parabolic law. While  $\alpha\text{-Al}_2\text{O}_3$  conserved the same behaviour during all the oxidation time, the parabolic growth of  $\delta\text{-Ru}$  suddenly decreased after 10 hours. The signal became more scattered, and this coincided with an increase of the RuO<sub>2</sub> signal (Fig. 5.22). Most likely it is that after 10 hours the  $\delta\text{-Ru}$  phase starts to oxidize and evaporates as RuO<sub>3</sub> and RuO<sub>4</sub>. This would explain both the slower growth rate of the Ru-phase, due to consumption, and the increased signal from RuO<sub>2</sub>.

It must be noted that the signal of RuO<sub>2</sub> increased considerably during the heating of the specimen. Once the temperature of 1100 °C was reached, the signal reduced slightly its intensity (for 45 min) and then it continued to grow as the oxidation proceeded. Both the RuO<sub>2</sub> signals shared the same behaviour.



plane	d-spacing	Time of appearance
(110) RuO <sub>2</sub>	3.165	30 min
(100) Ru	2.322	20 min
(002) Ru	2.122	20 min
(101) Ru	2.036	20 min
(210) RuO <sub>2</sub>	1.946	140 min
(211) RuO <sub>2</sub>	1.671	30 min
(102) Ru	1.566	20 min
(01.2) α-Al <sub>2</sub> O <sub>3</sub>	3.462	30 min
(10.4) α-Al <sub>2</sub> O <sub>3</sub>	2.530	30 min
(11.0) α-Al <sub>2</sub> O <sub>3</sub>	2.361	30 min
(11.3) α-Al <sub>2</sub> O <sub>3</sub>	2.066	30 min
(02.4) α-Al <sub>2</sub> O <sub>3</sub>	1.723	30 min
(11.6) α-Al <sub>2</sub> O <sub>3</sub>	1.583	30 min

Fig. 5.20 Debye-Scherrer rings recorded onto the image plate detector. The observed signals are listed together with their d-spacing and time of appearance. The rings used for investigation are highlighted in the table.



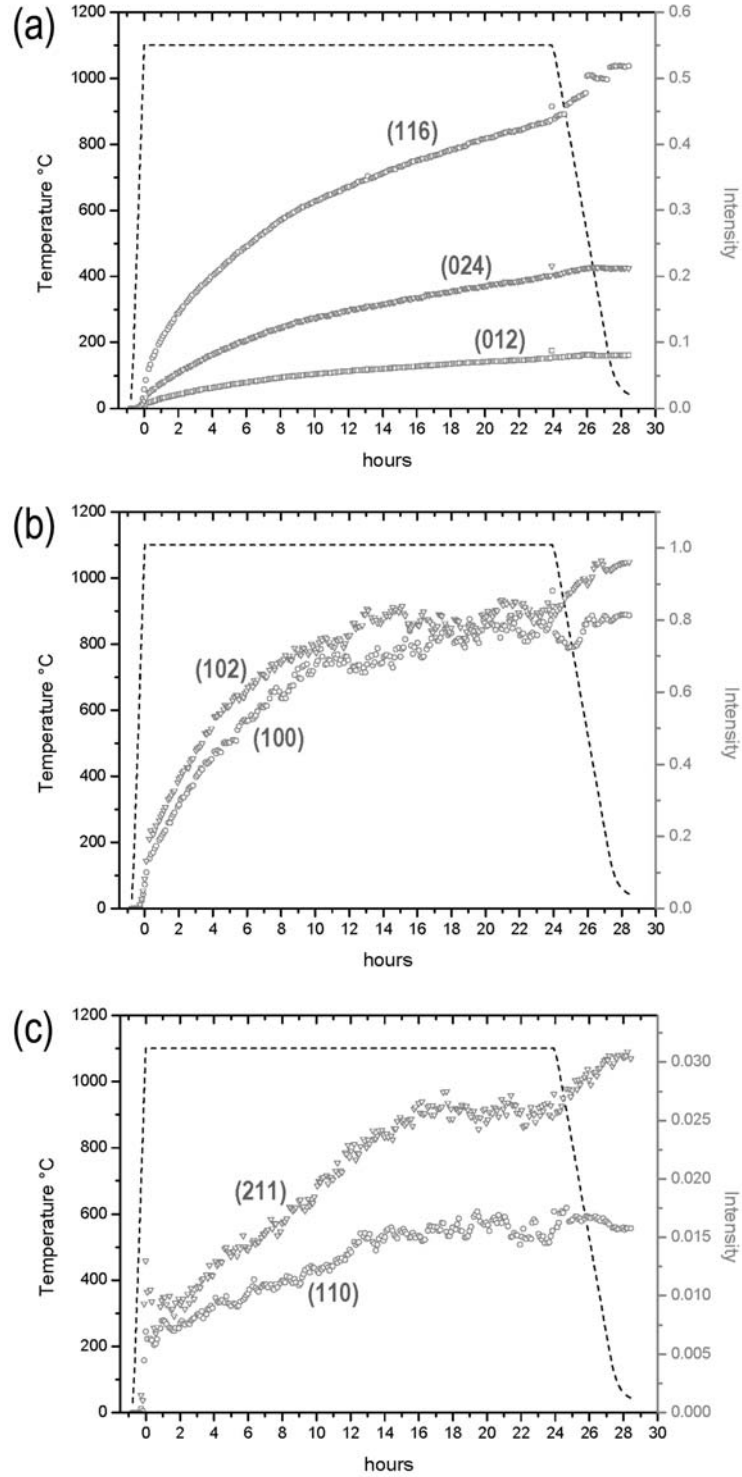


Fig. 5.21 Evolution of the intensities of different diffraction signals acquired in-situ during oxidation in air at 1100 °C at Argonne National Lab. Synchrotron: a)  $\alpha$ -Al<sub>2</sub>O<sub>3</sub>, b)  $\delta$ -Ru and c) RuO<sub>2</sub>.

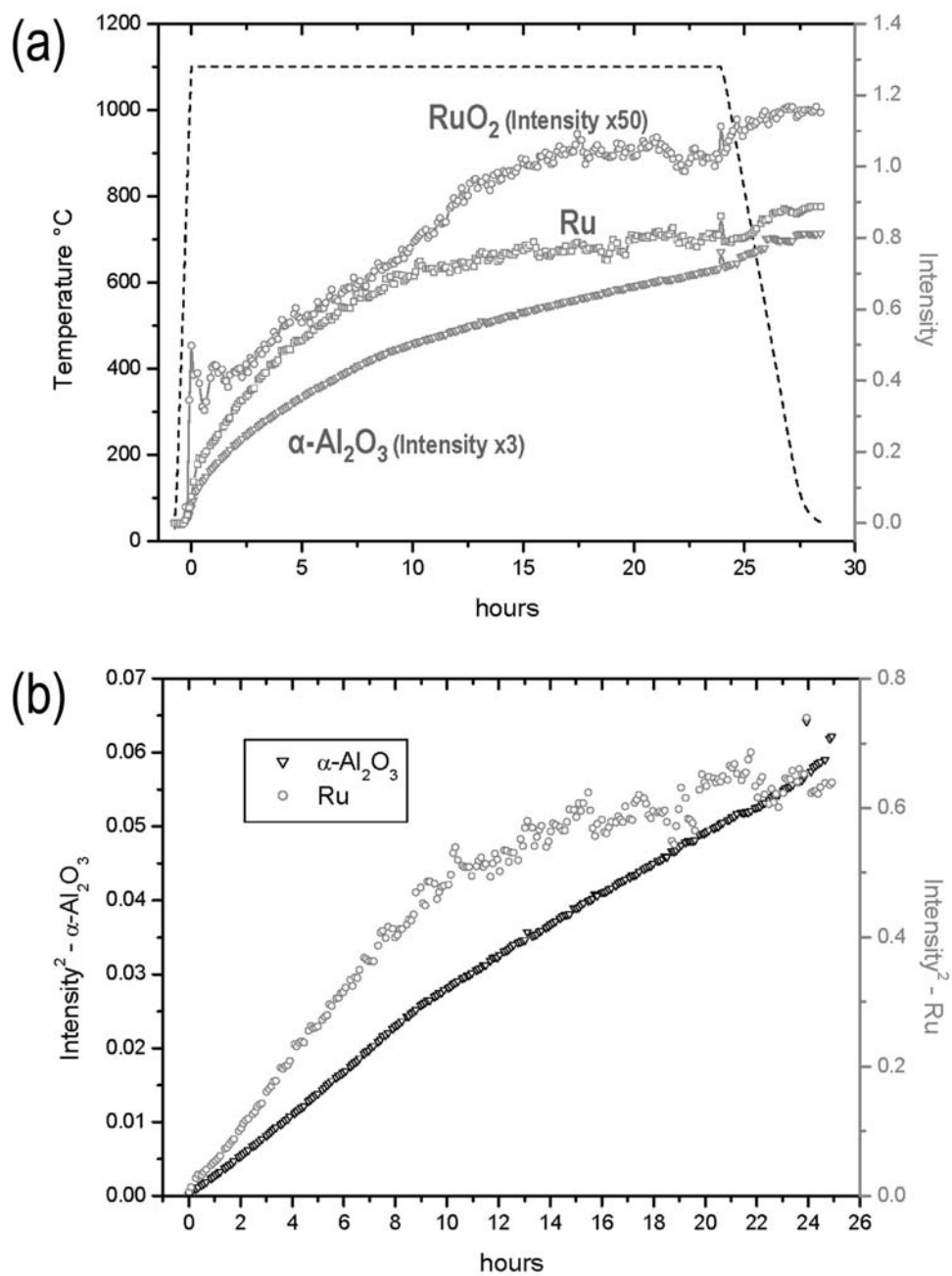


Fig. 5.22 Evolution of the intensities of different diffraction signals acquired in-situ during oxidation in air at 1100 °C at Argonne National Lab. Synchrotron: a) average of (116), (024), (012) for  $\alpha\text{-Al}_2\text{O}_3$ , (102), (100) for  $\delta\text{-Ru}$  and (211), (110) for  $\text{RuO}_2$ ; b) the signals of  $\alpha\text{-Al}_2\text{O}_3$  and  $\delta\text{-Ru}$  have been squared in order to evidence the parabolic behaviour.

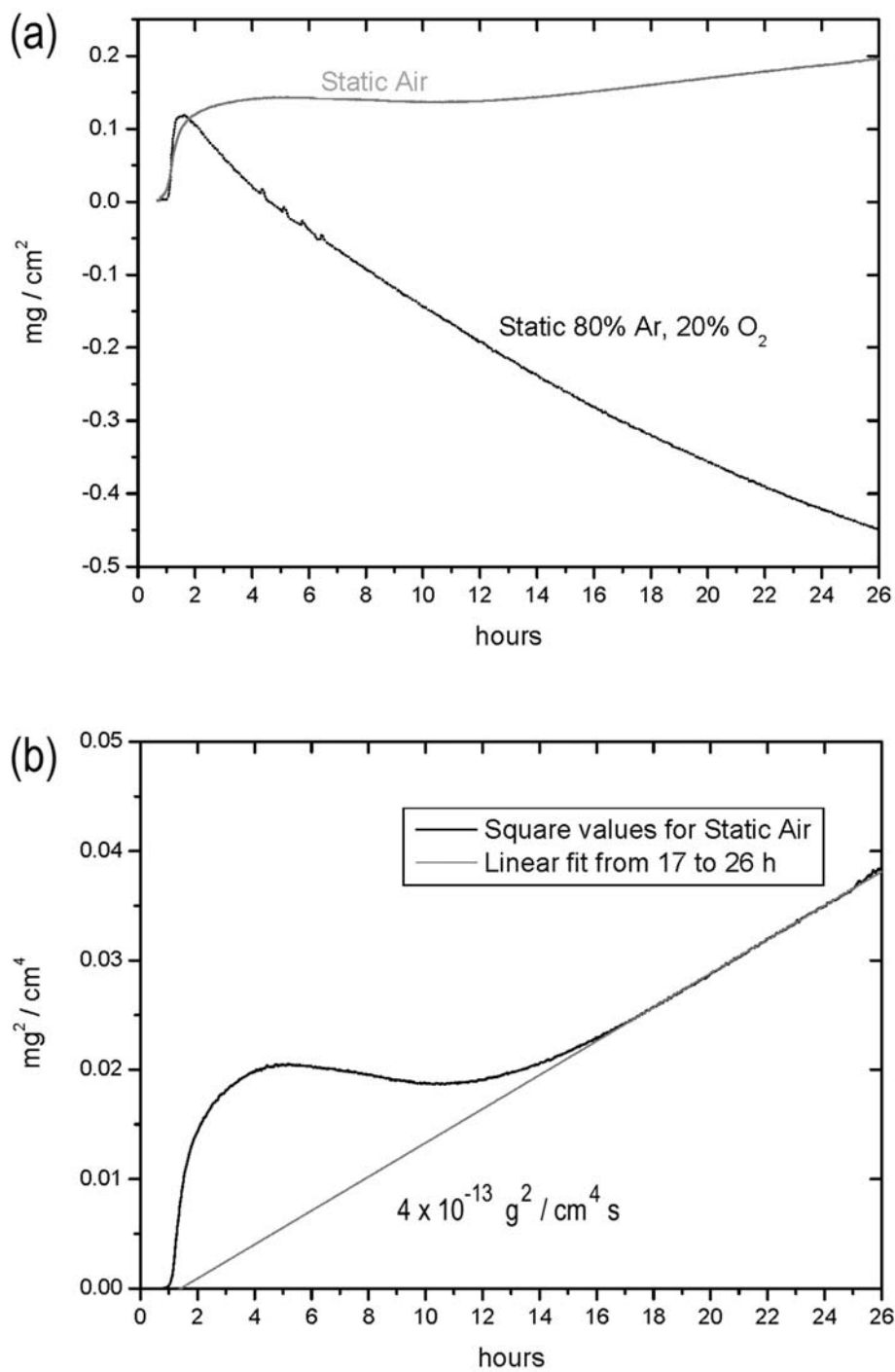


Fig. 5.23 TGA graphs showing the result of oxidation at 1100°C: (a) Static atmosphere of oxygen and argon mixture compared to a static air atmosphere. (b) Square plot of the oxidation in static air, showing a parabolic behaviour after the first 17 hours.

During the initial heating of the sample both Ru- and Al-oxides form, until the point at which the volatilization of Ru-oxide becomes dominant. In this moment, the solid  $\text{RuO}_2$  still in contact with the gas phase, evaporates. This explains the short weight loss observed when the experimental temperature is reached.

The TGA experiments showed a variety of results, depending on the composition of the oxidizing atmosphere (Fig. 5.23a). The oxidation conducted in  $\text{O}_2$  plus Ar showed a gain of weight during the first half an hour of oxidation at  $1100^\circ\text{C}$ . However, after the initial period, the measurements showed a continuous loss of weight, which can be explained by a simultaneous combined effect of oxide spallation and evaporation of  $\text{RuO}_3$  and/or  $\text{RuO}_4$ .

The oxidation in air, instead, resulted in a gain of weight, although a small loss of weight occurred between 6 and 13 h oxidation time. The square values of the weight change during oxidation in air were plotted; it can be observed that the gain of weight during the last period of the oxidation in air tends to a parabolic law (Fig. 5.23b).

Transverse cross-sections of the two samples have been prepared for microscopy investigation by polishing the surface tilted with a very low angle (Fig. 5.24), wedge-shaped cross section. The polished plane represents a broad view of the oxide scale, going from the surface down to the RuAl substrate. This method was used to facilitate the investigation across the TGO of phases different than  $\alpha\text{-Al}_2\text{O}_3$ .

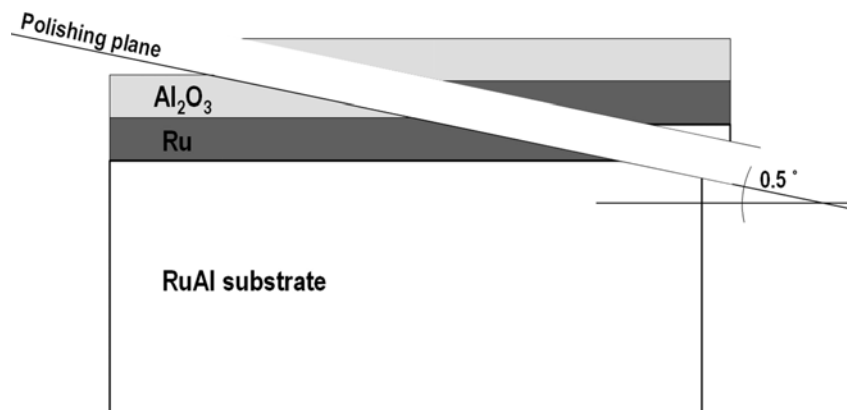


Fig. 5.24 Schematic drawing showing the low angle polishing method adopted for the Auger investigation. The samples have been polished by a tripod Techprep machine.

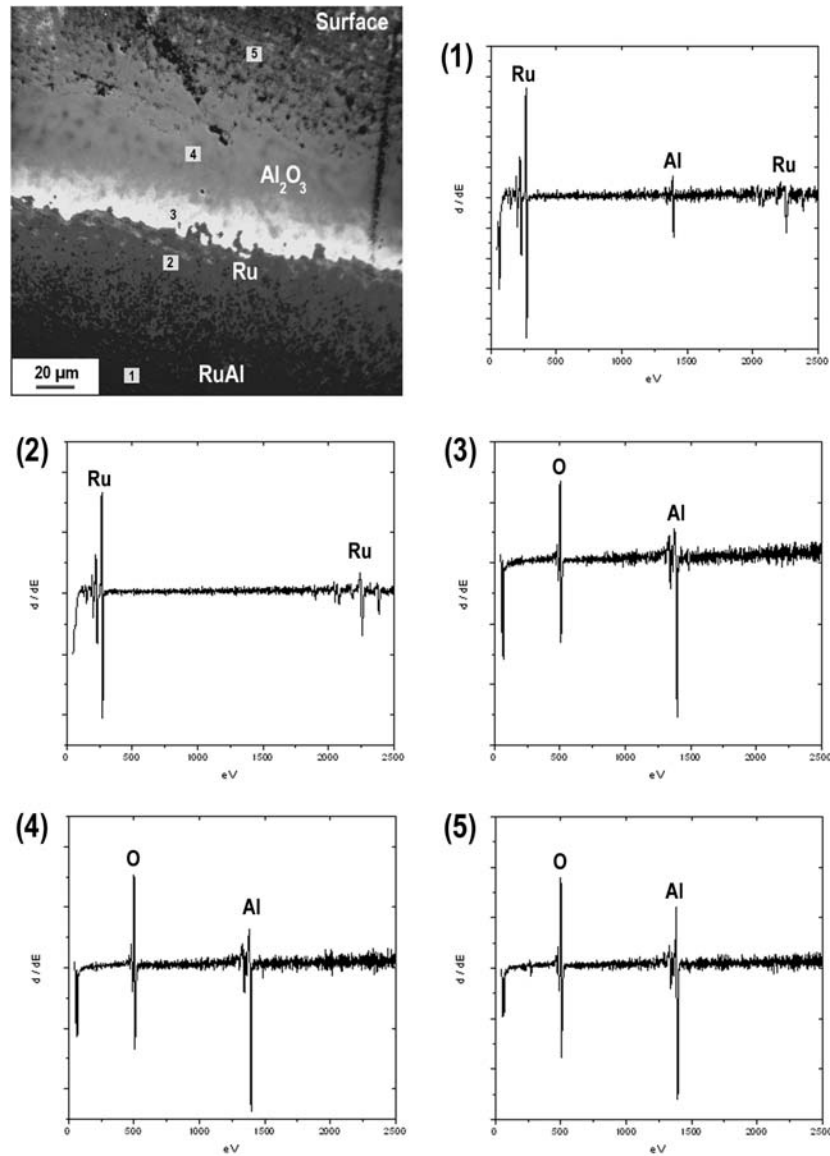


Fig. 5.25 SEM picture of low angle polished cross section, showing a sample oxidized in static oxygen plus argon atmosphere for 30 h. The Auger measurements correspond to the points marked in the picture.

Auger microanalysis has been conducted on such prepared surfaces in order to detect changes in composition between the two TGOs. The sample oxidized in O<sub>2</sub> plus Ar showed clearly the different phases: the RuAl substrate, the δ-Ru layer and the α-Al<sub>2</sub>O<sub>3</sub> scale (Fig. 5.25). The sample oxidized in air evidenced some differences. The measurements showed that Ru, Al, O and N are present (Fig. 5.26), suggesting that it is the multiphase material as described previously (par. 5.1).

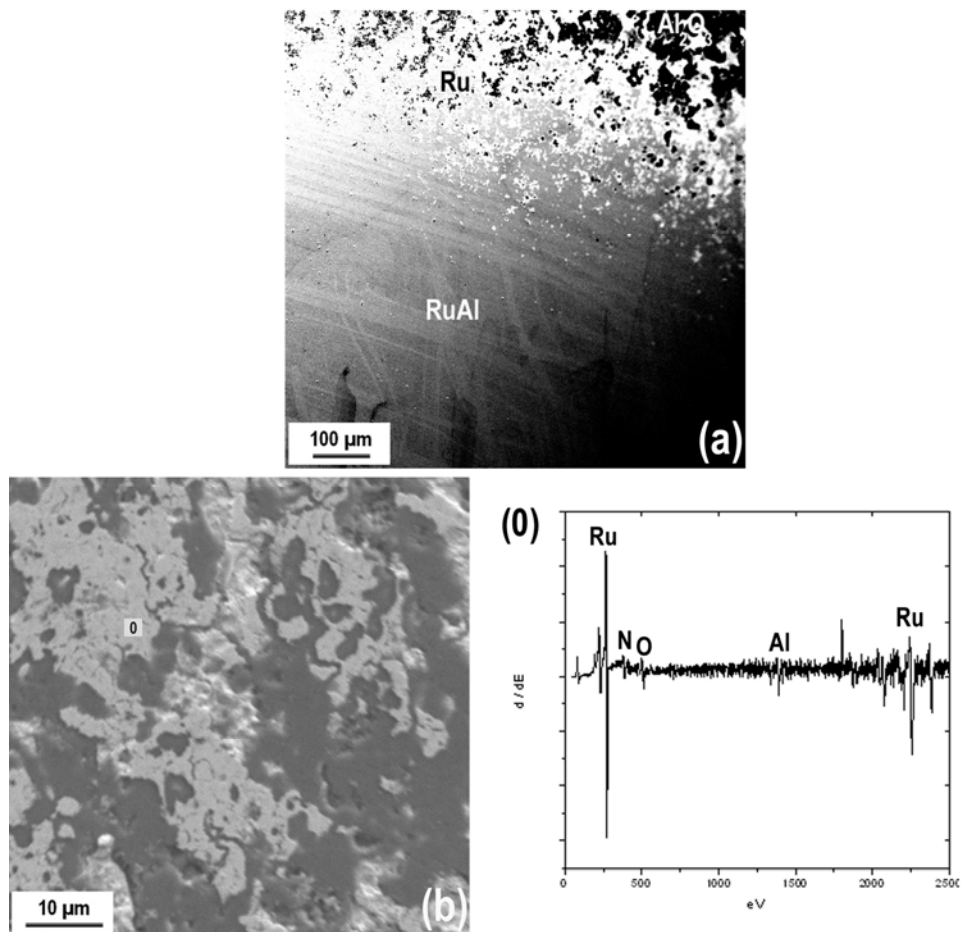


Fig. 5.26 SEM pictures of low angle polished cross section, showing a sample oxidized in static air for 30 h, (a); detail of the measured area, (b). The Auger measurement corresponds to the point marked in 'b'.

Additionally, other four samples have been oxidized and analyzed by XRD in order to understand if there is also some transient alumina phase involved in the oxidation mechanism. Two samples were oxidized at 1100 °C and the other two at 950 °C. The oxidation conditions used for the experiment at 1100 °C were: in static air for 0.2 h, and in static O<sub>2</sub> plus Ar for 0.2 h (Fig. 5.27). The conditions used at 950 °C were: in static air for 0.1 h, and in static air for 65 h (Fig. 5.28). No transient alumina was ever detected on the samples. It must be noticed also that the signal from RuO<sub>2</sub> has been detected only after oxidation in air.

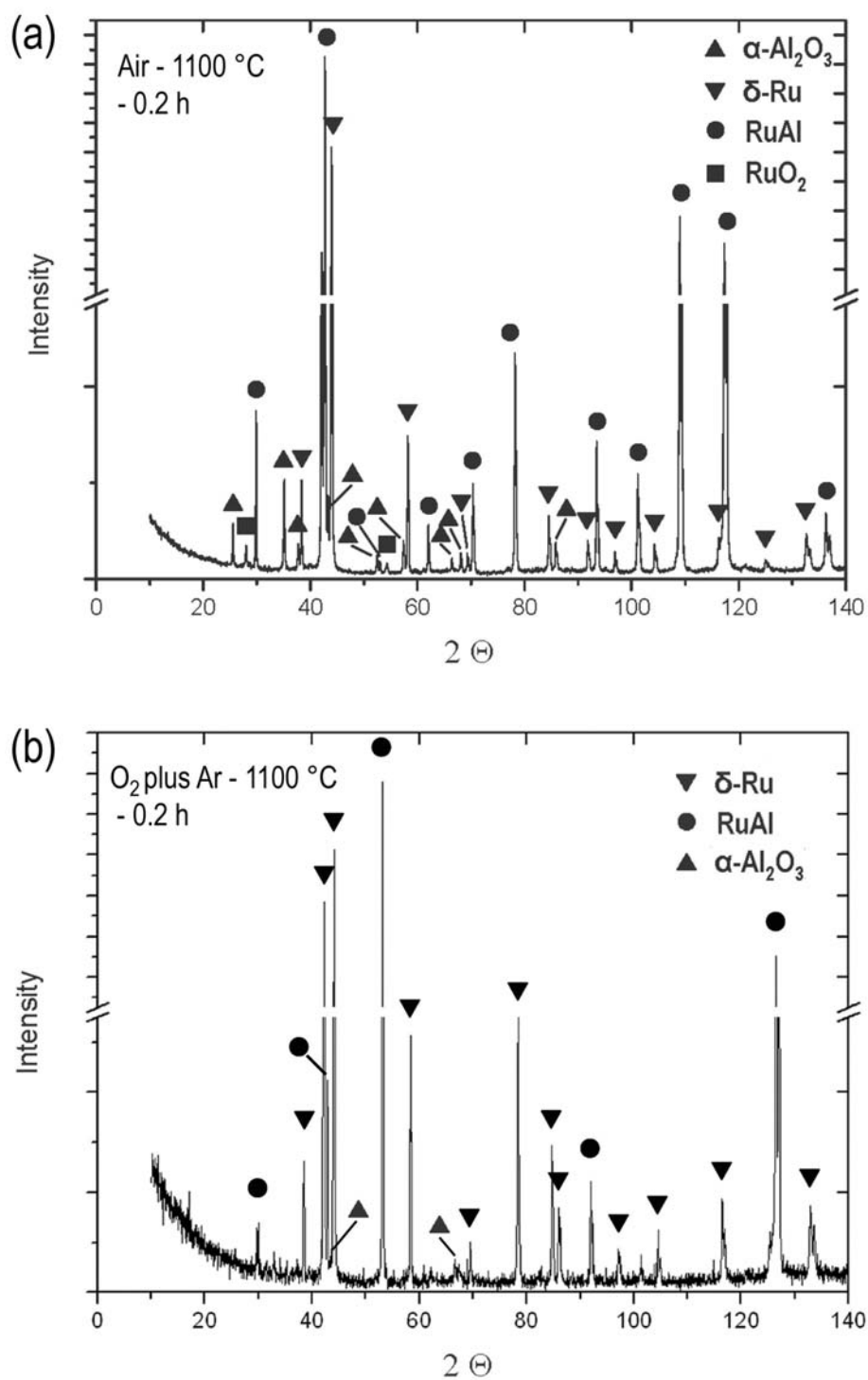


Fig. 5.27 X-ray pattern of RuAl after 0.2 h oxidation at 1100 °C in air (a) and in oxygen plus argon (b). For angles bigger than 80° the CuK $\alpha$ 1 and CuK $\alpha$ 2 radiations result in double peak morphology. The monochromator has not been used in order to acquire higher intensities.

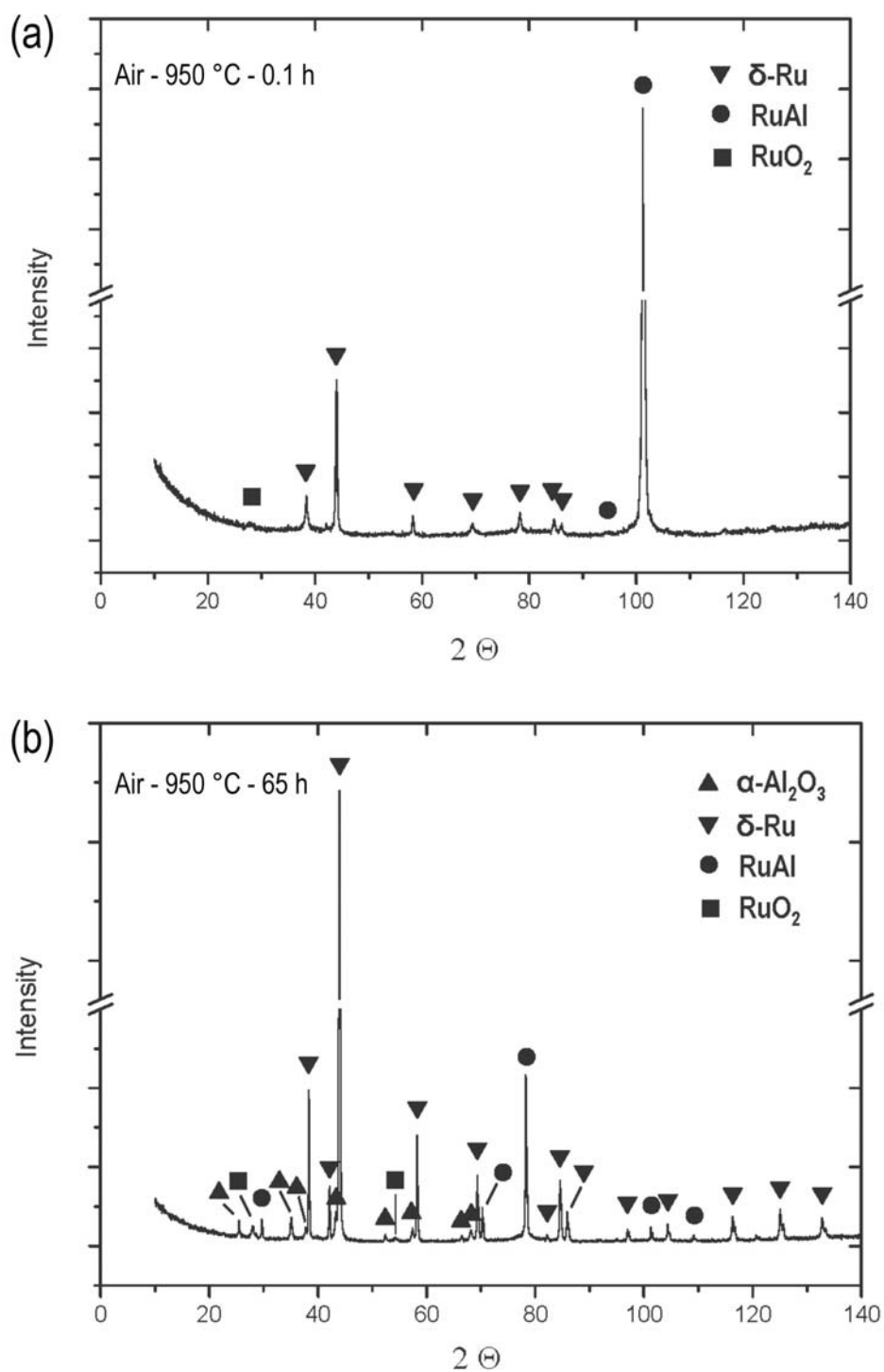


Fig. 5.28 X-ray pattern of RuAl after 0.1 h oxidation at 950 °C in air (a) and after 65 h oxidation at 950 °C in air (b). For angles bigger than 80° the CuK $\alpha$ 1 and CuK $\alpha$ 2 radiations result in double peak morphology. The monochromator has not been used in order to acquire higher intensities.



#### 5.4 EVAPORATION OF RuO<sub>3</sub> & RuO<sub>4</sub> DURING OXIDATION IN O<sub>2</sub> PLUS Ar

The evaporation of RuO<sub>3</sub> and RuO<sub>4</sub> is a crucial aspect in the oxidation of RuAl. In order to investigate the evaporation behaviour, three RuAl samples have been oxidized using TGA.

The samples were inserted in the furnace already in temperature in order to ensure rapid heating of the specimen, and the oxidizing atmosphere was controlled using a flow controller at the gas inlet.

The experiments have been performed alternating different  $P_{O_2}$  at 1100 °C on surfaces prepared by polishing through 1 µm diamond paste.

i) Oxidation in flowing O<sub>2</sub>: 20 sccm (standard cubic cm per minute) for 50 h (time for data acquisition 1.5 min).

Initially the specimen gained weight up to an oxidation time of about 30 min; afterwards it alternated losing and gaining weight periods (Fig. 5.29a, b).

ii) Mixed oxidation atmosphere: initially in static low oxygen partial pressure,  $P_{O_2} \sim 2$  mbar in Ar for 2.8 h, and afterwards in flowing O<sub>2</sub>, 50 sccm for 93 h (time for data acquisition 3 min).

A low  $P_{O_2}$  atmosphere was chosen in order to prove that the weight loss depends on the evaporation of gaseous Ru-oxides, exploiting the fact that the gaseous Ru-oxides' partial pressures depend logarithmically on the oxygen partial pressure (Fig. 2.2). Indeed, no drastic drop of weight was recorded until the beginning of the oxygen flow. (Fig. 5.29a, b).

iii) Oxidation in static low  $P_{O_2} \sim 2$  mbar in Ar for 3 h (time for data acquisition 10 s).

Same conditions of the first part of the experiment (ii), but with higher time resolution: weight acquired every 10 s (Fig. 5.29b, c).

As in the previous case, the plot of the weight change did not show a drastic weight loss, but after 40 min of monotonous mass gain, the weight measurements showed some fluctuations that may originate from cracking and spalling of the oxide scale or gaseous Ru-oxides evaporation.

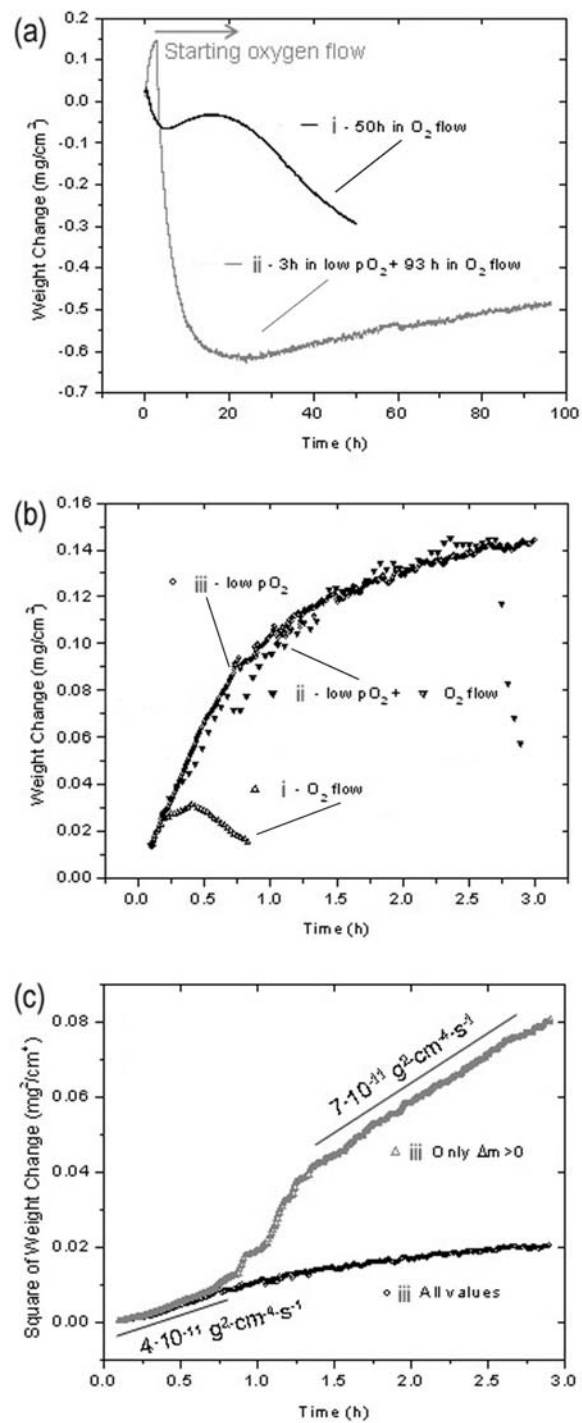


Fig. 5.29 TGA graphs showing the result of oxidation at 1100°C: (a) Experiments i and ii. (b) Experiment iii and details of the initial time for i and ii. (c) Square values of iii, considering all values and only the positive mass variations.

The square values of the weight change have been plotted by first using all the values, and afterwards by removing all the data indicating a weight loss. The weight measurements were re-considered as mass variations [ $\Delta m = m(t_2) - m(t_1)$ ], and the graph was re-plotted by omitting the negative variations. This method is approximate due to the concurrent events: the formation of  $\text{Al}_2\text{O}_3$  and the evaporation of the Ru-oxides. In spite of this, it is believed that this elaboration of the data should suggest whether the oxidation kinetics show a parabolic, which is expected for a continuous and well-adhered alumina scale [Bir83, Mil84], beyond the gaseous Ru-oxides evaporation behaviour (Fig. 5.29c). Except for a limited time, the elaborated square plot evidenced indeed a parabolic behaviour. The non-parabolic behaviour observed from 0.75 and 1.25 h (Fig. 5.29c) is believed to be caused by the spallation of small portions of the oxide scale; this, in fact, results in a direct contact between the bare metal and the gas phase, and, consequently, in a higher oxidation rate.

It must be noticed that the plan view of this sample evidenced a clear difference in the morphology of the TGO formed depending on the grain orientation of the substrate (Fig. 5.30). In particular it can be seen that the oxide formed on one grain showed to suffer cracking, resulting in the ridge morphology.

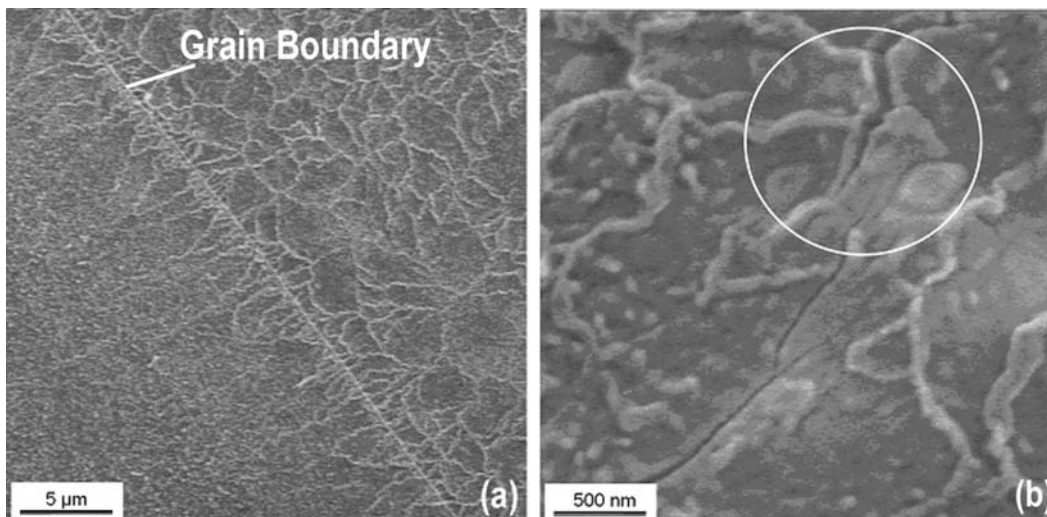


Fig. 5.30 SE-SEM plan view pictures after 3 h. oxidation at 1100°C in 2 mbar of oxygen partial pressure. (a) Oxidation depends on the RuAl grain orientation: an approximate flat and homogeneous oxide on the left and a surface characterized by a ridge network on the right. (b) The ridge in fig. (a) show to form at the crack sites.

## 5.5 EVOLUTION OF STRESSES IN $\alpha$ -Al<sub>2</sub>O<sub>3</sub>, $\delta$ -Ru AND RuO<sub>2</sub> DURING OXIDATION IN AIR AT 1100 °C

As described in section 4.3, analyzing the elliptical distortion of the Debye-Scherrer rings, it is possible to calculate the in-plane stresses of the different phases ( $\alpha$ -Al<sub>2</sub>O<sub>3</sub>,  $\delta$ -Ru, RuO<sub>2</sub>) formed during the oxidation. The following results refer to the sample oxidized at the Argonne National Laboratory's synchrotron; the diffraction intensities belonging to this experiment have been previously reported (section 5.2).

In Fig. 5.31a the in-plane stress of  $\alpha$ -Al<sub>2</sub>O<sub>3</sub> is obtained from (116), (024) and (012) reflections. The (012), the smallest ring, is often the least reliable, which seems to be the case also for these measurements. The stresses are always compressive. The largest stresses developed during early stage oxidation. More commonly, for other alloys forming alumina during oxidation at temperatures higher than 900 °C, it is observed an initial large tensile stress (up to 1 GPa) [Hou04]. This results from the  $\theta$ - to  $\alpha$ -phase transformation of the early oxide. The difference between the specific volumes of the two phases induces the  $\alpha$ -phase to shrink during transformation and to be consequently under tension [Tol00]. Therefore, the initial compressive state suggests that no transition aluminas are formed on this material at the initial oxidation stage.

The residual stress ( $\sim$  1 GPa), which develops during cooling, is relatively small compared to other alloys, which are used as BCs [Hou04]. In fact, as mentioned before, the thermal expansion coefficients (CTE) of  $\alpha$ -Al<sub>2</sub>O<sub>3</sub> and RuAl are relatively comparable.

There is no evidence of debonding during cooling, in fact no abrupt changes attributable to sudden strain relief are observed. Also, the cooling was rather slow (300 °C/h), so some strain relief might be accomplished at higher temperatures by creep in the oxide.

In Fig. 5.31b the in-plane stress of  $\delta$ -Ru is obtained from (100) and (102) rings; at the initial state the (102) ring indicates tension, while the (100) indicates compression. The stress intensities in both cases appear to decrease during oxidation. This behaviour might suggest that the stresses have an orientation-dependence. This hypothesis is also supported by the fact that the signals for the two rings behave differently during the oxidation, suggesting that different orientation suffer a different stress-evolution.

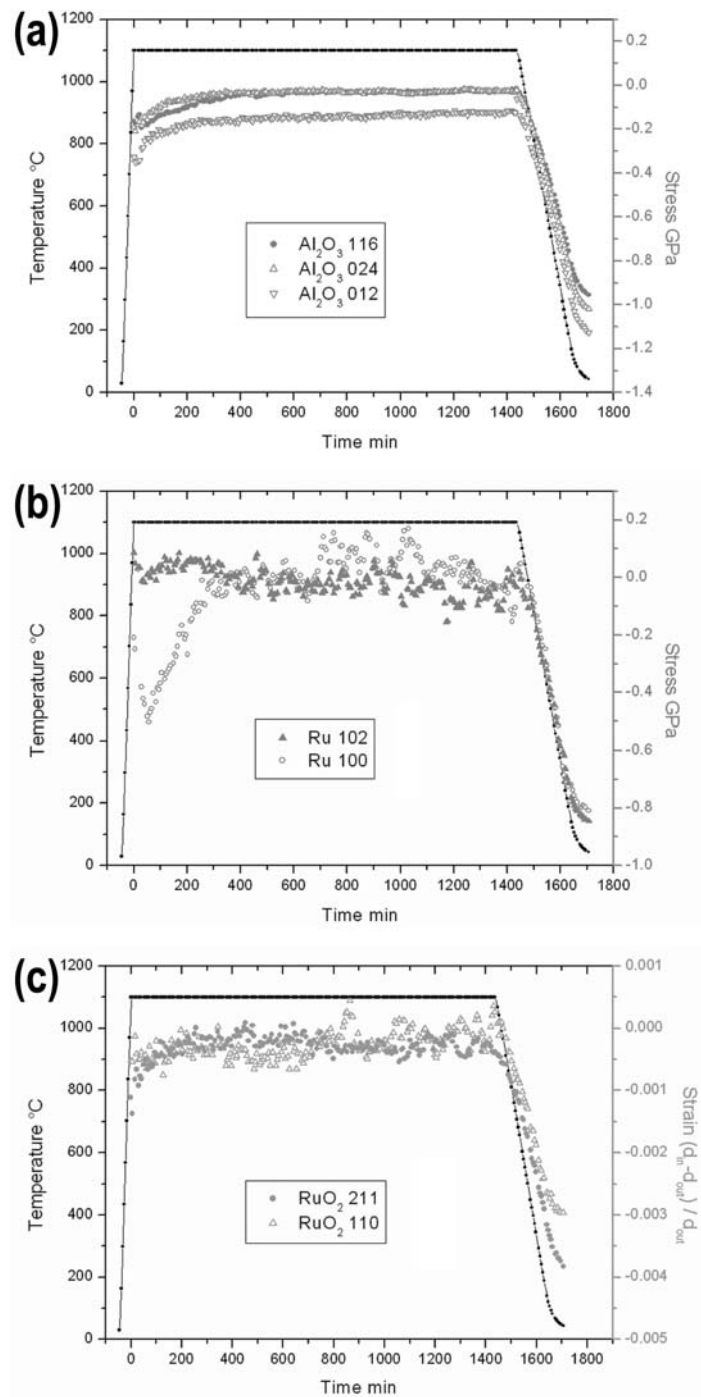


Fig. 5.31 Evolution of the stresses measured in-situ, during oxidation in static air at 1100 °C of a polished RuAl sample; heating rate 1000 °C/h, cooling rate 300 °C/h. a) (116), (024) and (012)  $\alpha$ - $\text{Al}_2\text{O}_3$ ; b) (102) and (100)  $\delta$ -Ru; c) (211) and (110)  $\text{RuO}_2$ . The stresses have been calculated by analyzing the elliptical distortion of the Debye-Scherrer rings, which have been acquired at Argonne National Lab. Synchrotron.

It must also be noticed that the residual stresses in Ru after cooling are about the same as the stresses in  $\alpha\text{-Al}_2\text{O}_3$ .

In Fig. 5.31c the strain in  $\text{RuO}_2$  is obtained from two rings. During the oxidation, the strain indicates always a compression state, which increases during cooling as observed also for  $\text{Al}_2\text{O}_3$  and Ru.

## 6. DISCUSSION

### 6.1 MORPHOLOGY OF THE TGO AND SUBSTRATE

Fig. 6.1 shows schematically the microstructure of RuAl after oxidation and the techniques used for the investigations. In the following, the TGO and some of the main fundamental science themes related to its formation are discussed. Additionally, some more specific features, related to the role of Ru, are also addressed.

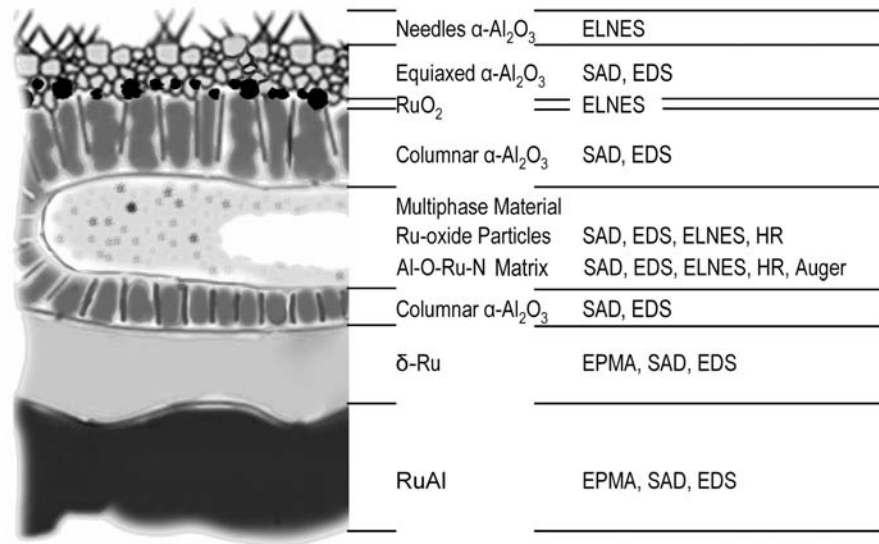


Fig. 6.1 Schematic representation of a TGO formed on a RuAl sample after oxidation in air at 1100 °C.

#### **Direct establishment of $\alpha$ - $\text{Al}_2\text{O}_3$ in the TGO**

As already mentioned, crystalline transient alumina was never detected on RuAl oxidized samples. Neither the oxidation at 950 °C, nor the in-situ investigation, during which the sample was heated from RT to 1100 °C, did indicate the presence of meta-stable phases. This represents an excellent quality for a potential BC, which should prevent failure due to phase transformation of the TGO. In fact, rapid establishment of stable  $\alpha$ - $\text{Al}_2\text{O}_3$  on single-phase  $\beta$ -structure is a challenge, which is being usually addressed by careful

surface preparation [Tol00] or doping with elements that promote the nucleation of the  $\alpha$ -phase, e.g. Cr or Fe [Bye74].

In particular, Cr and Fe are adopted because the early formation of  $\text{Cr}_2\text{O}_3$  or  $\text{Fe}_2\text{O}_3$  nucleus, whose crystalline structure is similar to  $\alpha\text{-Al}_2\text{O}_3$ , is generally believed to enhance the formation and growth of  $\alpha\text{-Al}_2\text{O}_3$ . A similar mechanism is believed to occur in the oxidation of RuAl. It is suggested that RuAl, which possess a  $\beta$ -phase as (Ni,Pt)Al, forms rapidly  $\alpha\text{-Al}_2\text{O}_3$  because of the early formation of the  $\delta$ -Ru phase. In fact,  $\delta$ -Ru phase has a hexagonal structure, which may promote the direct formation of  $\alpha\text{-Al}_2\text{O}_3$ .

### **$\alpha\text{-Al}_2\text{O}_3$ needles**

Alumina needles were observed on the surface of the oxidized RuAl samples. It is known that whisker-type features were detected also in the oxidation of other metals such as iron [Tal67] and copper [Fis63]. After electron diffraction investigations, it was suggested that a dislocation pipe runs along the growth direction. The morphology of these features, projecting outwards from the oxide surface, has suggested a growth mechanism based on cationic transport, either by lattice or surface diffusion.

Filamentary protrusions of alumina polymorphs (including  $\alpha$ -phase) have been observed as well at temperatures above 1100 °C at the gas-scale interface of several alumina-former alloys, such as iron-based [Tie72] and nickel-based [Hin80].

Similar features were observed also at lower temperatures (between 900 and 1000 °C) on Ni-Al and Fe-Al systems. In this case the formation of needles was associated to the fast-growing transition phase  $\theta\text{-Al}_2\text{O}_3$  [Pin95, Yan98, Ryb89].

The fact that on RuAl no transient  $\text{Al}_2\text{O}_3$  has been detected, suggested that the needles were  $\alpha\text{-Al}_2\text{O}_3$ . This was then confirmed by EELS investigation, which has shown undoubtedly the energy loss near edge structure of the  $\alpha$ -phase (Fig. 5.14).

Also the possibility that these needles grow as transient alumina prior to transforming to  $\alpha$ -phase is very improbable. In fact, crystalline polymorphs different than  $\alpha$ -phase were not detected even at lower temperatures (950 °C), at which transient alumina phases are normally observed on Ni-Al [Bru92].

Based on these observations, it can be concluded that this particular alumina morphology can nucleate and grow directly as  $\alpha$ -phase on the RuAl alloy.



### **Growth of the TGO based on inward and outward diffusion**

The TGO, formed after oxidation at 1100 °C on RuAl specimens, presents equiaxed grains at the surface and columnar grains next to the substrate. Both the equiaxed and columnar grains have shown to grow during oxidation. This type of morphology has already been observed upon oxidation at high temperature on different alloy systems, such as: (Ni,Pt)Al [Bri00, Tol01], NiCrAlY [Lev03], CoCrAl [Hin82].

It is commonly assumed that the oxidation mechanism is based on the counter diffusion of Al (outward) and O (inward) at the grain boundaries [Pin96, Sch96], which are known to act as diffusion path across the oxide scale [Kin76, Cla03]. The outward diffusion of Al is believed to enhance the formation of the equiaxed morphology, while the inward diffusion of O the columnar. Therefore, a TGO will present a columnar or an equiaxed morphology, depending on which is the dominating diffusion mechanism.

There are two main observations in the oxidation of RuAl that confirm this theory.

The first (i) is that no crystallographic texture has been observed by XRD, indicating that the grains are randomly oriented. Thus, the absence of a fiber texture suggests that the columnar morphology can be only a consequence of the inward growth of the grains.

The second (ii) is that the enrichment or Ru-rich precipitates at the border between the equiaxed and the columnar zones. In fact, these precipitates form at the very beginning of the oxidation when the substrate is not yet covered with a protective oxide layer and RuAl is directly in contact with the oxidizing atmosphere. Therefore, these Ru-rich precipitates indicate the position of the surface of the sample prior to oxidation, proving the outward diffusion origin of the equiaxed grains and the inward diffusion origin of the columnar grains.

### **Role of the multiphase material**

The multiphase material detected within the cavities is composed of nano-particles embedded in a Ru-Al-O-N amorphous matrix. The particles are composed of Ru and O, and show a hexagonal crystalline structure, which is characteristic of the  $\delta$ -Ru phase.

The in-situ TEM investigation, conducted at high temperatures, showed that the particles dissolved in the matrix at temperatures higher than 800 °C. It was suggested (par. 5.2)

that the origin of these particles is caused by a temperature dependence of the solubility of Ru in the Ru-Al-O-N phase.

This behaviour suggests that at the oxidation temperature (1100 °C) the amorphous Ru-Al-O-N phase, which to the authors' knowledge was never reported in literature, forms and coexists with the  $\alpha$ -Al<sub>2</sub>O<sub>3</sub> in the TGO.

It is believed that the multiphase material is the outcome of the oxidation of the  $\delta$ -Ru phase. Based on the different behaviour that RuAl showed during oxidation in O<sub>2</sub> plus Ar and oxidation in air, it is suggested that N has a crucial role contributing to the stability of the Ru-Al-O-N phase. Enhancing the stability of this phase, N is believed to strongly reduce the evaporation rate of the gaseous Ru-oxides. It must be mentioned indeed that the amount of cavities produced during 50 h oxidation in O<sub>2</sub> was similar to the one produced after 500 h oxidation in air. This observation suggests that the effect of N decreases approximately by one order of magnitude the consumption of Ru.

### **The Metallic Substrate**

After oxidation acicular precipitates of Ru were detected in the RuAl substrate. Additionally, electron diffraction and HREM presented a superstructure of the RuAl substrate next to the  $\delta$ -Ru layer.

The presence of Ru precipitates in RuAl has already been reported. Fleischer and coauthors [Fle91] already detected these particular precipitates in annealed RuAl samples (annealing conditions: 1350 °C for 20 h), and an orientation relationship between them and the matrix was found. The precipitates have been described with a roughly square cross section, having one of the facets parallel to the (110)/(0001) planes of the matrix and precipitate, respectively. The other facet did not lie on a high index plane, but was close to the (3 $\bar{3}$ 4) plane of the matrix. The rod axis for the acicular precipitate has been indicated approximately to be [ $\bar{2}$ 32]. Dislocations were also observed, running along the length of the precipitates on the precipitate/matrix interface.

The superstructure detected by electron diffraction and HREM is suggested to be caused by the presence of Al vacancies.

The HREM micrograph (Fig. 5.13) presented a contrast, which has been addressed as a compositional modulation. It is believed that the compositional modulation is indeed a

self rearrangement of the Al vacancies in the RuAl. This rearrangement of vacancies confers to the crystal structure a displacive modulation, which has been observed in the electron diffraction pattern.

Similar diffraction patterns have been already reported in literature. Van Tendeloo and coauthors, for example, found similar features investigating the Bi-Sr-Cu-O superconductor system [Van88]. In their study it was shown that the observed modulation was incommensurate, which is the case when the modulation period cannot be related to the base underlying lattice through a rational number. In the case of the modulation observed on RuAl, the modulation wave vectors ( $\bar{q}_1$  and  $\bar{q}_2$ ) have been measured to be  $\sim 1/10$  of the  $\{011\}$  and  $\{112\}$ , respectively (Fig. 5.12). Due to the approximation of the measurement, however, further investigations are needed in order to establish the nature of this modulation.

The acicular Ru precipitates and the compositional-displacive modulations are considered to be a clear proof of the existence of an orientation dependence of the Al vacancies in the RuAl alloy. Such features, which as in the case of the acicular precipitates can already be present after annealing, are believed to be enhanced during oxidation due to the Al depletion. Therefore, there might be an influence of the orientation of the RuAl substrate upon oxidation, which so far has not been investigated.

## 6.2 EVOLUTION OF STRESSES DURING OXIDATION

The formation of stresses in the TGO is a scientific theme, which has been largely investigated. In fact, as already mentioned, the thermally grown alumina is the origin of the major strain incompatibility, which induces failure in TBC systems.

In order to predict the evolution of the stresses during oxidation, Clarke [Cla03] developed a model for the lateral strain rate accompanying the growth of an oxide. This model is based on trapping of counter-diffusing cations and anions at core of edge dislocations causing them to climb through the oxide thickness. The model predicts that “in the absence of any stress relaxation, the lateral growth strain rate is proportional to the thickening rate of the oxide and the average grain boundary mis-orientation but inversely to the average grain size of the oxide”.

The measurements conducted during oxidation on the RuAl samples showed that the stress in the  $\alpha$ -Al<sub>2</sub>O<sub>3</sub> is compressive at all times, with the largest stress appearing in early oxidation. This is in agreement with the fact that no transition aluminas have been observed. In fact, for alumina-formers at 1100 °C, a large tensile stress is commonly seen, which results from the  $\theta$  to  $\alpha$  phase conversion of the initial oxide [Hou04]. Therefore, despite the fact that the oxide thickness grows due to inward and outward diffusion, as previously observed, the stresses diminish to approximately 50 MPa and remain constant after the initial high compression state.

The progress of the stresses, observed on RuAl, suggested then that there was indeed a noticeable stress relaxation by creep occurring in the oxide during oxidation at 1100 °C. A mechanism of stress relaxation during high-temperature oxidation of other alumina-former alloys has already been proposed by Hou and coauthors [Hou04] after XRD in-situ investigations.

The residual stress, which develops during cooling in the oxide scale grown on RuAl, is relatively small compared to other alumina-former alloys. In fact, as mentioned, the thermal expansion coefficients (CTE) of  $\alpha$ -Al<sub>2</sub>O<sub>3</sub> and RuAl are relatively comparable. This represents a promising property for a potential BC, which should undergo many thermal cycles.

The in-plane stresses, calculated for the  $\delta$ -Ru phase, are obtained for two different orientations. The measured stresses behave differently during the oxidation, suggesting that the stresses might have an orientation-dependence. It must be taken into account that the  $\delta$ -Ru phase has an hexagonal crystal structure, which does not behave isotropically upon strain. Therefore, if there is an orientation relation between the RuAl substrate and the nucleated  $\delta$ -Ru phase, it can happen that the in-plane stresses may provoke cracks in the  $\delta$ -Ru layer on specific orientations of the RuAl grains more than on others.

### **6.3 OXIDATION PROGRESS**

The TGA conducted in O<sub>2</sub> plus Ar and in air showed clear differences, which are schematically summarized in Fig. 6.2. The oxidation in air is characterized by an overall gain of weight, while the oxidation in O<sub>2</sub> plus Ar by an overall loss of weight.

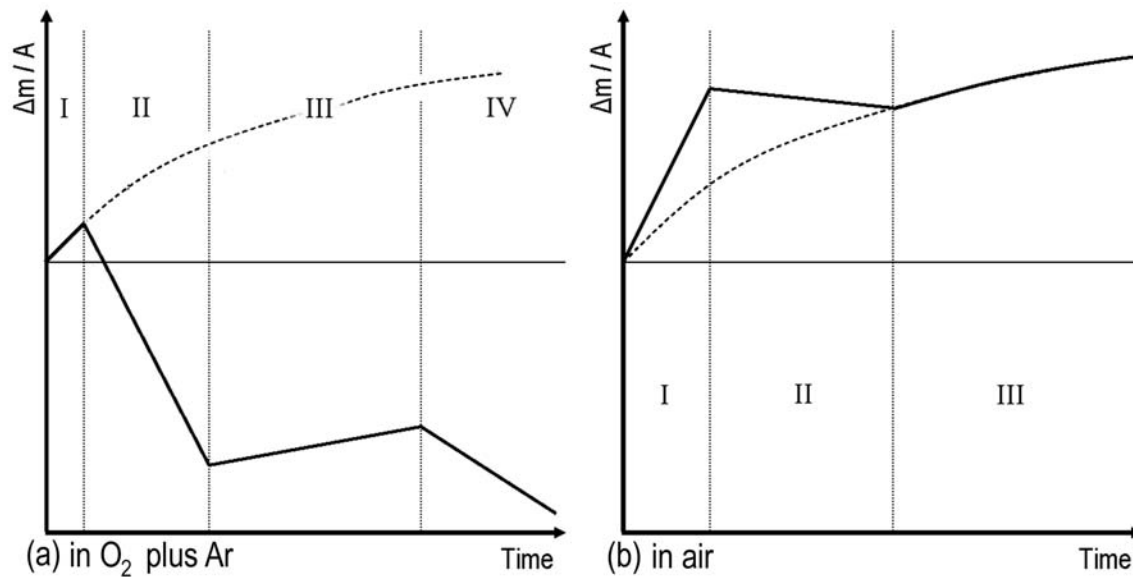


Fig. 6.2 Schematic illustration of the weight change of a RuAl sample during oxidation (a) in  $O_2$  plus Ar and (b) in air.

Even if the general trends in these two oxidizing atmospheres are very different, there are some similarities in the kinetics evolution. As it can be seen from the weight-change curves, both the oxidation processes can be divided in different stages of gaining and losing weight.

The two different oxidizing atmospheres present the same sequence of stages, which differ only for duration and intensity of the weight variation. As mentioned previously, the cause of this difference has been attributed to the effect of N on the stability of the mixed oxide based on Ru and Al.

### **Initial Stage**

At the very beginning, when the RuAl sample is exposed to the high temperature, both Ru-oxides and  $Al_2O_3$  form, because the oxygen partial pressure at the sample's surface is higher than the equilibrium partial pressures of the oxides. But  $Al_2O_3$  is preferentially oxidized due to its higher thermodynamic stability.

The favorite formation of  $\text{Al}_2\text{O}_3$  compared to Ru-oxides leads to the formation of an aluminum depleted layer in the subsurface zone. Due to the very narrow stoichiometry window of RuAl alloy (Fig. 3.6), the Al depleted zone transforms to  $\delta$ -Ru.

The  $\delta$ -Ru layer is situated between the oxide scale and the RuAl substrate, and acts as a diffusion barrier because of the low solubility of Al and O in it.

In air at 1100 °C the rate of the weight loss of Ru, estimated from Jehn [Jeh84] ( $\sim 3 \text{ mg/cm}^2\cdot\text{h}$ ), is one order of magnitude bigger than the rate of the oxide growth at the beginning of the oxidation ( $\sim 0.1 \text{ mg/cm}^2\cdot\text{h}$ , data referring to oxidation in low  $P_{\text{O}_2}$  plus Ar). Therefore the gain of weight measured during the initial stage of the experiment, when the bare RuAl was exposed to the oxidizing atmosphere, suggested that the gaseous  $\text{RuO}_3$  and  $\text{RuO}_4$  do not form instantaneously from the RuAl phase. They form only afterwards from the  $\delta$ -Ru phase.

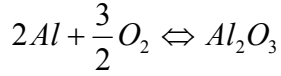
### **Loss of weight**

The thermogravimetric investigations suggests that the oxidation of Al and the oxidation of Ru, with the consequent evaporation of  $\text{RuO}_3$  and  $\text{RuO}_4$ , proceed simultaneously. In fact, when the  $P_{\text{O}_2}$  has been increased, the plot of the mass-change reacted instantaneously, proving the concurrency of these events.

The instantaneous reaction to the variation of  $P_{\text{O}_2}$  refutes the existence of a continuous and dense  $\alpha$ - $\text{Al}_2\text{O}_3$  scale that should indeed forbid the evaporation of  $\text{RuO}_3$  and  $\text{RuO}_4$  from the underlying  $\delta$ -Ru. In fact, it can be seen from the vapour phase diagram (Fig. 3.7) that the gaseous species of Ru-oxide ( $\text{RuO}_3$  and  $\text{RuO}_4$ ) have a pressure smaller than 1 atm. Therefore, no evaporation of gaseous Ru-oxides is expected after a closed and dense scale is formed.

Another important thermodynamic consideration is that the formation of solid  $\text{RuO}_2$  beneath a continuous and dense  $\alpha$ - $\text{Al}_2\text{O}_3$  scale is also unexpected, if  $\text{RuO}_2$  and  $\text{Al}_2\text{O}_3$  are assumed to be the only stable oxides at 1100 °C. In fact, even if we assume that beneath a dense alumina scale the  $P_{\text{O}_2}$  is about  $10^{-3}$  atm, which is necessary to form  $\text{RuO}_2$  (see Fig. 3.7), the Al activity should be lower than  $2.08 \cdot 10^{-21}$  to permit the formation of solid Ru-

oxide and/or to establish high vapour pressures of the volatile Ru-oxides. As it can be calculated, ( $\log K_f$  at 1100 °C can be extrapolated from the literature [Bar89]),



$$\log K (= 45.86 \text{ KJ} / \text{mol}) = \log a_{Al_2O_3} - 2 \log a_{Al} - \frac{3}{2} \log P_{O_2} \quad (6.1).$$

$$a_{Al} = 2.08 \cdot 10^{-21} \text{ KJ} / \text{mol}$$

Such an aluminum activity corresponds to a concentration of Al in the  $\delta$ -Ru phase that is far too low to be considered feasible at these experimental conditions. Thus the oxidation of Ru is not feasible to happen by oxygen diffusion through a compact oxide scale.

Therefore, there are clear indications of the presence of favorite paths through the oxide scale that allow the oxidation of the  $\delta$ -Ru and the evaporation of its gaseous oxides. These favorite paths can either be cracks across the oxide scale or a second phase containing Ru and wetting the  $\alpha$ - $Al_2O_3$  grain boundaries.

An indication of the evaporation rate of the gaseous Ru-oxides may be offered by the variation of the  $RuO_2$  signal during in-situ XRD. This signal offers good indications regarding the progress of the oxidation, because the  $RuO_2$  formation is related to (i) the oxidation of the  $\delta$ -Ru layer, (ii) the formation of the multiphase material and consequently (iii) to the evaporation of the gaseous Ru-oxides.

While the growth of  $Al_2O_3$  results parabolic during all the high temperature exposition, the Ru and  $RuO_2$  signals present a discontinuous behaviour.

The interpretation of the results suggests that the multiphase material forms in air already during the heating up of the specimen. After an initial period during which it grows linearly, the signal of  $RuO_2$  becomes constant. This indicates that the evaporation of the gaseous Ru-oxides stops or becomes constant. In fact also the TGA conducted in conditions similar to the synchrotron experiment evidenced that after the initial period, during which a consistent gain of weight is measured, the behaviour becomes parabolic (Fig. 6.2).

So it seems that after an instable initial period of oxidation (stages I and II) the reactions taking place find an equilibrium in which the formation of  $\alpha\text{-Al}_2\text{O}_3$  represents the main aspect.

### **Alternation of gaining and loosing weight periods (Cavities Formation)**

During the early stages of oxidation the microstructure of the scale is already well defined, showing the  $\delta\text{-Ru}$  and the  $\alpha\text{-Al}_2\text{O}_3$  layers. As previously explained, the  $\delta\text{-Ru}$  layer acts as a diffusion barrier for aluminum to migrate from the substrate to the oxide scale and consequently renders the interface between the oxide and the metallic Ru unstable. In fact any inward protuberance of the interface shortens the diffusion distance, resulting in a favorite growing site.

The wavy oxide/ $\delta\text{-Ru}$  interface and the stresses, formed due to the lateral growth of the oxide [Hin82, Cla03] and the  $\delta\text{-Ru}$  formation, are supposed to enhance the formation of cracks in the  $\delta\text{-Ru}$  layer, in particular at the sites where the layer is thinner and the stresses are consequently higher. The cracks in the  $\delta\text{-Ru}$  layer act as free paths for oxygen to diffuse and to grow oxides (Fig. 6.3a), as suggested by the direction of the alumina columns, which are perpendicular to the  $\delta\text{-Ru}$  phase. This mechanism represents the way by which oxygen can pass through, creating a multilayered morphology. A similar mechanism has been suggested also in the case of the oxidation of  $\text{NbAl}_3$  [Mei89].

It is believed that the growth of the “oxide bridges” (see Fig. 6.3a) across the  $\delta\text{-Ru}$  layer develops locally stresses in the oxide top scale which enhance cracking.

In fact the formation of the “oxide bridges” renders the oxide layer wavy, and it is known that the out-of-plane stresses of the TGO on convex surfaces can be much higher than on flat surfaces [Reb03]. This explains why a more severe multilayered morphology has been observed at edges and corners.

When the embedded  $\delta\text{-Ru}$  is isolated from the substrate, the activity of Al in it is supposed to decrease in time until the point at which the oxidation of the metallic Ru begins. Then the Ru-oxides find their way out through grain boundaries or micro-cracks in the  $\alpha\text{-Al}_2\text{O}_3$  scale (Fig. 6.3b).

At this point the cracked and porous scale is no longer protective and the mechanism for the formation of the cavity can start again (Fig. 6.3c).



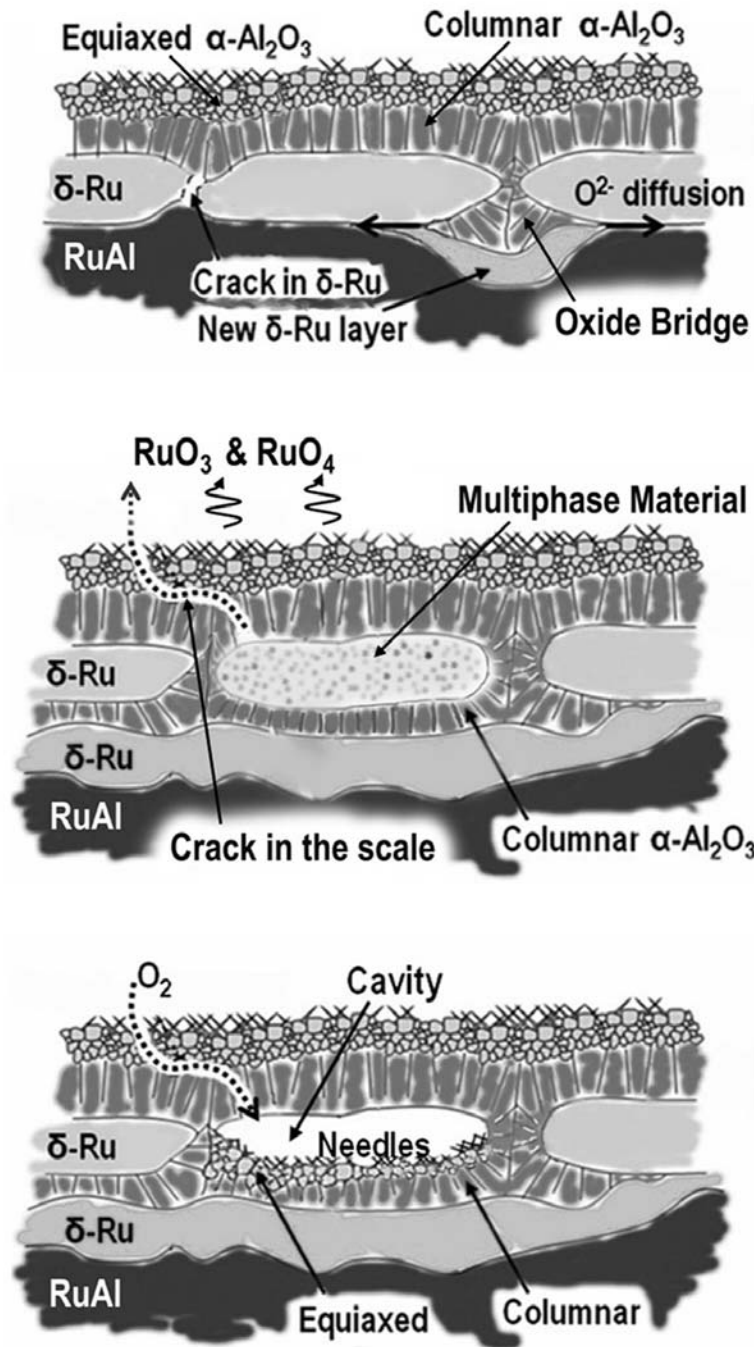


Fig. 6.3 Proposed mechanism for the formation of cavities during the oxidation of RuAl.  
 (a) instability of the  $\alpha\text{-Al}_2\text{O}_3/\delta\text{-Ru}$  interface, formation of cracks and oxide bridges in the  $\delta\text{-Ru}$  layer.  
 (b) the embedded  $\delta\text{-Ru}$  oxidizes, and gaseous Ru-oxides evaporate through grain boundaries and cracks.  
 (c) the cracked scale is no longer protective and the cavity formation mechanism re-starts.

This mechanism of formation of the discontinuous  $\text{Al}_2\text{O}_3$  layer is different from the one that Chou proposed for the oxidation of IrAl alloys [Cho90], previously described in par. 3.3.1. Chou suggested that the discontinuity in the  $\text{Al}_2\text{O}_3$  layer were caused by Al and O diffusion fluxes through the Ir-rich layer, which in the RuAl case is represented by the  $\delta$ -Ru layer. The nucleation and growth of  $\text{Al}_2\text{O}_3$  is not expected to occur in the Ir-rich layer because of the low concentrations of both Al and O; but at the Ir-rich/IrAl interface where the Al's activity is big enough to react with the diffusing oxygen.

If such a mechanism really occurs, some oxide areas totally embedded in the Al-depleted metal (Ir or Ru) should be visible. This feature should be the result of the nucleation of "new" oxide at the Ru/RuAl (Ir-rich/IrAl) interface. In fact, the nucleation of the oxide at the interface with the substrate would instantaneously be accompanied by a depletion of Al in the areas of the substrate next to the "new" oxide itself. Consequently, this depletion of Al would lead to the formation of "new" Al-depleted metal (Ir or Ru), surrounding the oxide. This is not the case of RuAl, where the different layers of oxide are always interconnected.

## 7. CONCLUSIONS

The RuAl has been analyzed as an alternative BC due to its good mechanical properties and its similar thermal expansion coefficient to  $\alpha$ -Al<sub>2</sub>O<sub>3</sub>. The isothermal oxidation of RuAl binary alloy, prepared by arc-melting and induction melting, has been studied at 1100 °C in different atmospheres.

During oxidation an  $\alpha$ -Al<sub>2</sub>O<sub>3</sub> layer grows over a  $\delta$ -Ru layer formed by the depletion of Al in the RuAl substrate. Transient alumina has never been detected neither after very short oxidation times.

The morphology of the oxide shows needles and equiaxed  $\alpha$ -Al<sub>2</sub>O<sub>3</sub> grains at the surface, and columnar  $\alpha$ -Al<sub>2</sub>O<sub>3</sub> grains next to the substrate. The oxidation mechanism is based on a combination of inward diffusion of O and outward diffusion of Al.

Thermogravimetric measurements conducted during oxidation showed an alternation of gaining and losing weight periods, where the weight loss has been attributed to the evaporation of the gaseous Ru-oxides from the  $\delta$ -Ru phase.

The  $\alpha$ -Al<sub>2</sub>O<sub>3</sub> top scale did not grow dense and continuous because the oxidation of Ru and the evaporation of RuO<sub>3</sub> and RuO<sub>4</sub> through the oxide formed large cavities.

The gaseous Ru-oxides evaporate through (i) cracks in the alumina scale and/or (ii) through a second phase rich in Ru decorating the  $\alpha$ -Al<sub>2</sub>O<sub>3</sub> grain boundaries.

A mechanism for the formation of the layered structure and the cavities has been proposed, which suggests that the formation of a second layer of alumina is initiated by the cracking of the  $\delta$ -Ru layer. These cracks offer a favorite site to the alumina to grow and embed areas of the  $\delta$ -Ru layer, which may afterwards evaporate as gaseous oxide creating the cavities.

It was observed that the stresses in the oxide were not so intense to justify the cracking. But, it is believed that the growth of the  $\alpha$ -Al<sub>2</sub>O<sub>3</sub> through the  $\delta$ -Ru layer develops out-of-plane stresses in the oxide, which are the cause of cracking.

The weight loss showed to be much more severe in the oxygen plus argon environment compared to the oxidation in air.

It has been proposed that the presence of nitrogen in the oxidizing atmosphere enhances the formation of an amorphous oxy-nitride containing Ru and Al. This material is believed to strongly reduce the evaporation rate of RuO<sub>3</sub> and RuO<sub>4</sub>; in fact the amount of

cavities, which is visible after 50 h oxidation in oxygen plus argon, is similar to the amount of cavities detected after 500 h oxidation in air.

In conclusion, it appears that the formation of the  $\delta$ -Ru layer beneath the oxide scale is detrimental for the formation of a protective TGO on polycrystalline RuAl, because the evaporation of RuO<sub>3</sub> and RuO<sub>4</sub> does not allow a compact oxide to form.

Based on these conclusions, it is suggested that to exploit the outstanding mechanical properties of Ru-aluminide alloys, two routes may be investigated.

The first route is to investigate the orientation influence of the substrate. The reasons to conduct such investigation are based on three observations. (i) The multilayer morphology has not been detected all over the sample. Large areas presented only a single couple of layers  $\alpha$ -Al<sub>2</sub>O<sub>3</sub>/ $\delta$ -Ru even after 500 h oxidation, proving a good stability. (ii)  $\delta$ -Ru phase has a hexagonal crystal structure, which does not behave isotropically upon strain. Therefore, if there is an orientation relation between the RuAl substrate and the nucleated  $\delta$ -Ru phase, it can happen that the in-plane stresses may provoke cracks in the  $\delta$ -Ru layer on specific orientations of the RuAl grains more than on others. (iii) Acicular Ru precipitates and Al vacancies presented an orientation-dependence in the RuAl substrate. Therefore a specific orientation of the RuAl substrate might be found, which minimizes the cracking of the  $\delta$ -Ru layer.

The second route is to try to avoid the formation of the  $\delta$ -Ru phase. This effect may be reached by finding alloying elements which renders the Ru-Al B2 structure more stable in case of depletion of Al.

## REFERENCES:

- [Ahn04] C.C Ahn: Trans elect en loss spectr in mat sci & EELS atlas. (VCH, Weinheim, Germany, 2004).
- [Bar89] I. Barin: Thermochemical Data of Pure Substances. (VCH, Weinheim, Germany, 1989).
- [Bir83] N. Birks, G.H. Meier: Introd. to High Temp. Oxid. of Metals, 1st ed. (Edward Arnold, London, England, 1983).
- [Bri00] M.R. Brickey, J.L. Lee: Structural and chemical analyses of a thermally grown oxide scale in thermal barrier coatings containing a platinum-nickel aluminide bondcoat. *Oxid. Met.* **54**, 237 (2000).
- [Bor99] M. Born, E. Wolf: Principles of optics. Cambridge University Press, 7<sup>th</sup> edition (1999).
- [Bou03] D. Bouchet, C. Colliex: Experimental study of ELNES at grain boundaries in alumina: intergranular radiation damage effect on Al-L<sub>23</sub> and O-K edges. *Ultramicroscopy*, **96**, 139 (2003).
- [Bra99] D. Brandon, W.D. Kaplan. Microstructural characterization of materials. Wiley (1999).
- [Bru92] M.W. Brumm, H.J. Grabke: The oxidation behaviour of NiAl-1. Phase transformations in the alumina scale during oxidation of NiAl and NiAl-Cr alloys. *Corr. Sci.* **33**, 1677 (1992).
- [But03] H.J. Butt. Physics and chemistry of interfaces, Wiley-VCH GmbH&Co.KGAA (2003).

- [Bye74] G.C. Bye, G.T. Simpkin: Influence of Cr and Fe on the formation of  $\alpha$ -Al<sub>2</sub>O<sub>3</sub> from  $\gamma$ -Al<sub>2</sub>O<sub>3</sub>. *J. Am. Ceram. Soc.* **57**, 367 (1974).
- [Car05] J.M. Cairney, P.R. Munroe, M. Hoffman: The application of focused ion beam technology to the characterization of coatings. *Surf. Coat. Tech.*, **198**, 165 (2005).
- [Cha86] S. Chakravorty, D.R.F. West: The constitution of the Ni-Al-u system. *J. Mater. Sci.* **21**, 2721 (1986).
- [Cho90] T.C. Chou: The formation of discontinuous Al<sub>2</sub>O<sub>3</sub> layers during high temperature oxidation of IrAl alloys. *J. Mater. Res.* **5**, 378 (1990).
- [Cla03a] D.R. Clarke: The lateral growth strain accompanying the formation of thermally grown oxide. *Acta Mat.* **51**, 1393 (2003).
- [Cla03b] D.R. Clarke, C.G. Levi: Materials design for the next generation thermal barrier coatings. *Annu. Rev. Mater. Res.* **33**, 383 (2003).
- [DeG03] M. De Graef: Introduction to conventional transmission electron microscopy. Cambridge University Press, 1<sup>th</sup> edition (2003).
- [Fis63] H. Fischmeister: Mechanism and kinetic effects of particulate oxide growth. I. Whiskers. *Collo. Intern. Centre Natl. Tech. Sci.* **112**, 211 (1963).
- [Fle91] R.L. Fleischer, R.D. Field, C.L. Briant: Mechanical-properties of high temperature alloys of AlRu. *Metall Trans. A.* **22**, 403 (1991).
- [Fle93] R.L. Fleischer, D.W. McKee: Mechanical and oxidation properties of AlRu-based high temperature alloys. *Metall Trans A.* **24**, 759 (1993).
- [Gol58] V.M. Goldschmidt: Geochemische Verteilungsgesetze vol. VI, measurements by W.H. Zachariasen; quoted by W.B. Pearson: A handbook of lattice spacings and

- structures of metals and alloys. P. 1026, Pergamon Press, New York, USA (1958).
- [Goo01] P.J. Goodhew, J. Humphreys, R. Beanland: Electron microscopy and analysis. Taylor & Francis, London, UK (2001).
- [Gra91] H.J. Grabke, D. Wiemer, H. Viehhaus: Segregation of sulfur during growth of oxide scales. *Appl. Sur. Sci.* **47 (3)**, 243 (1991).
- [Hin80] H.M. Hindam, W.W. Smeltzer: Growth and microstructure of  $\alpha$ -Al<sub>2</sub>O<sub>3</sub> on  $\beta$ -NiAl. *J. Electrochem. Soc.* **127(7)**, 1630 (1980).
- [Hin82] H. Hindam, D.P. Whittle: Microstructure, adhesion and growth-kinetics of protective scales on metals and alloys. *Oxid. Met.* **18**, 245 (1982).
- [Hou04] P.Y. Hou, A.P. Paulikas, B.W. Veal: Growth strains and stress relaxation in alumina scales during high temperature oxidation. *6<sup>th</sup> Symposium on High Temp. Corr. And Protection of Materials*: Les Embiez, France (2004).
- [Hut00] J.W. Hutchinson, A.G. Evans: The influence of imperfections on the nucleation and propagation of buckling driven delamination. *J. Mech. Phys. Solids.* **48**, 709 (2000).
- [Jeh84] H. Jehn: High temperature behaviour of platinum group metals in oxidizing atmospheres. *J. of Less Common Metals.* **100**, 321 (1984).
- [Kin76] W.D. Kingery, H.K. Bowen, D.R. Uhlmann: *Introd. to Ceram.* (J Wiley & Sons, New York, USA, 1976).
- [Lan97] C. Lang, M. Schütze: The initial stages in the oxidation of TiAl, in *Oxidation of Intermetallics*, edited by H.J. Grabke, M. Schütze (Wiley-VCH, Weinheim, Germany, 1997), p. 245.

- [Lee85] W.E. Lee, K.P.D. Lagerlof: Structural and Diffraction Data of Sapphire ( $\alpha$ - $\text{Al}_2\text{O}_3$ ). *J. Elec. Micr. Tech.* **2**, 247 (1985).
- [Lev98] I. Levin, D. Brandon: Metastable alumina polymorphs: crystal structures and transition sequences. *J. Am. Ceram. Soc.* **81**, 1995 (1998).
- [Lev03] C.G. Levi, E. Sommer, S.G. Terry, A. Catanoiu, M. Rühle: Alumina grown during deposition of thermal barrier coatings on NiCrAlY. *J. Am. Ceram. Soc.* **86**, 676 (2003).
- [Lev04] C.G. Levi: Emerging materials and processes for thermal barrier systems. *Curr. Opin. Sol. St. & Mat. Sci.* **8**, 77 (2004).
- [LuD99] D.C. Lu, T.M. Pollock: Low temperature deformation and dislocation substructure of ruthenium aluminide polycrystals. *Acta Mat.* **47**, 1035 (1999).
- [Mei89] G.H. Meier: Fundamentals of the oxidation of high-temperature intermetallics, in *Oxidation of High-Temperature Intermetallics*, edited by T. Grobstein and J. Doychak (workshop on the oxidation of high-temperature intermetallics, Cleveland 1988), p. 1.
- [Mil84] R.A. Miller: Oxidation-based model for thermal barrier coating life. *J. Am. Ceram. Soc.* **67**, 517 (1984).
- [Mil87] R.A. Miller: Thermal barrier coatings for aircraft engines: history and directions. *J. Thermal Spray Techn.* **6**, 35 (1997).
- [Nic03] J.R.R. Nicholls: Advances in coating design for high performance gas turbines. *MRS bull.* **28**, 659 (2003).
- [Pin95] B.A. Pint, J.R. Martin, L.W. Hobbs: The oxidation mechanism of theta- $\text{Al}_2\text{O}_3$  scales. *Solid St. Ion.* **78**, 99 (1995).



- [Pin96] B.A. Pint: Experimental observations in support of the dynamic-segregation theory to explain the reactive-element effect. *Oxid. Met.* **45**, 1 (1996).
- [Reb03] N.R. Rebollo, M.Y. He, C.G. Levi, A.G. Evans: Mechanism governing the distortion of alumina-forming alloys upon cyclic oxidation. *Zeit für Metall.* **3**, 171 (2003).
- [Rei83] L. Reimer, U. Zepke, J. Mösch, M. Ross-Messemer, W. Probst, E. Weimer: EELSpectroscopy. (Carl Zeiss, Electron Optics Division, ord. num: G34-640, Oberkochen, Germany, 1983).
- [Ryb89] G.C. Rybicki, J.L. Smialek: Effect of the  $\theta$ - $\alpha$ -Al<sub>2</sub>O<sub>3</sub> transformation on the oxidation behaviour of  $\beta$ -NiAl+Zr. *Oxid. Met.* **31**, 275 (1989).
- [San00] P.S. Santos, H.S. Santos, S.P. Toledo: Standard transition aluminas. Electron microscopy studies. *Mat. Res.* **3**, 104 (2000).
- [Sch94] P.F. Schmidt et al.: Praxis der Rasterelektronenmikroskopie und Mikrobereichsanalyse, Expert Verlag (1994).
- [Sch96] E. Schumann, J.C. Yang, M. Rühle, M.J. Graham: High resolution SIMS and analytical TEM evaluation of alumina scales on beta-NiAl containing Zr or Y. *Oxid. Met.* **46**, 37 (1996).
- [Sch00] J.C. Schaeffer, W.B. Connor, R.D. Field: Method for forming a thermal barrier coating. US Patent, 6,123,997; 2000.
- [Sea88] M.P. Seah, D. Briggs: Practical surface analysis, John Wiley & Sons Ltd., Chichester (1998).
- [Smi91] J.L. Smialek: Effect of sulfur removal on Al<sub>2</sub>O<sub>3</sub> scale adhesion. *Met. Trans. A*, **22 (3)**, 739 (1991).

- [Sol03] F. Soldera, N. Ilić, S. Brännström, I. Barrientos, H. Gobram, F. Mücklich: Formation of Al<sub>2</sub>O<sub>3</sub> scales on single-phase RuAl produced by reactive sintering. *Oxid. Met.* 59, 529 (2003).
- [Spi03] I.T. Spitsberg: Method for improving the TBC life of a single phase platinum aluminide bond coat by preoxidation heat treatment. US Patent Application, US 2003/0203221 A1 (2003).
- [Str03] A. Strecker, U. Salzberger: Specimen preparation for transmission electron microscopy: reliable method for cross-section and brittle materials. *Mayer J. Prakt Metallogr.* 30, 482 (1993).
- [Stu50] H.C. Stumpf, A.S. Russel, J.W. Newsome, C.M. Tucker: Thermal transformations of aluminas and alumina hydrates. *Ind. Eng. Chem.* 42, 1398 (1950).
- [Tal67] R.L. Tallman, E.A. Gulbransen: Crystal morphology and mechanisms of growth of  $\alpha$ -Fe<sub>2</sub>O<sub>3</sub> whiskers on iron. *J. Electrochem. Soc.* 114(12), 1227 (1967).
- [Tie72] J.K. Tien, F.S. Pettit: Mechanism of oxide adherence on Fe-25Cr-4Al(Y or Sc) alloys. *Metall. Trans.* 3, 1587 (1972).
- [Tol00] V.K. Tolpygo, D.R. Clarke: Microstructural study of the theta-alpha transformation in alumina scales formed on nickel-aluminides. *Mat. High Temp.* 17, 59 (2000).
- [Tol01] V.K. Tolpygo, D.R. Clarke, K.S. Murphy: Oxidation-induced failure of EB-PVD thermal barrier coatings. *Surface and Coatings Tech.* 146, 124 (2001).
- [Try04] B. Tryon, T.M. Pollock, M.F.X. Gigliotti, K. Hemker: Thermal expansion behavior of ruthenium aluminides. *Scripta Mat.* 50, 845 (2004).

- [Van88] G. Van Tendeloo, H.W. Zandbergen, S. Amelinckx: Electron diffraction and high resolution electron microscopic study of the 20K superconducting phase in the Bi-Sr-Cu-O system. *Solid St. Comm.* **66**, 927 (1988).
- [Wag33] C. Wagner. *Z. Phys. Chem.* **21**, 25 (1933)
- [Wil79] J. Wilson: Phase transformations and developments of microstructures in boehmite-derived transition aluminas. *Proc. Br. Ceram. Soc.* **28**, 281 (1979).
- [Wil96] D.B. Williams, C.B. Carter: *Transmission Electron Microscopy*. Plenum Press, New York, USA (1996).
- [Wol96] I.M. Wolff: Synthesis of RuAl by reactive powder processing. *Met. Mat. Trans. A.* **27**, 3688 (1996).
- [Wol97] I.M. Wolff, G. Sauthoff: Role of an intergranular phase in RuAl with substitutional additions. *Acta Mat.* **45**, 2949 (1997).
- [Yan98] J.C. Yang, E. Schumann, I. Levin, M Rühle: Transient oxidation of NiAl. *Acta Mater.* **46**, 2195 (1998).
- [Zho04] C. Zhou, J. Yu, S. Gong, H. Xu: Influence of water vapor on the high temperature oxidation behavior of thermal barrier coatings. *Mat. Sci. Eng. A* **348**, 327 (2003).

## ACKNOWLEDGEMENTS

I would like to thank:

Prof. Manfred Rühle for giving me the opportunity to work in his department and his confidence in the forthcoming of this thesis.

Prof. Fritz Aldinger for taking over the *Mitbericht*.

Dr. Amalia Catanoiu for her support throughout the project and proofreading of the thesis.

Dr. Francisco M. Morales Sánchez and Dr. Julie Carney, for the fruitful discussions and support in the field of Transmission Electron Microscopy.

Dr. Wilfried Sigle, Dr. Fritz Phillipp and Dr. Christoph Koch for the support in the use and in the interpretation of the TEM.

Dr. Sašo Šturm and Dr. Vesna Srot for nice discussions and the help with the HAADF experiments.

Dr. Stephan Kraemer for his help in getting started and explaining the use of the TGA.

Herr Meisner and Herr Preininger respectively for the sample preparation and the quartz manufacturing necessary for the TGA.

Dr. Nicole Rauch, Dr. Elena Tchernychova and Dr. Boriana Raschkova for their nice company and the help they offered me during the last years.

Prof. C. Levi, Prof. G.H. Meier, Prof. T.M. Pollock, Prof. R. Cannon and Herr Lamparter for fruitful discussions.

Dr. B. Veal and Arun Reddy for the excellent work done at the synchrotron at the Argonne National Laboratory.

Dr. B. Tryon and F. Cao from Univ. of Michigan for the preparation of the bulk material and for making my staying in Ann Arbor so nice.

Herr Opielka, Horst, and Dr. Fabio Lupo for their everyday help concerning whatever problem, thank you.

All the TEM group and especially Ute Salzberger, Ute Bäder and Adolf Strecker for their help and preparation of excellent TEM specimens; and Kersten Hahn and Marion Kelsch for introducing me to the microscopes.

Birgit Heiland for her positive character and behaviour and the preparation of very nice FIB specimens for TEM.

Frau Kuehnemann for the excellent SEM work and Frau Haug for the EPMA.

Ira Swoboda and Elisabeth Pfeilmeier for their patient help in solving all the annoying problems caused by the excellent German bureaucracy.

I would like also to thank my family and all my friends for their constant support.

This research was supported by a program of international collaboration between the European Commission (GRD-200-30211) and National Science Foundation (DMRR-0099695).

# Lebenslauf

## Persönliche Daten

Name: Bellina Paul  
Geburtsdatum: 16.05.1975  
Familienstand: ledig  
Staatsangehörigkeit: Italienisch

## Schulbildung

1981-1986 Scuola elementare “Italienische Grundschule”, Udine, Italien  
1986-1989 Scuola media-inferiore, “Italienische Mittelschule”, Udine, Italien  
1989-1994 Scuola media-superiore, “Italienische Mittel-Hochschule” (Note 56/60), Udine, Italien

## Hochschulstudium

1994-2002 Università degli Studi di Trieste, Corso in Ingegneria dei Materiali  
“Materialwissenschaftliche Technische Hochschule” (Note 108/110), Trieste, Italien

## Berufliche Erfahrungen/Praktika

- Oktober 2001-Februar 2002 Labortätigkeit als wissenschaftliche Hilfskraft (Raman Technik auf SiC) am *Kyoto Institute of Technology* unter Betreuung durch Prof. G. Pezzotti.
- 02.11.2002-13.02.2006 Promotion am *Max-Planck-Institut (MPI) für Metallforschung* in Stuttgart, Abteilung Prof. Rühle, Thema: “High Temperature Oxidation of Bulk RuAl Alloy”.

## Publikation

P.J. Bellina, A. Catanoiu, F.M. Morales, and M. Rühle: Formation of discontinuous Al<sub>2</sub>O<sub>3</sub> layers during high-temperature oxidation of RuAl alloys. *Journal of Materials Research* **21**, 276 (2006).